The Effects of Gap Ratio and Upstream Wall-Roughness on the Spatio-Temporal Turbulent Flow Dynamics Surrounding a Square Cylinder

By

Heath Alexander Chalmers

A Thesis Submitted to the Faculty of Graduate Studies of The University of Manitoba in Partial Fulfilment of the Requirements of the Degree of

MASTER OF SCIENCE

Department of Mechanical Engineering

University of Manitoba

Winnipeg

Abstract

Turbulent flow around a square cylinder offset at different heights from upstream smooth and rough walls are investigated using time-resolved particle image velocimetry. The Reynolds number based on the freestream velocity and cylinder height was 12 750 and the turbulent boundary layer thickness was 3.6 and 7.2 times the cylinder height for the upstream smooth and rough wall respectively. The first portion of this thesis discusses the effects of wall roughness for cylinders with a gap underneath the cylinder of 0.0, 0.3, 0.5, and 2.0 times the cylinder height. The results show that wall roughness reduces the mean reattachment length behind the wall-mounted cylinders by 29%, but does not significantly influence the mean recirculation length behind the offset cylinders. Wall roughness also suppresses the Reynolds stresses in the lower shear layer emanating from the undersurface of the offset cylinders. The dominant frequencies behind the wall-mounted cylinder are similar to the dominant frequencies of the incoming turbulent boundary layer regardless of the wall roughness conditions, but the fundamental frequencies in the wake behind the offset cylinders are dictated by the vortex shedding motions. The dominant shedding frequencies behind the offset cylinders are nearly independent of gap ratio when scaled by the freestream velocity, even though the cylinder is deeply submerged in a thick incoming turbulent boundary layer. Reconstruction of the vorticity field based on proper orthogonal decomposition shows that with a gap of 0.3 times the cylinder height, wall roughness reduces the size of vortical structures downstream the gap exit, and suppresses regular vortex shedding motion behind the cylinder.

The second portion of this two-manuscript based thesis presents a discussion on gap ratio effects on flow around a square cylinder with an upstream rough wall for additional cases with a gap size of 1.0, 4.0 and 8.0 times the cylinder height. The results show that the mean recirculation length

remains relatively constant for cases with a gap size greater than or equal to 1.0 times the cylinder height. Flow acceleration through the gap under the cylinder is strongest with a gap size of 2.0 times cylinder height. Downstream of the cylinder, the vertical velocity fluctuations contribute strongly to the production of turbulent kinetic energy by interacting with mean wall-normal velocity gradient in the vertical direction. The dominant frequency embedded in the incoming turbulent boundary layer persists in the wake of the cylinder when the gap size is less than 1.0 cylinder height. Kelvin-Helmholtz vortices originating from the top leading edge of cylinder occur at Strouhal numbers of $2.77-3.11$ for the cases with gap ratio ranging from $0.3-8.0$ cylinder heights, while spectral migration towards lower frequencies is observed for cases with gap sizes equal to 0.3 and 0.5 cylinder heights. The spatial trajectory of Kelvin-Helmholtz vortices extends further away from the cylinder as the gap size increases. Spectral proper orthogonal decomposition analysis shows that the von Kármán vortex shedding structures possess the highest spectral energy for all offset cases despite regular vortex shedding being disrupted when the gap size is 0.3 times the cylinder height.

Table of Contents

Contribution of Authors

In this two-manuscript based thesis the set of experiments collecting the smooth-wall data were performed by Samuel Addai, while I collected the data for the upstream rough wall cases. For the first manuscript, I analyzed the data and wrote the discussion and analysis portion of the manuscript. For the second manuscript, I analyzed and interpreted the data and wrote the manuscript in full. For both manuscripts, Dr. Xingjun Fang provided valuable assistance in data interpretation and preparation of the manuscript. My advisor, Dr. Mark Tachie, provided guidance in the design of experiments, data analysis and evaluation of the manuscripts.

Heath Chalmers	Dr. Mark F. Tachie
MSc. Student and First Author	Academic Advisor and Last Author

Acknowledgments

Thank you to my parents Alex Chalmers and Sherri Gowan for their love and support in the development of this thesis and throughout my Masters degree at the Price Faculty of Engineering. Your support and encouragement have been crucial to achieving this milestone.

I would also like to thank my advisor Dr. Mark Tachie for his guidance and support throughout both my undergraduate and graduate research programs. Thank you to Dr. Xingjun Fang for your support and advice throughout my time in the Turbulence and Hydraulics Engineering Laboratory. I would also like to thank Sedem Kumahor, Samuel Addai, and all my colleagues in the lab for their friendship and motivation these past few years. I would also like to acknowledge Brendan Pachal for his technical support and ensuring my experiments ran smoothly and according to schedule. Finally, thank you to Dr. Wang and Dr. Essel for agreeing to be a part of my examining committee.

Nomenclature

English

$a_j^{(k)}$	coefficient of SPOD k-th mode at j-th frequency
$a^{(k)}$	coefficient of POD k-th mode
C_f	skin friction coefficient
D	water depth
d_p	seeding particle diameter
f	frequency
G	gap height
g	gravitational acceleration
h	cylinder height
H	shape factor
k	instantaneous in plane kinetic energy: $½(u'u' + v'v')$
K	in-plane turbulent kinetic energy: $½(\overline{u'u'} + \overline{v'v'})$
L	cylinder length
L_R	permanent recirculation length
L_r	mean recirculation length
P_{tke}	turbulent kinetic energy production
P_{uu}, P_{vv}	Reynolds stress production terms for $\overline{u'u'}$ and $\overline{v'v'}$, respectively
R^2	coefficient of determination
Re	Reynolds number
S	spanwise length of cylinder
St	Strouhal number
St_k	Stokes number
t	measurement time

T_{int}	integral time scale
Tu	turbulence intensity
u'	streamwise instantaneous velocity
U	streamwise mean velocity
U_∞	freestream velocity
U_s	slip velocity
U_τ	friction velocity
v'	vertical instantaneous velocity
V	vertical mean velocity
x	streamwise coordinate
y	wall-normal coordinate

Greek

δ	boundary layer thickness
θ	momentum boundary layer thickness
ρ	density
τ_f	smallest timescale of the flow
τ_p	seeding particle relaxation time
ν	kinematic viscosity of water
Φ	SPOD mode
ϕ	spectral energy

Subscripts and Superscripts

$(\cdot)'$	fluctuating component
$(\cdot)_k$	variable for the k-th SPOD mode
$(\cdot)_j$	variable for the j-th frequency
$(\cdot)_{rms}$	root mean square value
$\overline{(\cdot)}$	time-averaged value

Acronyms

c.c.	complex conjugate
CMOS	complementary metal-oxide-semiconductor
FOV	field of view
KH	Kelvin-Helmholtz
LDV	laser Doppler velocimetry
LES	large-eddy simulation
Nd:YLF	neodymium yttrium lithium fluoride
PDF	probability density function
PIV	particle image velocimetry
POD	proper orthogonal decomposition
SPOD	spectral proper orthogonal decomposition
TBL	turbulent boundary layer
THEL	Turbulence and Hydraulics Engineering Laboratory
TKE	turbulent kinetic energy

List of Tables

List of Figures

1 Introduction

This section introduces the background information that has led to the study of near-wall square cylinders and presents a literature review of pertinent studies to this topic.

1.1 Background and Motivation

Separated and reattached turbulent flow induced by sharp edged bluff bodies is a fundamental design challenge in fluids engineering. Investigation into bluff bodies placed within a uniform flow have been used as a canonical test case to develop aerodynamic lift and drag theories. Bluff bodies situated near a wall are also a common phenomenon in both industrial and environmental engineering applications. For example, the structural integrity of elevated tourist walkways can be subject to time-varying aerodynamic loads as a result of flow separation. The fuel efficiency of semi-trucks can be impacted by the crossflow separations around the trailer, and the effectiveness of fluid thermal devices such as heat exchangers is often improved by using turbulators in the form of square ribs to promote turbulent mixing. Similarly, flow past pipelines on the sea floor and atmospheric boundary layer flows involve turbulent flow past a wall-mounted bluff body.

Flow past a square cylinder, with height h, in a flow with a uniform approach velocity, U_∞, results in flow separation at the leading edge of the cylinder with symmetric flow on the upper and lower surfaces of the cylinder as portrayed in Figure 1.1.1a. Unlike the uniform case, flow past a square cylinder in the vicinity of a solid wall is subjected to an approaching boundary layer, as depicted in Figure 1.1.1b. which shows a square cylinder of height, h, placed at a distance, G, away from a solid boundary. The boundary layer is characterized by freestream velocity, U_∞, and boundary layer thickness parameter δ, while the velocity at the cylinder centerline is denoted by U_c. The flow separates at the leading edge of the cylinder, and asymmetric recirculation flow forms on

either side of the cylinder and in the cylinder wake. The flow dynamics becomes comparatively more complex when the bluff body is placed near the wall due to the presence of different turbulent scales and complex interaction of the cylinder wake and the turbulent boundary layer.

There have been considerable studies on the drag and lift around cylinders placed in uniform flow as well as the von Kármán vortex street in the cylinder wake (Roshko, 1954; Okajima, 1982; Bai & Alam, 2018). However, only a handful of studies have focused on a square cylinder placed near a wall (Durão et al., 1991; Martinuzzi et al., 2003; Panigrahi, 2009). Further, these studies employed an upstream smooth wall even though most applications occurring near a hydraulically rough surface such as oil pipelines near an uneven seabed or elevated walkways near mountainous terrain. There is, therefore, a need to investigate the dynamics of near-wall cylinder flow with the added complexity of upstream wall roughness.

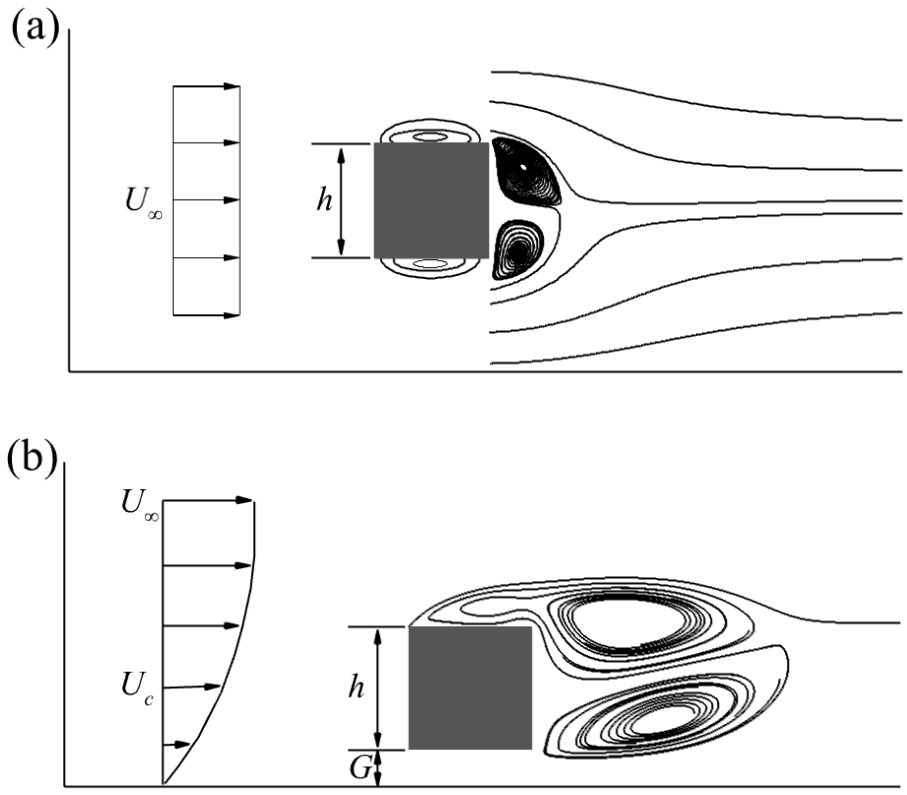

Figure 1.1.1: Schematic of flow features past (a) a square cylinder placed in uniform flow, and (b) a square cylinder placed near a wall.

1.2 Literature Review

1.2.1 Square Cylinders in a Uniform Flow

Early work by Roshko (1954) describes the separated shear layer past bluff bodies in a uniform flow. In general, the flow separates upstream of a sharp-edged bluff body and rolls up into a train of vortices on the upper and lower surfaces of the bluff body, which are commonly termed Kelvin-Helmholtz (KH) vortices. These KH vortices have been reported for various shear flows including an adverse pressure gradient turbulent boundary layer (TBL) and separated shear flows induced by sharp-edged rectangular cylinders (McAuliffe & Yaras, 2010; Brun et al., 2008; Moore et al., 2019) and circular cylinders (Roshko, 1954; Riches et al., 2018). Brun et al. (2008) used large eddy simulation (LES) and laser Doppler velocimetry (LDV) to show that, for flow around a square

cylinder, the KH vortices appears at $Re > 1\,000$ (where $Re = U_\infty h/\nu$, and U_∞ is the freestream velocity, h is the cylinder height, and ν is the kinematic viscosity of water) and possesses a frequency of approximately $St_{KH} = 2.2\text{–}3.5$, (where $St_{KH} = f_{KH} h/U_\infty$, and f_{KH} is frequency). Lander et al. (2016) performed a particle image velocimetry (PIV) study into the formation of KH vortices over a square cylinder in uniform flow with varying turbulence intensity, $Tu = \sqrt{\overline{u'u'}}/U_\infty$. They determined that when the freestream turbulence increases from 1.0% to 6.5%, the initial formation of KH vortices, identified using concentration of vorticity, approaches the leading edge, although the concentration of vorticity dissipates by $x/h = 0.5$, where x is measured from the cylinder's leading edge, regardless of the freestream turbulence. Moore et al. (2019) defined the transition point as the location at which the growth rate of turbulent kinetic energy along the separated shear layer diminishes downstream of the square cylinder's leading edge. This transition location is shown to meander towards the cylinder's leading edge as the Reynolds number increases. They noted that migration of energy towards the larger scales decreases significantly downstream of the transition location. Okajima (1982) investigated the effects of Reynolds number on the shedding frequency behind a square cylinder and determined that between $Re = 1\,000\text{–}20\,000$, the Strouhal number remains nearly constant between $St_{VK} = 0.125\text{–}0.135$. This range agrees well with the more recent findings of Kim et al. (2002) and Bai & Alam (2018) who both reported $St_{VK} = 0.136$ at similar Reynolds numbers, as well as $St_{VK} = 0.138$ reported by Kumahor & Tachie (2021).

1.2.2 Wall-Mounted Bluff Bodies

The dynamics of the flow past wall-mounted bluff bodies present significant complications due to the confinement of the solid boundary. Studies by Sherry et al. (2010) and Essel et al. (2015) investigated Reynolds number effects on flow past forward-facing steps. They concluded that the

mean reattachment length over the step increases monotonically with Reynolds number until a threshold value of $Re = 6\,380$ (Essel et al., 2015) or $8\,500$ (Sherry et al., 2010), depending on factors such as the upstream turbulence intensity, and mean shear in the incoming TBL. Sherry et al. (2010) also observed that above a Reynolds number of 800, the separated shear layer becomes susceptible to KH instabilities. This behaviour was also observed by Ikhennicheu et al. (2019) for wall-mounted square cylinder at $Re = 250\,000\,000$, who further demonstrated that the KH vortices are inclined towards the surface at an angle of 9 degrees. Recent investigations on wall-mounted bluff bodies have shown that large scale motions in the upstream boundary layer significantly interact with the bluff body. For example, Fang & Tachie. (2019a) used time-resolved PIV to show that, with a boundary layer thickness to step height ratio, $\delta/h = 4.8$ shear layers emanating from the leading and trailing edges of a rectangular bluff body interact and merge in the wake region. They further demonstrated that this interaction manifests in the flapping motion of separation bubbles above and behind the cylinder at a frequency of $St = 0.075$ based on the freestream velocity. Chalmers et al. (2021) also showed that, for bluff bodies with $L/h > 2$ immersed in an upstream rough wall boundary layer, the frequency of the large-scale motions in the TBL manifests in the recirculation region above the cylinder. When $L/h \leq 2$, the interaction is also influenced by the flapping motion of the recirculation region in the wake.

1.2.3 Square Cylinders Near a Wall

Bluff bodies in the vicinity of a wall are further complicated by the interaction of the different turbulent scales arising from the TBL, the KH vortices, the flapping motion of separation bubbles, and the von Kármán vortices. Many studies have documented the behaviour of the vortex shedding pattern in the wake of a near-wall square cylinder (Durão et al., 1991; Martinuzzi et al., 2003; Wang & Tan, 2008; Shi et al., 2010). Durão et al. (1991) used LDV to study square cylinder gap

flow at a Reynolds number of 13 600. They reported that vortex shedding in the wake is suppressed when the gap ratio, G/h where G is the size of the gap underneath the cylinder, becomes less than 0.35. The critical gap ratio at which vortex shedding becomes suppressed is dependent on the incoming flow parameters and could be as low as 0.2 (Kumeran & Vengadesan, 2007), and as high as 0.5 (Samani & Bergstrom, 2015). The shedding frequency of vortices in the wake region is generally between 0.12 and 0.14, although there is disagreement in the literature as to whether the shedding frequency is independent of the cylinder's proximity to the wall (Martinuzzi et al., 2003; Shi et al., 2010) or if the frequency decreases as the cylinder approaches the wall (Kumeran & Vengadesan, 2007; Samani & Bergstrom, 2015). A recent study by Addai (2022) showed that, with an upstream smooth wall, KH vortices are present in the shear layer and are shed at a frequency of approximately 20 times higher than the von Kármán vortex shedding frequency.

1.2.4 Roughness Effects

The mean flow and turbulent characteristics in canonical rough wall TBL have also been studied extensively since the pioneering work of Nikuradse (1933). These studies clearly demonstrated that wall roughness increases the boundary layer thickness, mean shear, turbulence level and drag compared to a smooth wall (Tachie et al. 2000; Akinlade et al. 2004; Flack & Schultz 2014; Baars et al. 2016; Hearst et al. 2016). The effects of wall roughness on the dynamics of separated shear flows induced by wall-mounted bluff bodies such as forward-facing step (FFS) are also well documented. Studies by Rifat et al. (2016), Essel & Tachie (2017) and Kumahor et al. (2021) on FFS reported a reduction of the mean reattachment length over the step by 30-48% compared to a case with an upstream smooth wall. The reduction of the mean reattachment length is attributed to strong mean shear and enhanced turbulence level which promote earlier mean flow reattachment. Fang & Tachie (2019a) performed experiments with an upstream boundary layer thickness, $\delta/h =$

4.8, over a bluff body with streamwise aspect ratio of $l/h = 2.36$ subjected to an upstream rough wall and observed mean flow reattachment on top of the body. A study by Chalmers et al. (2021) with a similar $\delta/h = 6.5$, demonstrated mean flow reattachment on top of bluff bodies subjected to upstream roughness, with $l/h > 1.0$. In contrast, the experimental investigations by Bergeles & Athanassiadis (1983) and van der Kindere & Ganapathisubramani (2018) with an upstream smooth wall showed that mean flow reattachment only occurred on top of the bluff body for $l/h > 5$ and 4, respectively. Chalmers et al. (2021) further reported the mean recirculation length in the wake of a wall-mounted square cylinder (L_r/h), defined as the streamwise distance from the trailing edge to the mean flow reattachment point on the wall, to be 6.3, which is 16-45% shorter than those reported in previous studies on square cylinders subjected to turbulent boundary layers developed over smooth walls (Bergeles & Athanassiadis 1983; Agelinchaab & Tachie 2008; Nematollahi et al. 2017; van der Kindere & Ganapathisubramani 2018). These findings suggest remarkable wall-roughness effects on the flow characteristics over wall-mounted bluff bodies. Since many past studies employed point-wise measurement techniques (Bergeles & Athanassiadis 1983) or low-repetition rate PIV systems (Agelinchaab & Tachie 2008; van der Kindere & Ganapathisubramani 2018), the time-varying flow dynamics remain largely unknown. Thus, in spite of the extensive investigations of the effects of wall roughness on flows around wall-mounted bluff bodies, the spatio-temporal interaction between a rough wall TBL and near-wall bluff bodies is still not well understood. Therefore, the focus of the present investigation is to elucidate the effects of wall roughness on the spatio-temporal flow dynamics induced by cylinders at different wall proximities using a time resolved PIV.

1.3 Objectives and Outline

Given the above discussion concerning the limited understanding of gap size on square-cylinder flow, and the profound effects that wall-roughness imposes on turbulent shear flows, the objectives of this thesis are to study effects of both gap ratio and upstream wall roughness on the spatio-temporal flow field surrounding a square cylinder in the vicinity of a rough wall using time-resolved PIV. The remainder of the thesis is organized as follows: the experimental setup and measurement procedure are described in Chapter 2, while the results on comparison between the flow dynamics in the wake of a square cylinder with upstream smooth and rough wall, which is published as the first manuscript, are presented in Chapter 3, and the discussion from the second manuscript concerning further gap ratio effects of flow around a square cylinder with an upstream rough wall is presented in Chapter 4. A summary of the major conclusions from this thesis and future work are presented in Chapter 5.

2 Experimental Setup and Measurement Procedure

This section provides details concerning the experimental facility, test setup, measurement procedure, and vector calculation of the data presented in this thesis.

2.1 Experimental Setup

The experiments were performed in an open recirculating water channel installed in the Turbulence and Hydraulic Engineering Laboratory (THEL) at the University of Manitoba. The water channel contains a flow conditioning unit upstream of the test section consisting of a perforated plate, hexagonal honeycomb mesh and a 4.88:1 flow contraction section. Downstream of the test section the flow is returned to the conditioning unit via a return plenum. The test section of the water channel, pictured in Figure 2.1.1, has a streamwise length, a vertical height and a spanwise width of 6000 mm, 450 mm and 600 mm, respectively. The two sidewalls and bottom wall of the test section were fabricated from 31.8-mm thick Super Abrasion Resistant® transparent acrylic plates to allow optical access to the flow from all directions. A 30 kW variable-speed drive motor was used to control the speed of the pump driving the recirculating water.

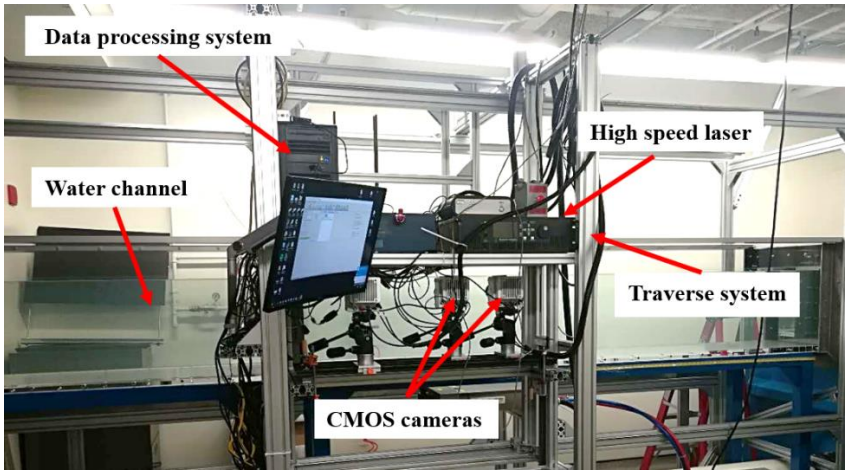

Figure 2.1.1: Photograph of the test facility.

A schematic of the test section, the square cylinder and the coordinate system adopted in this study are shown in Figure 2.1.2. The origins of the streamwise (x) and vertical (y) coordinates are set, respectively, at the leading edge and the vertical mid-point of the cylinder. The bottom wall consists of two replaceable sections: a 100-mm long entrance insert which promotes early transition to TBL, and a 5900-mm long wall insert. Two different bottom wall conditions were examined: for the first bottom wall condition, the entrance insert was a 6-mm thick acrylic plate attached with 16-grit sandpaper, and the subsequent wall insert was made of a 6-mm thick smooth acrylic plate. This test condition is hereinafter referred to as the smooth case. For the second bottom wall condition, the entrance insert was a toothed barrier consisting of 15-mm high triangular ribs (which was identical to that used in Fang & Tachie 2019a), while the wall insert was made of a 6-mm thick acrylic plate with 16-grit sandpaper glued on the top surface. The sandpaper, with an average roughness height of 1.54 mm, extended over 4400 mm downstream the leading edge of the acrylic plate. This test condition is hereinafter referred to as the rough case.

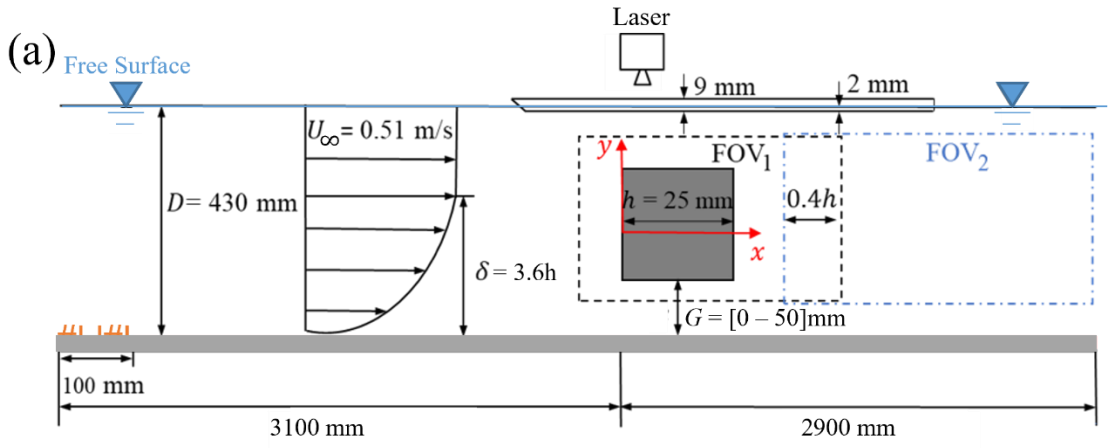

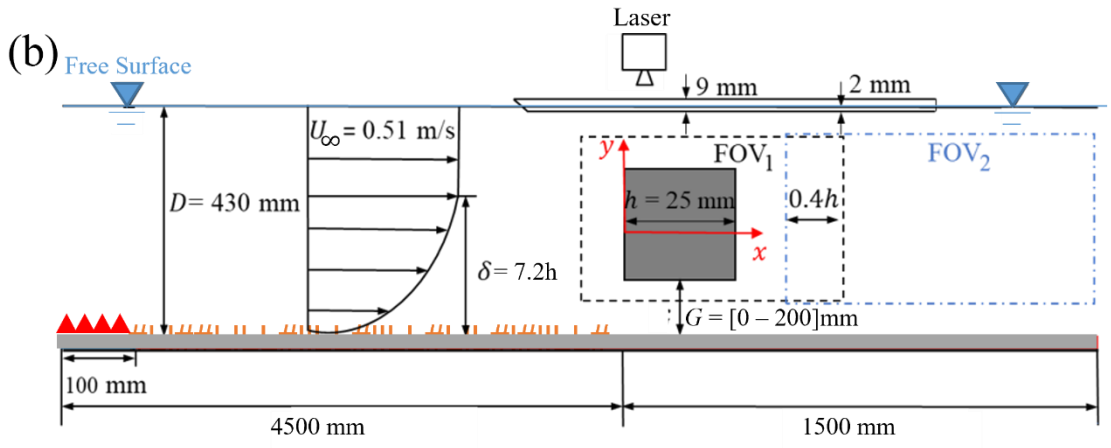

Figure 2.1.2: Schematic of the test channel setup and camera placement with (a) an upstream smooth wall and (b) an upstream rough wall.

A schematic of the test section, the square cylinder and the coordinate system adopted in this study are shown in Figure 2.1.2. The origins of the streamwise (x) and vertical (y) coordinates are set, respectively, at the leading edge and the vertical mid-point of the cylinder. The bottom wall consists of two replaceable sections: a 100-mm long entrance insert which promotes early transition to TBL, and a 5900-mm long wall insert. Two different bottom wall conditions were examined: for the first bottom wall condition, the entrance insert was a 6-mm thick acrylic plate attached with 16-grit sandpaper, and the subsequent wall insert was made of a 6-mm thick smooth acrylic plate. This test condition is hereinafter referred to as the smooth case. For the second bottom wall condition, the entrance insert was a toothed barrier consisting of 15-mm high triangular ribs (which was identical to that used in Fang & Tachie 2019a), while the wall insert was made of a 6-mm thick acrylic plate with 16-grit sandpaper glued on the top surface. The sandpaper, with an average roughness height of 1.54 mm, extended over 4400 mm downstream the leading edge of the acrylic plate. This test condition is hereinafter referred to as the rough case.

The square cylinder of height, $h = 25$ mm, was positioned over the bottom wall inserts at streamwise distances 3100 mm and 4500 mm downstream of the test section entrance, respectively, for the smooth and rough wall conditions. The cylinder was firmly held between two 6-mm thick acrylic plates, one attached to each of the sidewalls of the test section. Each acrylic plate had a streamwise length of 1170 mm, with its leading edge at 573 mm upstream of the cylinder leading edge. The leading edges of the acrylic plates had a chamfer of 45° to minimize distortion to the flow at the channel mid-span where the velocity measurements were conducted. The cylinder had a spanwise width (S) of 588 mm and the resultant aspect ratio, S/h = 23.5, was sufficient to ensure two-dimensionality of the time-averaged flow at the channel mid-span (Panigrahi & Acharya 1996; Fang & Tachie 2019a). The mid-section of the cylinder and the bottom wall were painted with non-reflective black paint to minimize surface glare from laser illumination.

Table 2.1.1. Summary of test cases, pertinent notations and values of U_c.

Upstream wall condition	G/h	Notation	U_c (m/s)
Smooth	0.0	S0	0.358
	0.3	S0.3	0.385
	0.5	S0.5	0.401
	2.0	S2	0.471
Rough	0.0	R0	0.255
	0.3	R0.3	0.285
	0.5	R0.5	0.299
	2.0	R2	0.374
	4.0	R4	0.442
	8.0	R8	0.510

Table 2.1.1 summarizes all test cases for the present research, and the notation of each case adopted hereinafter. The gap distance (G) from the top surface of the bottom wall inserts to the bottom surface of the square cylinder was varied to obtain 4 gap ratios, G/h = 0.0, 0.3, 0.5 and 2.0 for the smooth case and an additional 3 gap ratios, G/h = 1.0, 4.0, and 8.0 for the rough case. As seen in Table 2.1, the cases of $G/h = 0.3$ for the smooth and rough cases are denoted by S0.3 and R0.3, respectively, while similar notations are used to denote other test cases as well. During all experiments, the water depth (D) and the freestream velocity (U_∞) were kept constant at 430 mm and 0.51 m/s, respectively. The resultant blockage ratio (h/D) was 5.8%. For an open water channel, the free surface is equivalent to a symmetry plane (Fang & Tachie 2019a). As such, the effective blockage ratio was 2.9% which is less than the threshold value of 5% below which blockage effect on the flow is negligible (Farell et al. 1977). The Froude number ($Fr = U_\infty/\sqrt{gD}$, where $g = 9.81$ m/s^2 is the acceleration due to gravity) was 0.24, suggesting negligible surface wave effects on the flow dynamics (Fang & Tachie 2019a). Additionally, a 9 mm thick acrylic plate of an area of 585 mm × 585 mm and with a rounded leading edge was immersed into the water by about 2 mm, as shown in 2.0.2, to eliminate any distortion of the laser sheet by surface waves. The room temperature was maintained at 20℃ and thus the kinematic viscosity of water (ν) was 10^{-6} m^2/s. The Reynolds number based on the freestream velocity and cylinder height ($Re_h = U_\infty h/\nu$) was 12 750 which is comparable to those of previous studies on near-wall square cylinders (Durão et al. 1991; Wang & Tan 2008).

2.2 Measurement Procedure

The velocity measurements were performed in the streamwise-vertical (x-y) plane at the channel mid-span using a planar time-resolved particle image velocimetry (TR-PIV) system. Silver-coated hollow glass spheres with an average diameter of d_p = 10 μm and specific gravity of 1.4 were used

to seed the flow. Following Raffel et al. (2007), the slip velocity (u_s) was estimated using equation 2.1,

$$u_s = \frac{d_p^2(\rho_p - \rho_f)g}{18\rho_f \nu} \tag{2.1}$$

to be 2.18 × 10^{-5} m/s. Here, ρ_p and ρ_f denote the densities of the seeding particles and water, respectively. To characterize the response of the seeding particles to sudden changes in the flow motion, the relaxation time ($\tau_p = u_s/g$) was estimated to be 2.20 × 10^{-6} s, while the smallest temporal scales of the turbulent flows were estimated using the viscous time scale, $\tau_f = \nu/u_\tau^2$, where u_τ is the friction velocity determine using the Clauser plot technique, to be 2.77×10^{-3} s and 2.40 ×10^{-3} s for the smooth and rough wall cases, respectively. As such, the Stokes numbers ($S_k = \tau_p/\tau_f$) were, respectively, 0.0008 and 0.0009 for the smooth and rough walls. These values are well within the recommended range of $S_k \leq 0.05$ for the particles to faithfully follow the fluid flow (Samimy & Lele 1991).

A dual-cavity high-speed Neodymium-doped yttrium lithium fluoride (Nd: YLF) laser with a maximum pulse energy of 30 mJ/pulse for each emitted green light and a wavelength of 527 nm was used to illuminate the particles. The laser light sheet thickness was approximately 2 mm. The illuminated flow field was captured using two 12-bit complementary metal oxide semiconductor (CMOS) cameras positioned side-by-side with a full resolution of 2560 pixel × 1600 pixel. The cameras were positioned perpendicular to the sidewall of the water channel, and calibrated under the same optical condition as the actual measurements. As such, any aberration of particle images due to change of refractive index is minimized and does not reduce the measurement accuracy. For the smooth wall condition, the fields of view (FOVs) in the streamwise and vertical directions

were, respectively, $8.5h \times 5.3h$ ($2.36\delta \times 1.47\delta$) for the first camera and $10.7h \times 6.6h$ ($2.97\delta \times 1.83\delta$) for the second camera. The fields of view of both cameras for the rough wall condition were kept the same at $6.7h \times 4.3h$ ($0.93\delta \times 0.06\delta$) in the streamwise and vertical directions, respectively. In all measurements, an overlap of $0.4h$ in the streamwise direction was maintained between the FOVs of the two cameras. A total of 60 000 images were captured for each measurement at a frame rate of 806 Hz.

Data acquisition and velocity vector calculations were performed using a commercial software (DaVis version 10) supplied by LaVision Inc. (Ypsilanti, Michigan, United States of America). To minimize peak locking, the particle image diameter was kept within the range 2-4 pixels in all measurements, following the DaVis manual by LaVision Inc. The velocity vectors were calculated using a graphical-processing-unit-accelerated multi-pass cross-correlation algorithm. For both wall conditions, the interrogation area for the initial pass was 128 pixel × 128 pixel with 50% overlap and that for the fourth and final pass was 24 pixel × 24 pixel with 75% overlap. The resulting vector spacings were $0.0157h$ ($7.4\nu/U_\tau$, where U_τ is the friction velocity for the incoming turbulent boundary layer) and $0.0250h$ ($11.8\nu/U_\tau$) for FOV_1 and FOV_2, respectively, for the smooth wall condition and $0.0160h$ ($12.7\nu/U_\tau$) for both FOVs for the rough wall condition. All post-processing of calculated velocity fields was performed using in-house Matlab® scripts. For the ensuing discussion, u and v represent the streamwise and vertical instantaneous velocities, respectively. The fluctuating and time-averaged velocities are indicated using a superscript prime and an overbar, respectively, e.g., v' and $\bar{v}$. For convenience, an upper-case letter is also used to denote the time-averaged velocity, e.g., $V \equiv \bar{v}$.

2.3 Measurement Uncertainty

Following the approach presented in Fang et al. (2022), equations 2.2 and 2.3 were used to calculate the measurement uncertainty of the mean velocity and Reynolds normal stresses, respectively.

$$\xi_U = \frac{Z_c}{U}\sqrt{\frac{\overline{u'u'}}{N_{eff}}} \tag{2.2}$$

$$\xi_{uu,vv} = Z_c\sqrt{\frac{2}{N_{eff}}} \tag{2.3}$$

In the above equations, ξ is the measurement uncertainty of the mean velocity and Reynolds stresses, Z_c is the confidence coefficient and is taken as $Z_c = 1.96$ for 95% confidence, and $N_{eff} = \frac{t}{2T_{int}}$ where t is the total sampling time and T_{int} is the integral time scale, is the effective number of samples collected during the experiment. The results were calculated for each test case with an upstream rough wall along the shear layer emanating from the cylinder's leading edge. The measurement uncertainty for the streamwise velocity and Reynolds normal stresses are presented in Table 2.3.1 for the various test cases. Notably from Table 2.3.1 the measurement uncertainty is highest for lower gap ratio cases due to the high Reynolds stress present in the deeply thick turbulent boundary layer.

Table 2.3.1. Summary of measurement uncertainty.

Test Case	N_{eff}	ξ_U [%]	$\xi_{uu,vv}$ [%]
R0	422	4.2	13.5
R0.3	337	5.4	15.1
R0.5	368	4.3	14.4
R1	609	3.4	11.2
R2	512	3.8	12.2
R4	675	4.0	10.7
R8	682	4.5	10.6

3.0 The Effects of Wall Roughness on the Flow Dynamics Behind a Near-Wall Square Cylinder

In this chapter, the results and discussion published in the paper: Chalmers, H., Fang, X., Addai, S., and Tachie, M.F., 2022, "The effects of wall roughness on the flow dynamics behind a near-wall square cylinder," Experiments in Fluids, 63:123 are presented.

3.1 Incoming turbulent boundary layers

The TBLs over the smooth and rough walls are characterized in this section. Note that the measurements of the two incoming turbulent boundaries were performed at the same streamwise location where the cylinders would be installed but without the presence of cylinders.

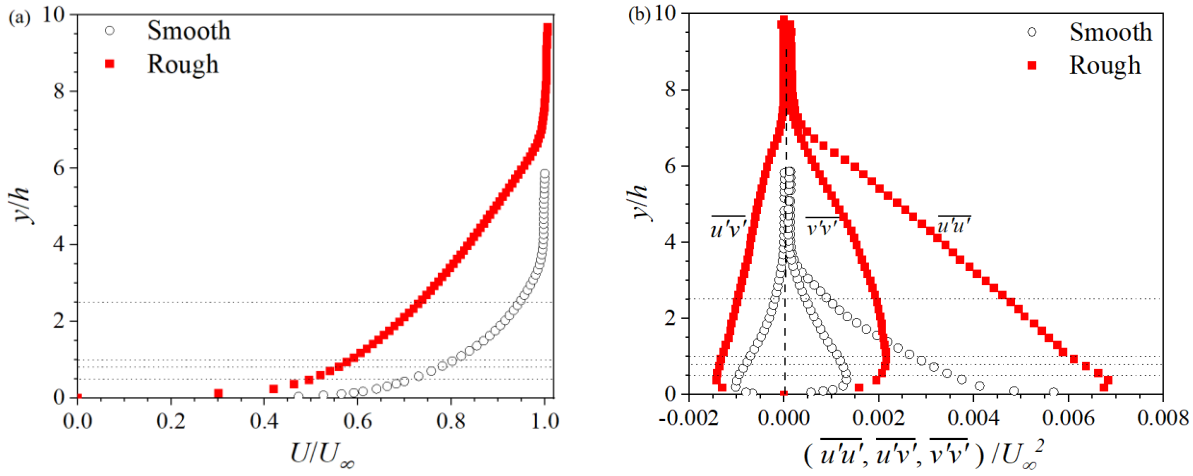

Figure 3.1.1: Vertical profiles of (a) streamwise mean velocity (U) and (b) Reynolds stresses ($\overline{u'u'}$, $\overline{u'v'}$ and $\overline{v'v'}$) for the incoming TBL over smooth and rough walls. Four horizontal dashed lines mark the centerlines of cylinders in the cases of $G/h = 0.0$, 0.3, 0.5 and 2.0 (from bottom to top).

Table 3.1.1. Parameters for incoming TBLs over different wall conditions.

Cases	δ/h	θ/h	H	$C_f \times 10^3$	Re_h	Re_τ	Re_θ
Smooth	3.6	0.46	1.34	2.8	12 750	1699	5814
Rough	7.2	1.05	1.56	4.1	12 750	5750	13 362

Figure 3.1.1 compares the vertical profiles of mean (time-averaged) velocity and Reynolds stresses, while Table 3.1.1 summarizes the pertinent parameters for the two TBLs. In the smooth case, the shape factor (1.34) is similar to the reported value by Chauhan et al. (2009) for turbulent boundary layers subjected to zero pressure gradient at the same Re_θ ($Re_\theta = U_\infty \theta/\nu$, where θ is the boundary layer momentum thickness). The skin friction coefficient for the smooth wall is within 1.8% of the value determined from the correlation, $C_f = 0.024 Re_\theta^{-0.25}$ proposed by Smits et al. (1983). In the rough wall case, the relative boundary layer thickness ($\delta/h = 7.2$) is twice that ($\delta/h = 3.6$) in the smooth case, and both the skin friction C_f and shape factor are also comparatively larger than the corresponding smooth-wall values. Additionally, the turbulence intensity that the cylinder is exposed to is significantly higher in the rough wall case. For instance, the value of $\overline{u'u'}$ at the centerline of the R2 case ($\overline{u'u'}/U_\infty^2 = 0.0046$, which is equivalent to a turbulence intensity of 7%) is five timesthe value ($\overline{u'u'}/U_\infty^2 = 0.0009$, which is equivalent to a turbulence intensity of 3%) in the S2 case. In Figure 3.1.1, the elevations of cylinder centerlines for different cases are marked using horizontal dashed lines, and were immersed in the incoming turbulent boundary layers. For instance, the centerlines of the cylinders in the case of G/h = 2.0 are at $y/\delta = 0.69$ and 0.35 for the smooth and rough cases, respectively. Thus, the incoming streamwise mean velocity at the centerline of cylinder, U_c, is used as the appropriate velocity scale

in the subsequent data presentation, since the freestream region is relatively far away from the cylinder (Lim et al. 2007; Fang & Tachie 2019a, 2019b, 2020).

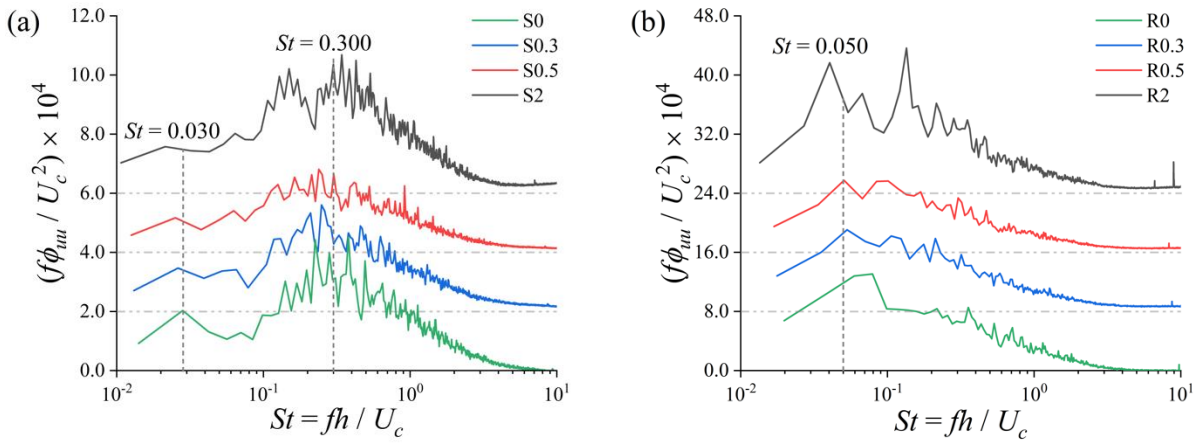

Figure 3.1.2: Premultiplied frequency spectra of streamwise fluctuating velocity at the centerlines of cylinders in different cases for the (a) smooth and (b) rough cases. The spectra are offset vertically to facilitate visualization.

Figure 3.1.2 examines the frequency spectra of the incoming streamwise fluctuating velocity at the centerlines in the different test cases. As seen in Figure 3.1.2a for the smooth case, the spectrum for the wall-mounted (S0) case possesses two distinct peak frequencies, one near $St = 0.030$, and the other centered around $St = 0.300$, where the Strouhal number *St* is defined as $St = fh / U_c$. The dominance of the former disappears as the centerline elevation increases for other test cases, whereas the latter persists. For Figure 3.1.2b, the spectra for all four test cases exhibit a peak frequency around $St = 0.05$. Assuming the mean velocity as the convective velocity in the context of Taylor's frozen hypothesis, the characteristic wavelength of coherent structure at $St = 0.05$ is 2.8δ. This wavelength is within the typical wavelength (2-3δ) for the large-scale motion in turbulent boundary layer (Adrian 2000). In our previous experimental studies of wall-mounted

bluff bodies (Chalmers et al. 2021; Fang & Tachie 2020) at a different Reynolds number (Re_h = 13 200) and with rough upstream walls, large-scale motion persists in the region of $y/\delta \in [0.1, 1.0]$.

3.2 Mean flow

Figure 3.2.1 shows the contours of streamwise mean velocity (U) superimposed with mean streamlines for all the test cases. As seen in Figures 3.2.1a and 3.2.1b, the mean flow in the wall-mounted cases (S0, R0) separates at the upper leading edge of the cylinder ((x/h, y/h) = (0.0, 0.5)) and reattaches onto the bottom wall forming a large mean separation bubble spanning the entire cylinder height. A separated shear layer emanating from the leading edge of the cylinder encompasses the large mean recirculation bubble. Meanwhile, a small mean recirculation bubble forms in the corner immediately behind the wall-mounted cylinder. On the other hand, the mean flows in the offset ($G/h > 0.0$) cases exhibit a pair of counter-rotating mean recirculation bubbles behind the cylinders. Two separated shear layers extending downstream of the upper and lower trailing edges of the cylinder ensue, and are hereinafter denoted by the upper and lower shear layers, respectively. Compared to the $G/h = 0.5$ and 2.0 cases, the mean recirculation in the lower region behind the cylinder for the $G/h = 0.3$ cases (Figure 3.2.1c and 3.2.1d) is skewed upwards. This reflects the significant influence of wall confinement on the mean flow for the smaller gap ratio. It is also interesting to notice in Figure 3.2.1 that there exists a region of elevated streamwise mean velocity downstream of the gap exit (i.e., $x/h > 1.0$ and $y/h < -0.5$). The maximum magnitude of streamwise mean velocity at the gap exit is approximately 15% smaller than the velocity in the upper shear layer for the S0.3 and R0.3 cases, but becomes approximately similar as the gap ratio increases to $G/h = 2.0$. The region of elevated velocity at the gap exit has also been reported by Durão et al. (1992), Panigrahi (2009) and Wang & Tan (2008), although the

difference between the maximum streamwise mean velocity in the upper and lower shear layers is smaller in the present study.

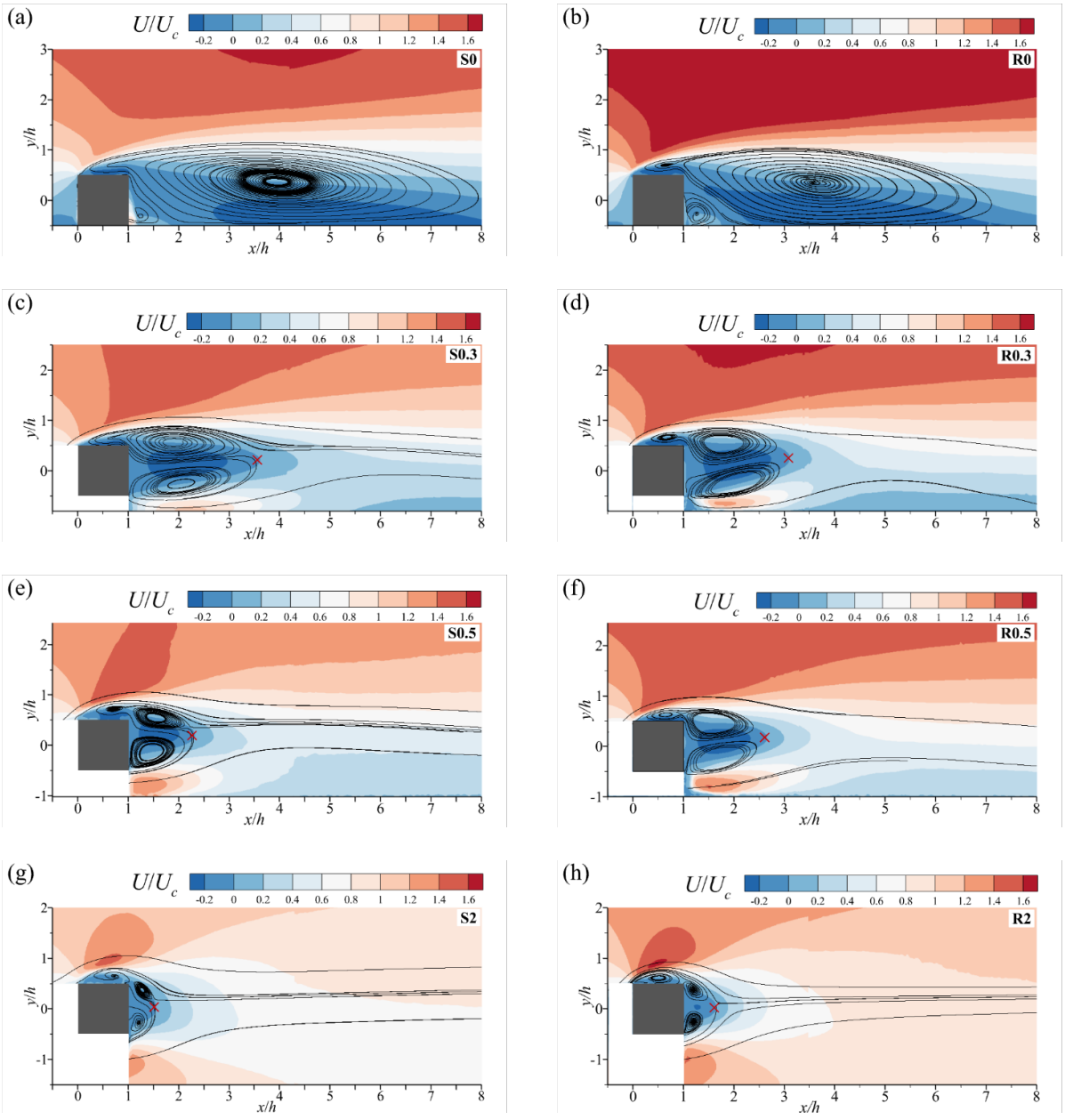

Figure 3.2.1: Contours of the streamwise mean velocity (U) for the cases of $G/h =$ (a, b) 0.0, (c, d) 0.3, (e, f) 0.5 and (g, h) 2.0 superimposed with representative mean streamlines for the

smooth (a, c, e, g) and rough (b, d, f, h) cases. The symbol × marks the furthest streamwise extent of the zero-velocity contour. Note that the measurement data right beneath the cylinders are unavailable due to the obstruction of laser sheet by the cylinder.

To better quantify the mean flow field, the mean recirculation length L_r, which is defined as the streamwise distance between the trailing edge of the cylinder and the most downstream point of the isopleth of $U = 0$, is calculated for each test case. Figure 3.2.2 compares the values of L_r for wall-mounted square cylinders from the present study and the existing literature with different Reynolds numbers and relative boundary layer thicknesses. From Figure 3.2.2a, the mean recirculation length for the smooth wall test cases monotonically increases with Reynolds number, and tends to an asymptotic value around $11.5h$ for Reynolds numbers beyond 20 000. This asymptotic behaviour of L_r with an upstream smooth wall is reminiscent of the observations by Sherry et al. (2010) and Essel et al. (2015) that the mean reattachment length over a forward-facing step (FFS) approaches an asymptotic value beyond Reynolds numbers (defined based on bluff body height and freestream velocity) 8500 and 6380, respectively. It is thus concluded that the mean recirculation length behind a wall-mounted square cylinder reaches Reynolds number independence at a higher Reynolds number than the FFS. Furthermore, the dependence of the recirculation length on Reynolds number follows the exponential function shown in Figure 3.2.2(a). As seen in Figure 3.2.2b, the values of L_r for the smooth wall decrease linearly with the relative boundary layer thickness, and the fitted linear function is presented in the figure. As seen in Figures 3.2.2a and 3.2.2b, the mean recirculation lengths for the rough wall cases are consistently smaller than the variation trend established for those over smooth walls. The reduced mean recirculation length for the rough wall cases is due to the enhanced flow

entrainment into the separation bubble by the elevated turbulence intensity and mean shear in the incoming TBL over roughness walls that the bluff body is exposed to. A similar conclusion was made by Nematollahi & Tachie (2018) for FFS with upstream smooth and rough walls.

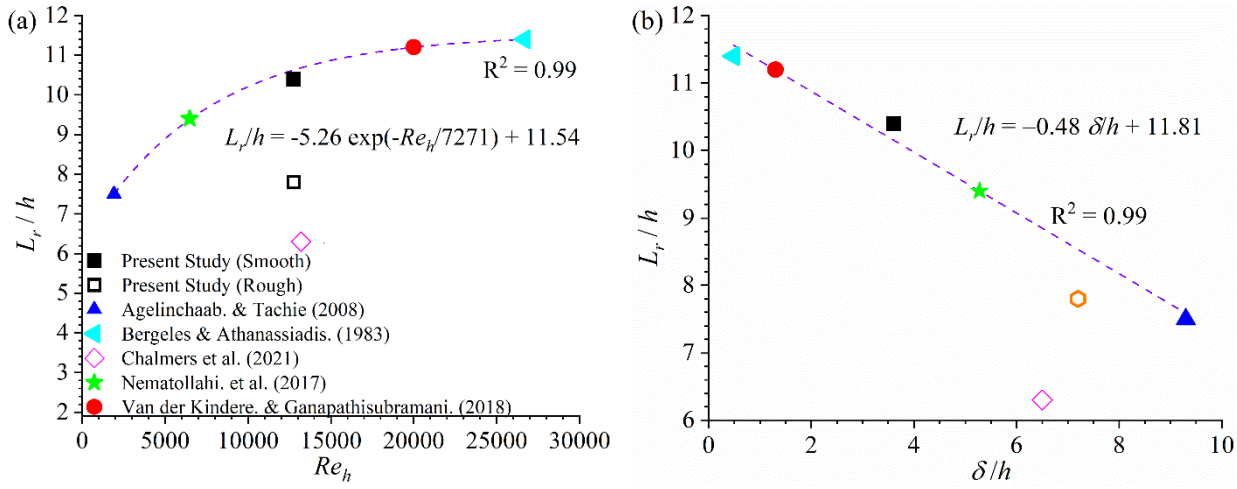

Figure 3.2.2: Variation of the mean recirculation length L_r downstream of wall-mounted cylinders with (a) Reynolds number, Re_h, and (b) relative boundary layer thickness δ/h. The hollow symbols indicate test cases employing rough walls. The dashed lines are fitted functions for the smooth data.

Figure 3.2.3 shows the variation of mean recirculation length with gap ratio for the smooth and rough wall cases. As the gap ratio increases, the value of the mean recirculation length decreases monotonically. This is in agreement with the observations by Durão et al. (1992), Panigrahi (2009) and Wang & Tan (2008). It is also noted from Figure 3.2.3 that as the gap ratio increases, the difference between the mean recirculation length for the smooth and rough cases diminishes. This is expected since as the cylinder gets further away from the wall, the wake flow is less susceptible to the roughness condition on the bottom wall. In particular, the values of L_r for the S2 and R2

cases are both $0.6h$, and agree well with Portela et al. (2017) and Durão et al. (1988) for square cylinders immersed in uniform flows over a wide range of Reynolds numbers. This observation implies that the mean flow for the largest gap ratio ($G/h = 2.0$) is similar to previous results for square cylinders in uniform flows, and the incoming TBL over either smooth or rough walls does not affect the mean flow separation induced by the cylinder.

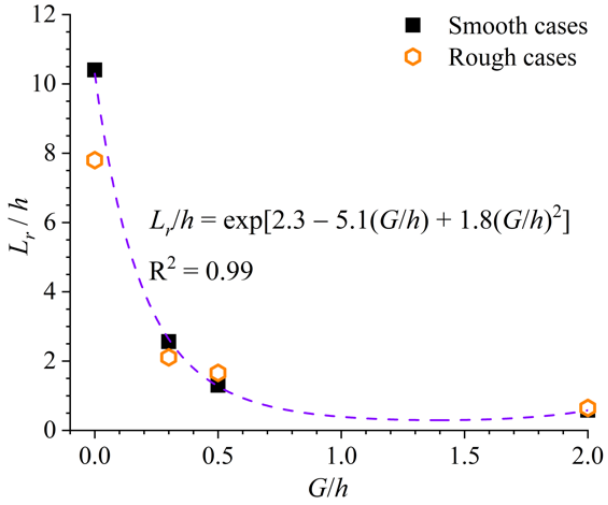

Figure 3.2.3: Variation of the mean recirculation length, L_r, with the gap ratio G/h for the smooth and rough wall cases.

3.3 Reynolds stresses

Figure 3.3.1 shows the contours of the streamwise Reynolds normal stress ($\overline{u'u'}$). The separated shear layers also manifest as regions of elevated $\overline{u'u'}$, and the streamwise extent of the elevated $\overline{u'u'}$ decreases as the gap ratio increases. This is consistent with the shorter mean recirculation bubble for larger gap ratios (see Figure 3.2.3). Additionally, the maximum magnitudes of $\overline{u'u'}$ in the upper shear layers are larger than those in the lower shear layers for the cases of $G/h = 0.3$

and 0.5, and the discrepancy in the maximum magnitudes of $\overline{u'u'}$ of the upper and lower shear layers in the R0.3 and R0.5 cases are apparently larger than those in the counterpart smooth cases. This implies that wall roughness imposes a stronger asymmetry in the streamwise Reynolds normal stresses. In the case of $G/h = 2.0$, the levels of $\overline{u'u'}$ are nearly symmetrical about the vertical centerline of the bluff body, and are nearly independent of wall roughness, as observed also for the mean flow field in Figures 3.2.1g and 3.2.1h.

Figure 3.3.2 compares the contours of the vertical Reynolds normal stress ($\overline{v'v'}$) for all test cases. In general, as the gap ratio increases, the peak $\overline{v'v'}$ increases in magnitude and its location moves closer to the leeward face of the cylinder. For instance, the maximum $\overline{v'v'}$ in the S0.5 and R0.5 cases are approximately 3.4 and 1.8 times higher than the values of the S0.3 and R0.3 cases, respectively. By comparing Figures 3.3.1 and 3.3.2, it is noted that the peak values of $\overline{u'u'}$ are generally larger than those of $\overline{v'v'}$ for the S0.3, R0.3 and R0.5 cases but $\overline{v'v'}$ dominates over $\overline{u'u'}$ in the cases of S0.5, S2, and R2.

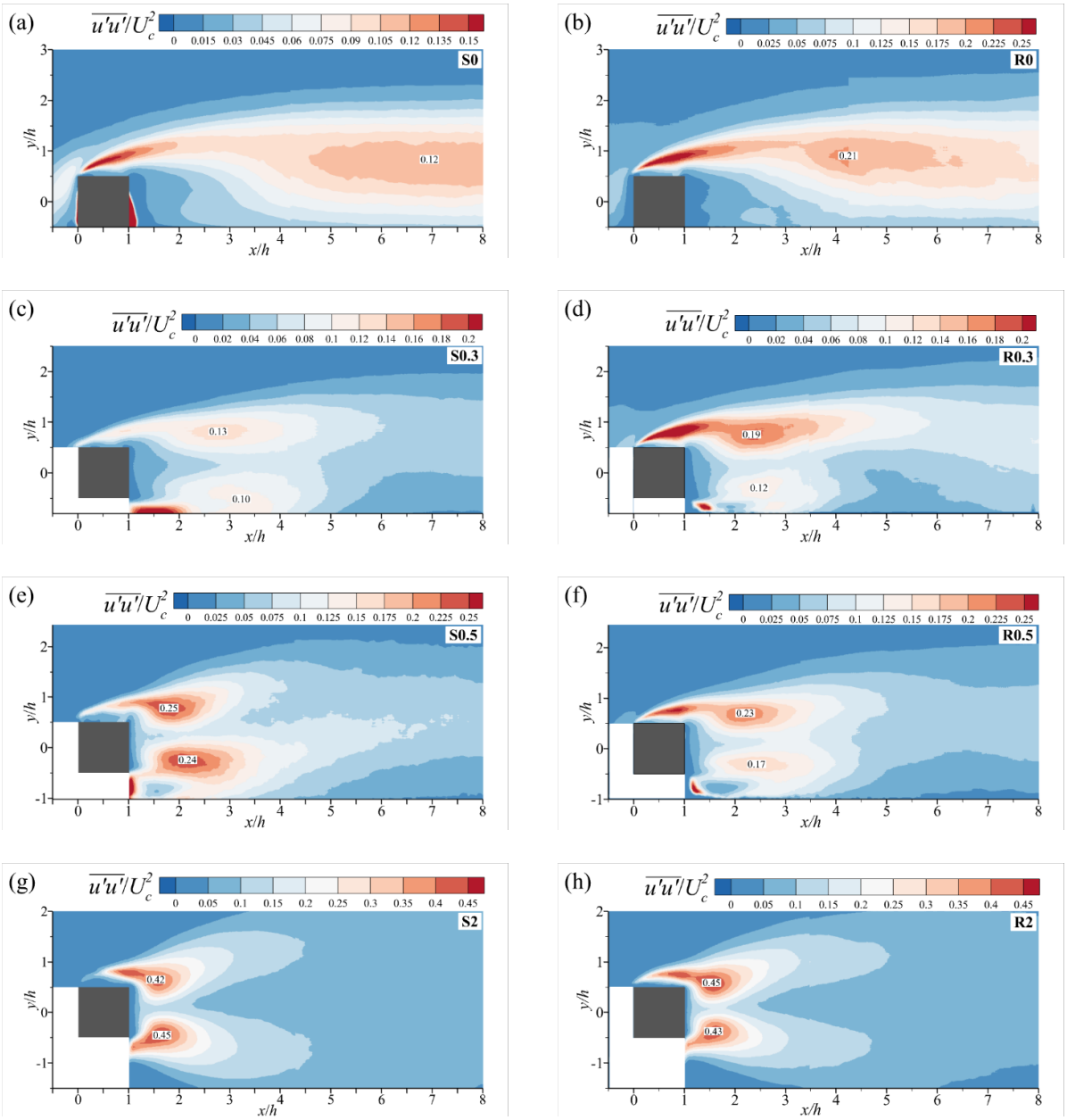

Figure 3.3.1: Contours of the streamwise Reynolds normal stress ($\overline{u'u'}$) for the cases of $G/h =$ (a, b) 0.0, (c, d) 0.3, (e, f) 0.5 and (g, h) 2.0 with smooth (a, c, e, g) and rough (b, d, f, h) wall conditions.

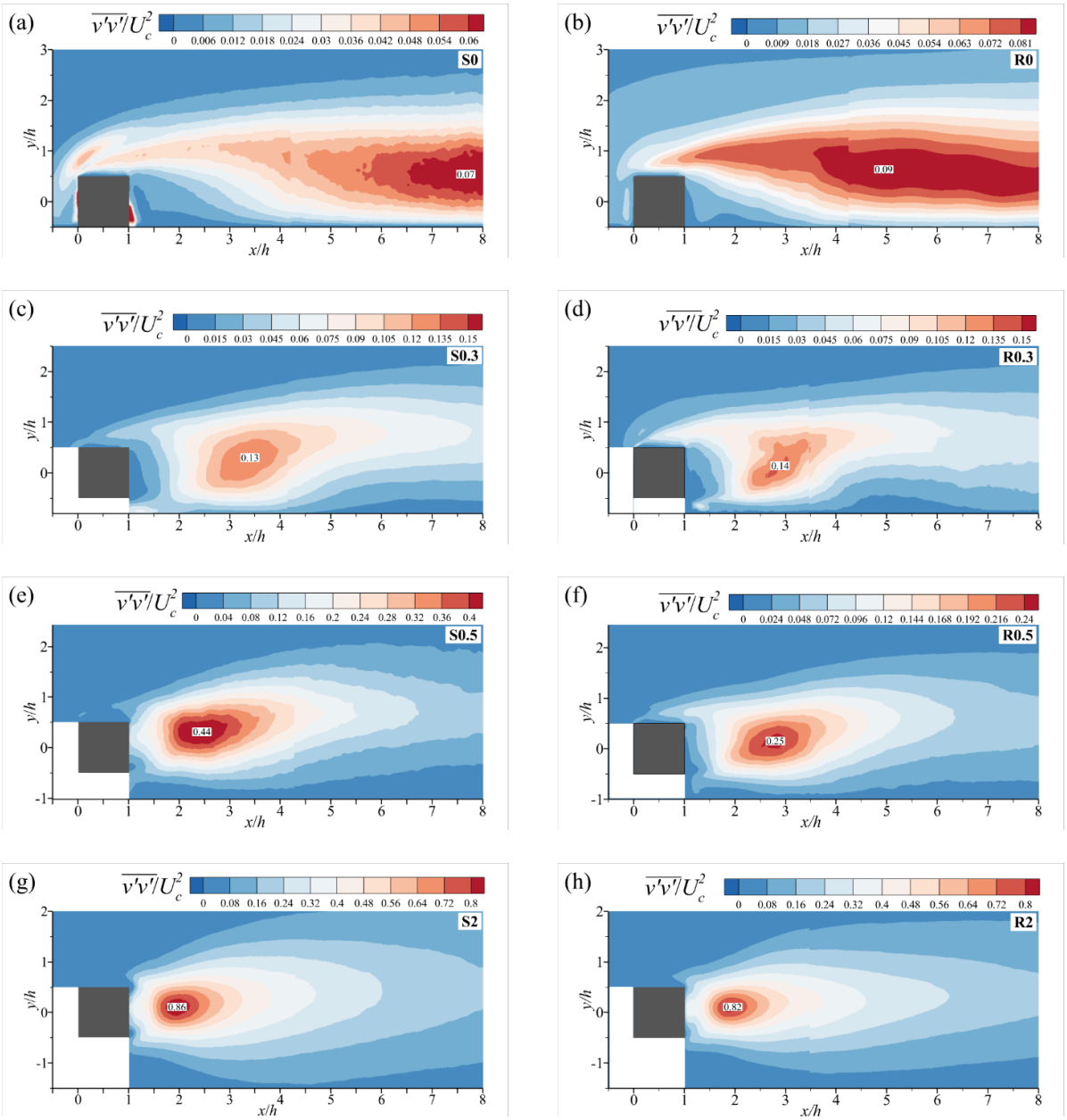

Figure 3.3.2: Contours of the vertical Reynolds normal stress ($\overline{v'v'}$) for the cases of G/h = (a, b) 0.0, (c, d) 0.3, (e, f) 0.5 and (g, h) 2.0 with smooth (a, c, e, g) and rough (b, d, f, h) wall conditions.

3.4 Coherent structures

In this section, the spatio-temporal characteristics of the vortical structures in the wake region behind the cylinders are examined exploiting the time-resolved whole-field measurement. Figure 3.4.1 compares the frequency spectra of the vertical fluctuating velocity at the peak location of $\overline{v'v'}$ for the offset cases, as denoted by the location of the labels in Figure 3.3.2. In general, the spectra at high frequencies (say $St > 0.5$) exhibit a slope of -5/3 for all test cases. This signifies the existence of inertial subrange at the present high Reynolds number. Differences in spectra for the different test cases are confined to the low frequencies (i.e., below the order of U_c/h). The similarity in the spectra at higher frequencies is consistent with the notion that the small scales tend to be universal. As seen in Figure 3.4.1a, the spectrum in the S2 case possesses a sharp peak at $St = 0.129$, and a less prominent peak at its second harmonic ($St = 0.396$). This dominant frequency at $St = 0.129$ agrees well with 0.129, 0.133 and 0.140 reported, respectively, by Durão et al. (1991), Bosch et al. (1996) and Martinuzzi et al. (2003). It is also evident in Figure 3.4.1 that, compared to the S2 case, the spectrum in the R2 case exhibits a relatively broader peak at a higher frequency, and the harmonic does not manifest. This suggests that for the cases of $G/h = 2.0$, even though wall roughness does not influence the mean flow and Reynolds stresses (see Figures 3.2.1, 3.3.1 and 3.3.2) the incoming turbulence intensity imposed by the wall roughness alters the vortex shedding motion behind the cylinder to some extent. As for the cases of $G/h = 0.3$ and 0.5, the dominant frequencies in the rough cases are consistently higher than those in the smooth case, and also possess broader peaks. In particular, the spectrum in the R0.3 case exhibits a peak at $St = 0.177$ which is not as distinct as the other test cases.

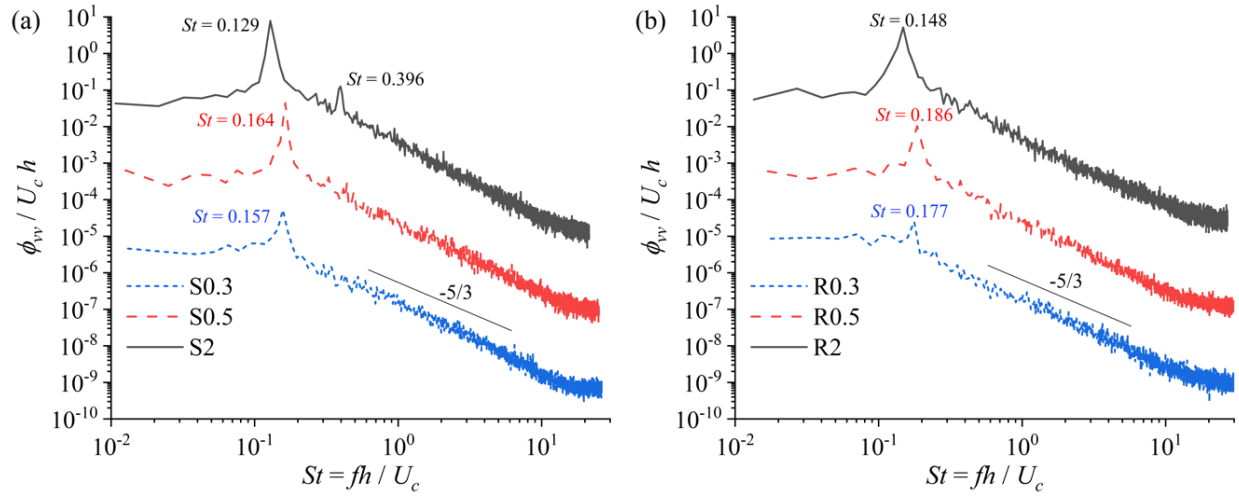

Figure 3.4.1: Frequency spectra of the vertical fluctuating velocities at the location of maximum $\overline{v'v'}$ *for the (a) smooth and (b) rough wall cases. To facilitate visualization, the characteristic peak frequencies are marked, and the spectra are offset by two orders of magnitudes for different cases.*

Table 3.4.1. Dominant frequencies in different test cases using different velocity scales

G/h	Smooth cases		Rough cases	
	St	St_∞	St	St_∞
0.3	0.157	0.119	0.177	0.099
0.5	0.164	0.130	0.186	0.109
2.0	0.129	0.119	0.148	0.109

Table 3.4.1 compares the dominant frequencies scaled by the incoming centerline mean velocity and freestream velocity for the offset cases. It is interesting to see that compared with St based on

U_c, the Strouhal numbers scaled by U_∞ for different gap ratios are consistent. Specifically, the dominant St_∞ for $G/h \in [0.3, 2.0]$ are between 0.119 and 0.130 for the smooth cases and 0.099 and 0.109 for the rough cases. A shift in *St* from 0.119 to 0.130 represents a change in frequency from 2.43 Hz to 2.65 Hz and represents a percent difference of 8.3%, which is approximately consistent between cases. These results agree with the conclusions by Martinuzzi et al. (2003), Durão et al. (1991) and Bosch et al. (1996) that the dominant Strouhal number does not change once vortex shedding occurs at large enough gap ratios. In contrast to wall-mounted bluff bodies in deep TBL for which the mean velocity of the incoming TBL at the bluff body height is the appropriate velocity scale (Castro 1979, Fang & Tachie 2019a, 2019b, 2020), the similarity in St_∞ for the rough wall cases clearly indicates that the freestream velocity is the appropriate velocity scale for offset cylinders even with a large relative boundary layer thickness.

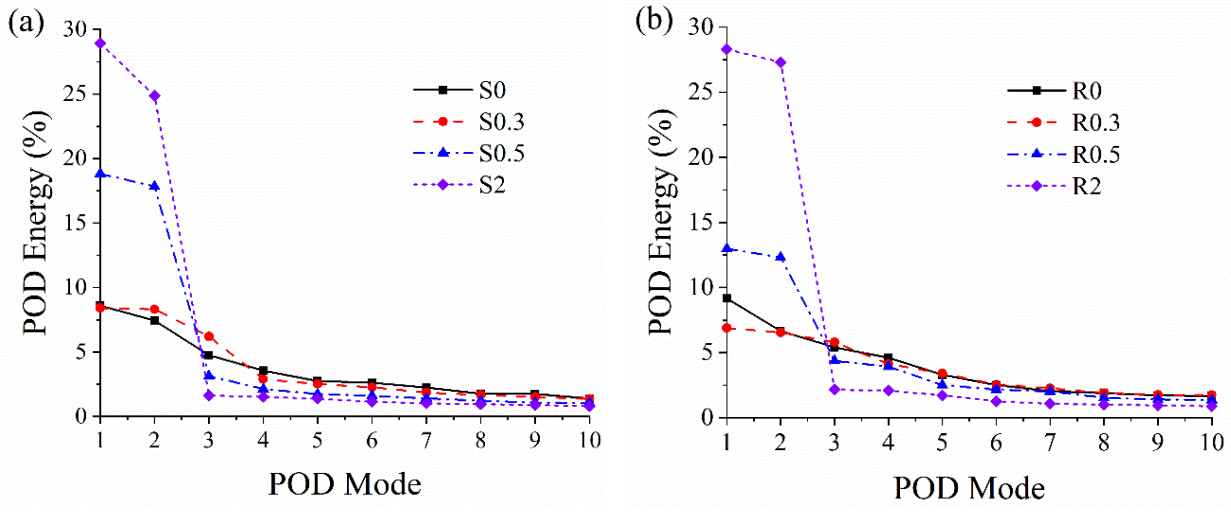

Figure 3.4.2: Energy distributions among the first 10 POD modes for the (a) smooth and (b) rough wall cases.

Table 3.4.2. Relative contribution [%] to the TKE by the streamwise (u') and vertical (v') components of the first four POD modes for the offset cases. The values in brackets indicate the contribution [%] from u' and v' to the pertinent POD mode energy.

Mode / Cases	1		2		3		4	
	u'	v'	u'	v'	u'	v'	u'	v'
S0.3	6.3(74.3)	2.2(25.7)	6.2(75.1)	2.1(24.9)	6.0(96.9)	0.2(3.1)	2.7(94.2)	0.2(5.8)
S0.5	6.0(31.8)	12.8(68.2)	5.1(28.7)	12.7(71.3)	2.4(77.9)	0.7(22.1)	1.4(66.9)	0.7(33.1)
S2	7.3(25.2)	21.6(74.8)	6.8(27.5)	18.0(72.5)	1.2(73.6)	0.4(26.4)	0.4(27.4)	1.1(72.6)
R0.3	5.1(93.5)	1.8(6.5)	6.1(92.9)	0.5(7.1)	5.6(96.7)	0.2(3.3)	4.0(97.1)	0.1(2.9)
R0.5	3.7(28.3)	9.3(71.7)	4.3(34.9)	8.0(65.1)	3.4(78.9)	0.9(21.1)	3.3(83.2)	0.7(16.8)
R2	8.5(30.1)	19.8(69.9)	7.0(25.6)	20.3(74.4)	0.6(27.0)	1.6(73.0)	0.6(26.8)	1.5(73.2)

To further elucidate the vortical structures in the wake region, proper orthogonal decomposition (POD) was performed using the snapshot POD method proposed by Sirovich (1987). Details of the POD algorithm implementation can be found in Fang & Tachie (2019b). In the framework of POD, it is typical that adjacent ranks of modes pair with each other to describe a convective structure like the vortex shedding motion (Fang & Tachie 2019a; Noack et al. 2003). As outlined by Riches et al. (2018) for the vortex shedding motion in uniform flow, two POD modes form a pair when the following three conditions are satisfied: (1) they possess similar energy content, (2) the temporal coefficients are shifted by 90° in phase; (3) the quasi-periodical spatial structures are shifted by a quarter wavelength. These three conditions are examined subsequently to determine existence (or lack thereof) of POD mode pairs in the present context of vortex shedding motion subjected to wall confinement.

Figure 3.4.2 presents the relative energy distributions of the first 10 POD modes for different test cases. For the cases of $G/h = 0.5$ and 2.0, a drastic reduction in energy occurs as the mode rank increases beyond two. For instance, the first two POD modes of the S2 and R2 cases are significantly more energetic than the remaining POD modes, containing approximately 55% of the total POD energy. This emphasizes the dominance of vortex shedding motion for the large gap ratio cases. For the $G/h = 0.0$ and 0.3 cases, on the other hand, the POD mode energy exhibits a

relatively gradual decay as the mode rank increases. This implies that the coherent structures in the cases of $G/h = 0.0$ and 0.3 possess a wider range of scales than the cases of higher gap ratios, and may be attributed to the strong perturbation of the wake flows by the incoming turbulence (see Figure 3.1.1b). It is also observed in Figure 3.4.2 that with an upstream rough wall, the relative energy content of the first POD mode is larger for the $G/h = 0.0$ case than the $G/h = 0.3$ case. The energy percentages of the first 2 POD modes in the S0.5 case are 10% smaller than the R0.5 case, but the differences in the energy of the first 2 POD modes for the other gap ratios are all less than 5%.

Table 3.4.2 breaks down the individual energy contributions (in terms of percentages) from the streamwise (u') and vertical (v') velocity components for the first four POD modes. In the cases of S2 and R2, the vertical fluctuating velocity, v', contributes the majority (approximately 70%-75%) of energy towards the first two POD modes. It is interesting to note that the contribution of v' for the third and fourth POD mode energies is similar (approximately 73%) for the R2 case, but drastically different for the S2 case. It is thus concluded that the effects of wall roughness in the S2 and R2 cases are still at play but limited to higher ranks of POD modes. In the cases of S0.5 and R0.5, the contribution percentages by v' for the first two POD modes are smaller with greater disparity compared to the cases of S2 and R2. This reflects the attenuation of vertical fluctuating velocity imposed by wall confinement for smaller gap ratios. For the third and fourth POD modes in the cases of S0.5 and R0.5, however, the dominant contribution to mode energy is from the streamwise fluctuating velocity u'. As the gap ratio reduces to 0.3, the first four POD mode energies are dominated by u'. This generally agrees with the observation from Figures 3.3.1 and 3.3.2 that the peak values of $\overline{u'u'}$ are larger than those of $\overline{v'v'}$ in the cases of S0.3 and R0.3.

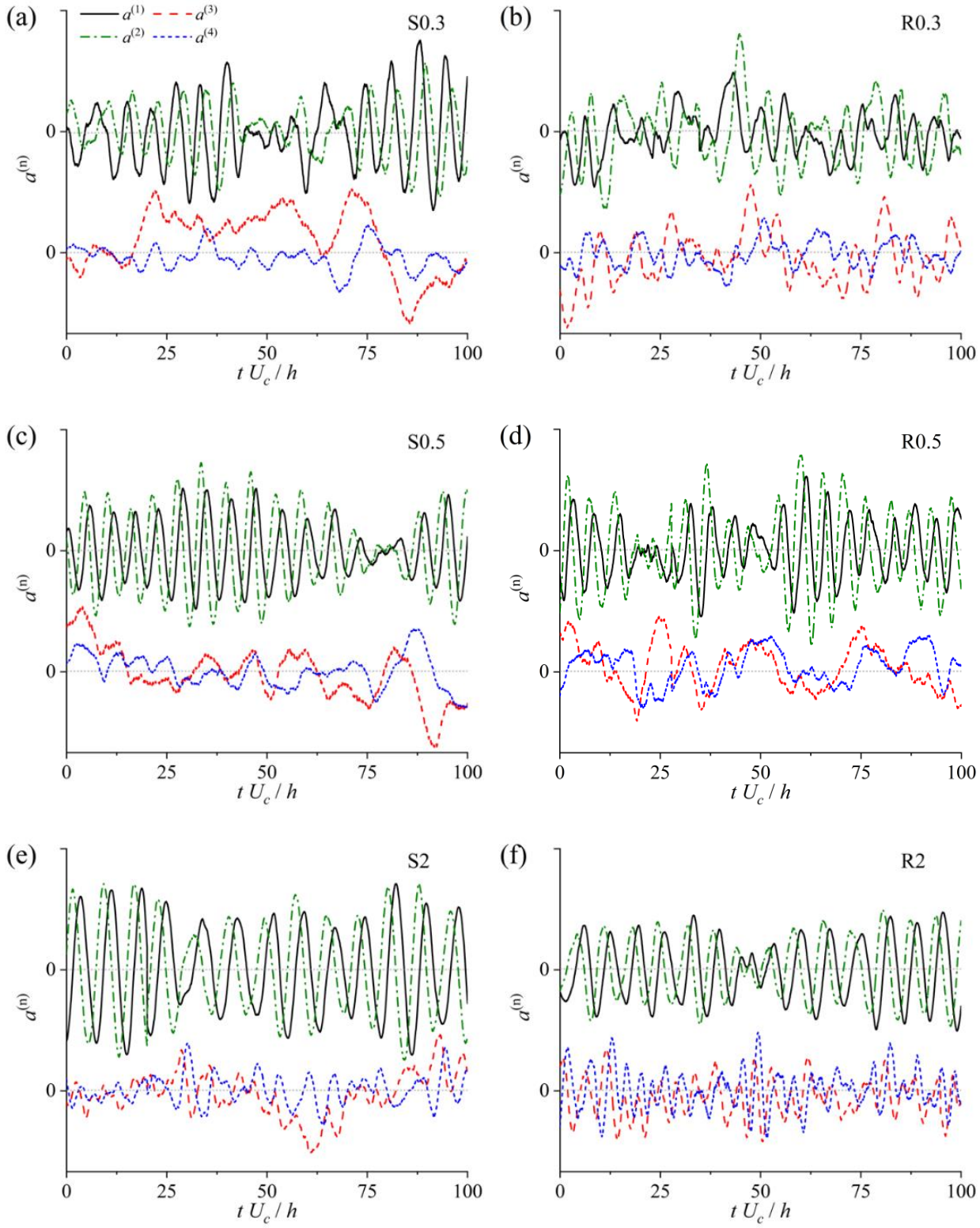

Figure 3.4.3: Temporal variation of the first four POD mode coefficients for the offset cases.

Figure 3.4.3 compares the temporal variations of the first four POD modes coefficients ($a^{(i)}$ with i = 1, 2, 3 and 4, respectively) in the offset cases. As seen in Figure 3.4.3e for the S2 case, both $a^{(1)}$ and $a^{(2)}$ exhibit distinct sinusoidal patterns and their phase difference is near a quarter of periodicity (i.e., 90°). This is a typical manifestation of vortex shedding motion. In accordance with Figures 3.4.3f, $a^{(1)}$ and $a^{(2)}$ in the R2 case also possess offset sinusoidal patterns, but with stronger amplitudes variation compared with the S2 case. For instance, both $a^{(1)}$ and $a^{(2)}$ skip a periodicity near time $t = 45U_c/h$. This is attributed to a temporary suppression (or intermittency) of vortex shedding motion. This is reminiscent of the observations by Bai & Alam (2018) and Bailey et al. (2002) that for a square cylinder in a uniform flow, the regular vortex shedding motion is interrupted as the shear layer intermittently reattaches on the side surfaces. An inspection (not shown here) of longer duration of $a^{(1)}$ and $a^{(2)}$ in the S2 and R2 cases reveals that the intermittency of vortex shedding motion is more likely to occur in the rough wall case. This is not surprising, since the stronger incoming turbulence intensity imposed by wall roughness (see Figure 3.1.1b) inevitably exerts a stronger influence on the wake flow dynamics compared with the smooth case counterpart. It is also interesting to note in Figures 3.4.3e and 3.4.3f that a similar pattern of phase-shifted sinusoidal variation of $a^{(3)}$ and $a^{(4)}$ is also observed in the R2 case, but not in the S2 case. This implies that the third and fourth POD modes are also paired in the R2 case, but not in the S2 case. This also agrees with the observation from Table 3.4.2 that at G/h = 2.0, roughness effects manifest in the third and fourth POD modes. Overall, for the cases of G/h = 2.0, wall roughness disturbs the periodic vortex shedding motion signified by the first two POD modes, but prompts an additional pairing mechanism amongst the third and fourth POD modes. It is also noted in Figure 3.4.3 that the pairing between the first two POD modes in the cases of S0.5, R0.5 and S0.3 is discernable to varying degrees. In general, both wall roughness and smaller gap ratios promote

intermittent vortex shedding motion signified by the first two POD modes. Additionally, it is a consistent pattern that when $a^{(1)}$ and $a^{(2)}$ temporally diminish, the magnitudes of $a^{(3)}$ and $a^{(4)}$ increases momentarily. This is indicative of the modulation of smaller-scale structures (higher ranks of POD modes) by the vortex shedding motion. As seen in Figure 3.4.3b, no pairing of POD modes is discernable for the R0.3 case.

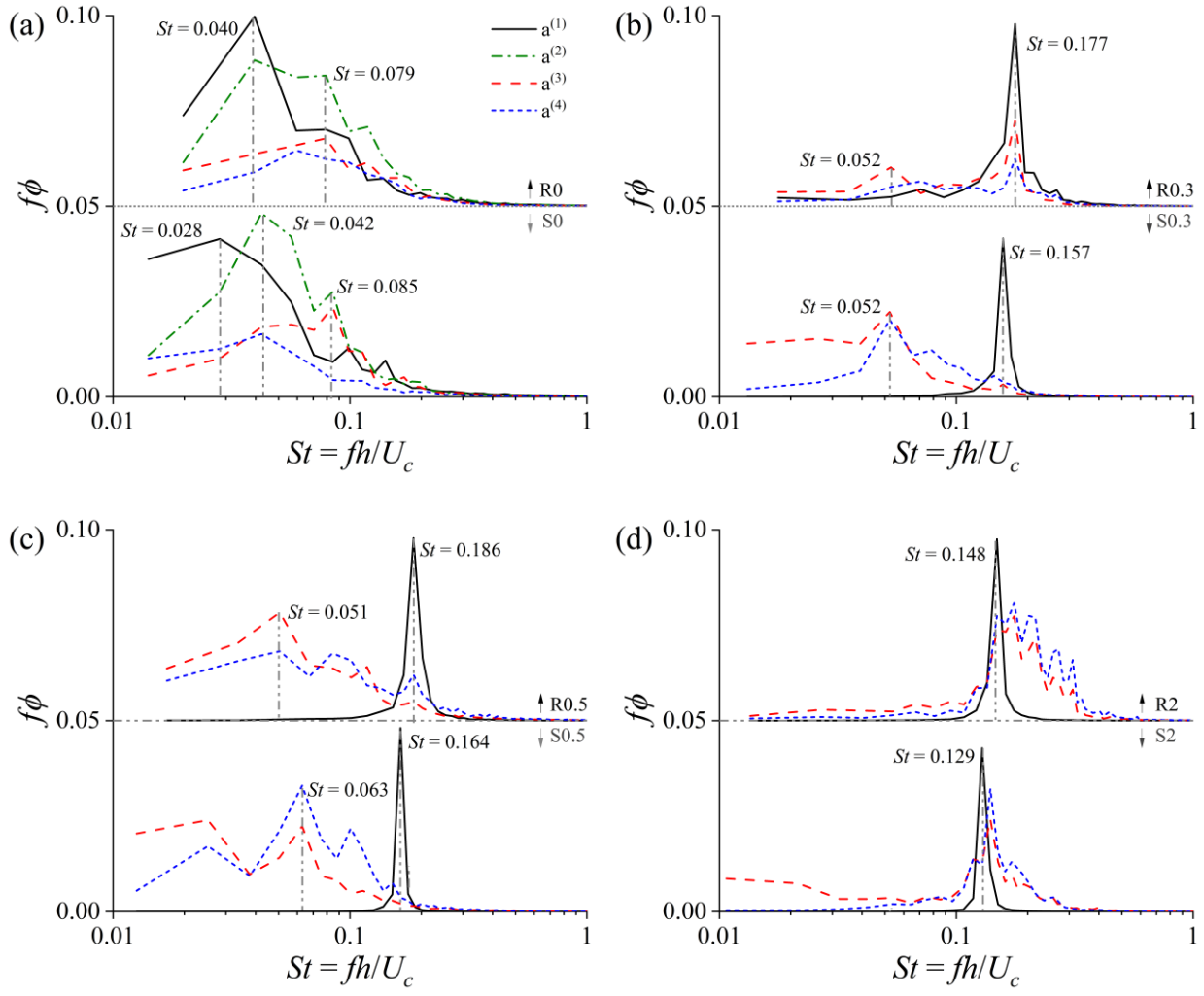

Figure 3.4.4: Premultiplied frequency spectra of the coefficients of the first four POD modes for the cases of G/h = (a) 0.0, (b) 0.3, (c) 0.5 and (d) 2.0.

Figure 3.4.4 compares the frequency spectra of the coefficients of the first four POD modes for different test cases. From Figure 3.4.4a, the first POD modes in the smooth and rough wall-mounted cases possess dominant frequencies of $St = 0.028$ and 0.040, respectively. Both of these frequencies are similar to dominant/subdominant frequencies in the incoming TBL (see Figure 3.1.2). In other words, the first POD mode in the wall-mounted cases mirrors the dominant frequency residing in the incoming TBL that the cylinder is exposed to. This is reminiscent of the observations by Fang & Tachie (2019a, 2019b, 2020) that the separation bubble over wall-mounted bluff bodies interacts with the large-scale motion embedded in the TBL so that it mirrors the characteristic frequency in the TBL. As seen in Figure 3.4.4b-3.4.4d for the offset cases, the first two POD modes possess sharp peaks at the same frequencies reported in Table 3.4.1 based on Figure 3.4.1. The third and fourth POD modes in the R0.3 and R0.5 cases exhibit a distinct peak centered around St = 0.05, which is similar to the characteristic frequency of the incoming TBL (see Figure 3.1.2). The third and fourth POD modes in the S0.3 and S0.5 cases, on the other hand, exhibit different peak frequencies compared with the corresponding incoming TBL shown in Figure 3.1.2. From Figure 3.4.4d, the third and fourth POD modes in the cases of G/h = 2.0 exhibit broader peaks at frequencies higher than the first two POD modes. In summary, for the wall-mounted case, the characteristic frequencies of the incoming TBL imprints in the first POD mode regardless of wall roughness condition. For offset cases with an upstream smooth wall, the characteristic frequencies of POD modes are not influenced by the incoming TBL. With an upstream rough wall, on the other hand, the characteristic frequencies of the incoming TBL manifests at higher (third and/or fourth) ranks of POD modes only at relatively small gap ratios (G/h = 0.3 and 0.5).

Figures 3.4.5 and 3.4.6 examine the first four POD modes for the two extreme offset cases, i.e., G/h = 2.0 and 0.3, respectively. As seen in these two figures, the first two POD modes in the cases of S2, R2 and S0.3 exhibit a pattern typical of vortex shedding behind a bluff body in uniform flows. Specifically, a train of alternating positive and negative vortical structures are aligned near the centerline behind the cylinder in the first mode, while the second mode is fairly similar to the first mode except for a downstream shift of a quarter of wavelength. As such, the three conditions required for POD mode pairs, as proposed by Riches et al. (2018), are satisfied by the first two POD modes in the cases of S2, R2 and S0.3. It is noted that the first two modes in the S0.3 case are clearly skewed upwards, reflecting the deflection of trajectory of shed vortices away from the bottom wall. This is because the shed vortex grows in size while being convected downstream, so that its core moves farther away from the wall. This skewed vortex shedding motion was also observed by Samani & Bergstrom (2015) for a near wall square cylinder. In the R0.3 case, on the other hand, the topologies of first two modes do not conform to typical vortex shedding motion even though the velocity spectra (Figure 3.4.1b) and spectra of POD mode coefficients (Figure 3.4.4b) exhibit identical peak frequency. As such, the first two POD modes for R0.3 cannot be considered as mode pairs. A close inspection on Figures 3.4.6b and 3.4.6d reveals that the sizes of elevated mode velocities near the wall are clearly smaller than those downstream of the upper trailing edge. As for the third and fourth POD modes, the similarity of the topology is discernable in the R2 case, but not in the S2 case. In accordance with Figures 3.4.2-3.4.5, the third and fourth POD modes in the R2 case also meet the three conditions outlined by Riches et al. (2018). The above analysis is further supported by the temporal trajectories of the first and second POD mode pairs presented in Figure A.1 of the appendix. Additionally, a discussion of the phase-averaged Reynolds normal stresses is presented in Figures A.2 and A.3 of the appendix.

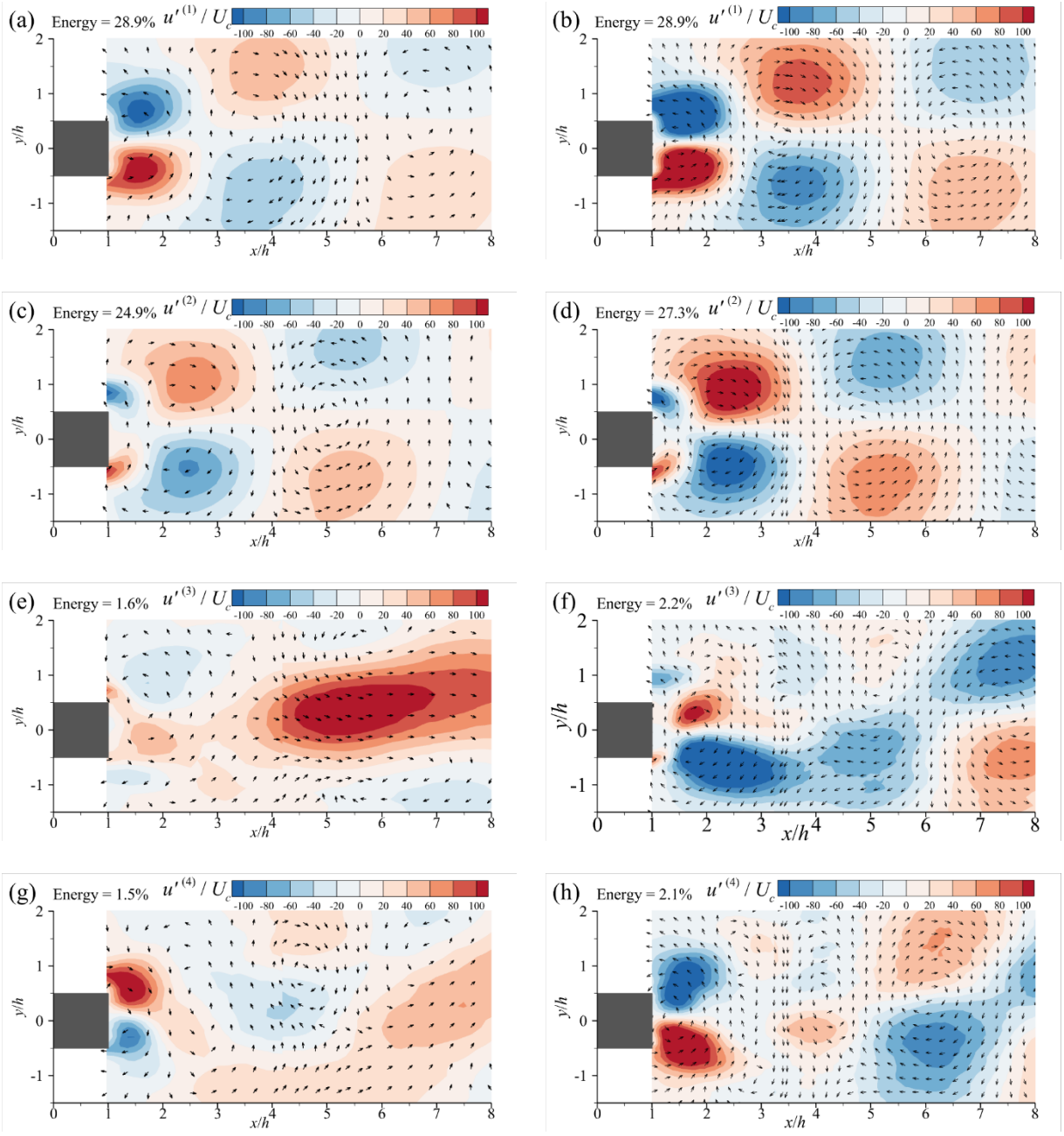

Figure 3.4.5: Contours of the first four POD modes for the (a, c, e, g) S2 and (b, d, f, h) R2 cases.

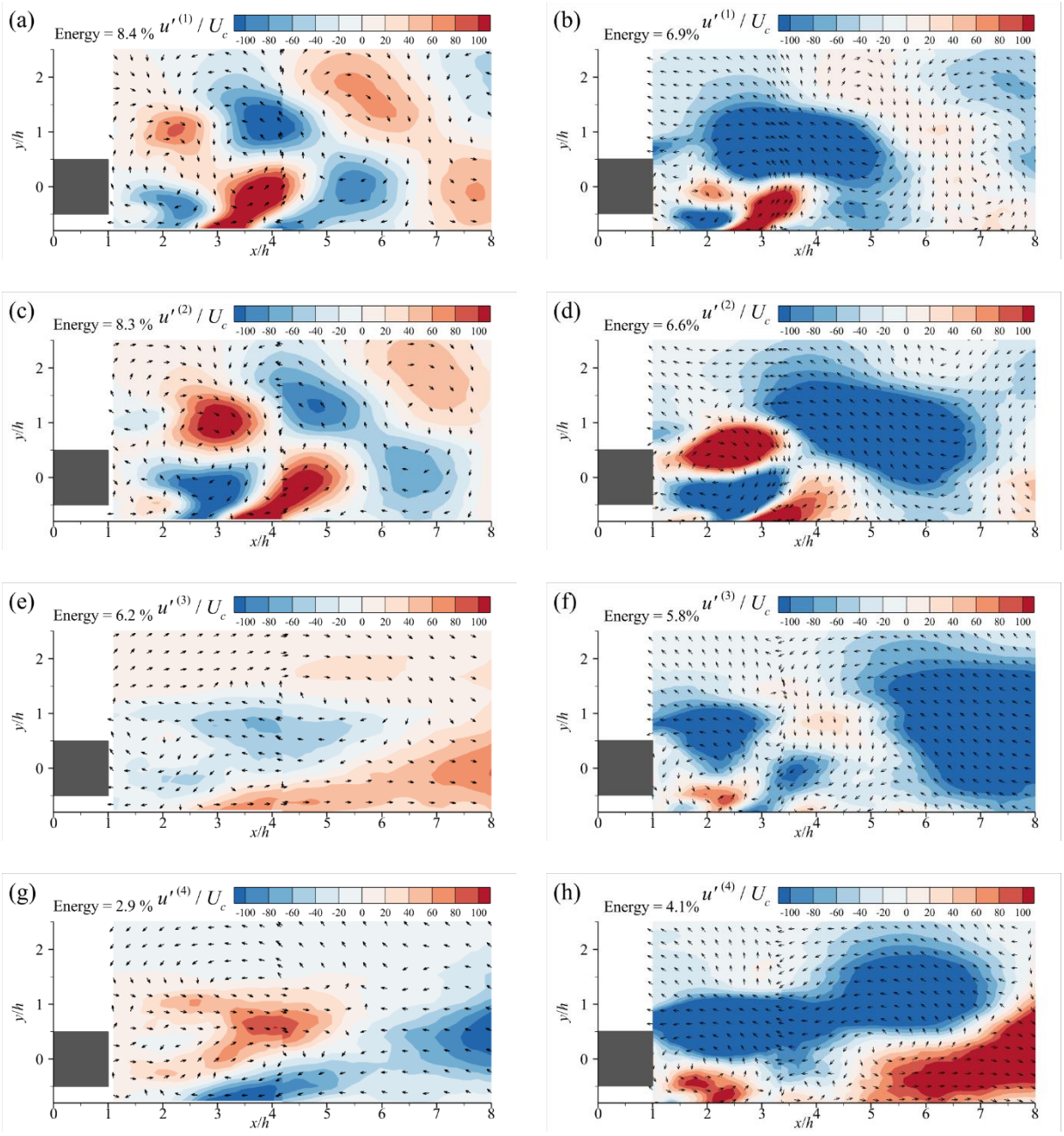

Figure 3.4.6: Contours of the first four POD modes for the (a, c, e, g) S0.3 and (b, d, f, h) R0.3 cases.

Figure 3.4.7 compares the temporal spanwise vorticity variations of the reconstructed fluctuating velocity fields based on the first two POD modes for the S0.3 and R0.3 cases. Note that the mode

coefficients at the indicated times are the same as those fromFigure 3.4.3, and at instances when the mode coefficients are attenuated (i.e. Figures 3.4.3g, i, k), the vorticity is multiplied by a factor of five for visibility. As seen in Figures 3.4.7a, two areas of amplified negative vorticity exist downstream of the upper and lower trailing edges (around $x/h = 2.0$). These two areas of negative vorticity signify the independent and synchronized rollup of upper and lower shear layers. As time evolves (Figure 3.4.7c), these two areas of negative vorticity are convected downstream and merge together to form a large vortex downstream of the cylinder (around $x/h = 2.5$). As seen in Figures 3.4.7e and 3.4.7g, the merged area of negative vorticity near the cylinder centerline in Figure 3.4.7c is subsequently stretched away from the wall, and another area of negative vorticity is induced near the wall (at $x/h \approx 4.0$ in Figure 3.4.7g). It is also noted that another pair of local peaks of positive vorticity manifest downstream of the trailing edge in Figure 3.4.7c. The evolution of these patches of positive vorticity is typically similar to the aforementioned process for the negative vorticity patches. It is interesting to see in Figures 3.4.7g, 3.4.7i and 3.4.7k that the two areas of positive vorticity immediately downstream of the trailing edges do not merge as they are convected downstream. This is an exemplification of the intermittency of vortex shedding deduced from Figure 3.4.3. In other words, the occurance of vortex shedding relies on a mutual interaction of vorticity fluctuation originated from the upper and lower shear layers.

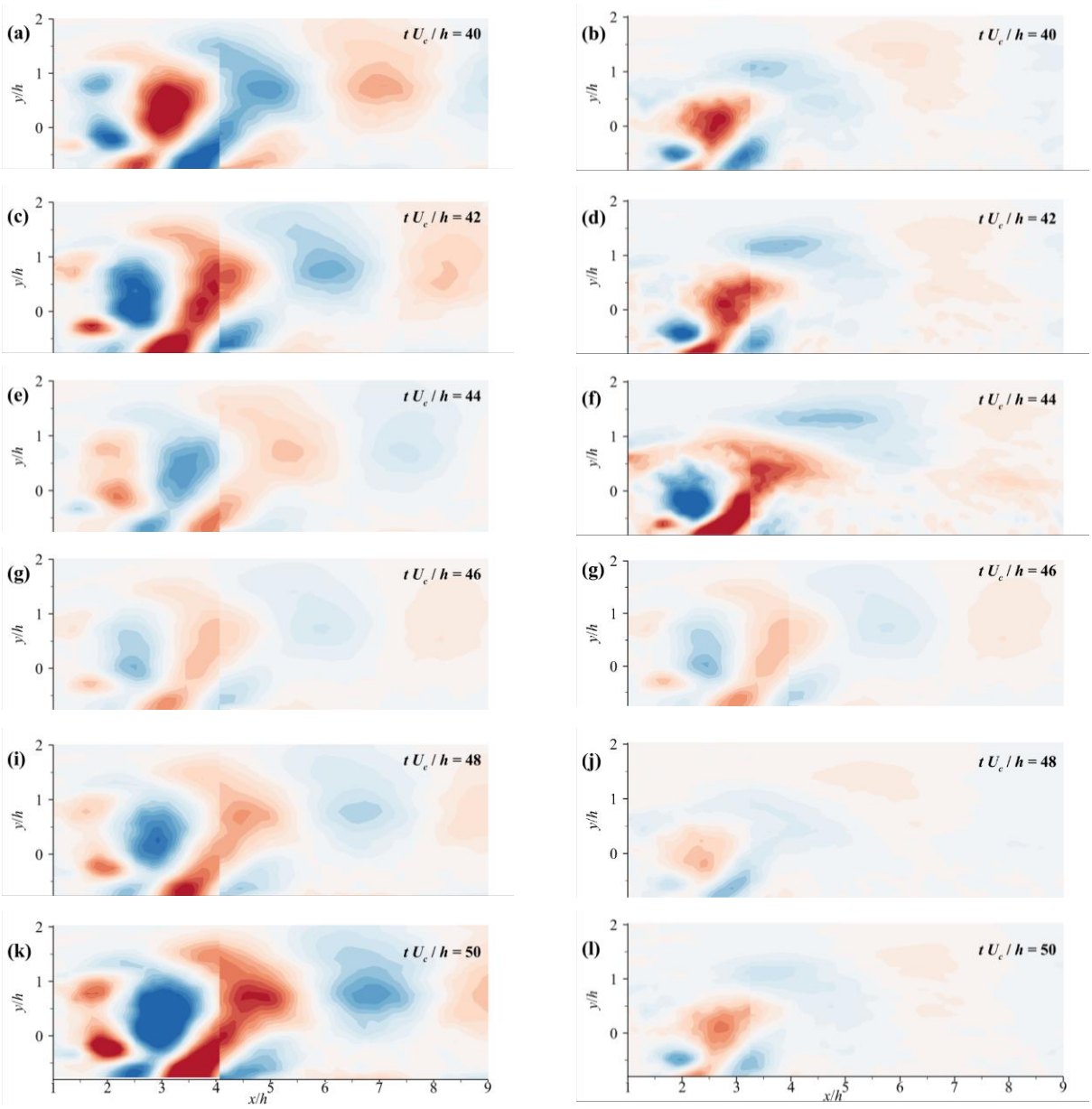

Figure 3.4.7: Typical temporal variation of spanwise vorticity field of the reconstructed fluctuating velocity fields based on the first two POD modes for the (left column) S0.3 and (right column) R0.3 cases. Negative and positive vorticities are shown in blue and red, respectively, while the magnitudes are reflected by the darkness. Note that the contour levels for (g, i, k) have been multiplied by a factor of five to make the vorticity visible.

This understanding is generally in line with the nonexistence of vortex shedding motion in the R0.3 case. Specifically, as seen in the right column of Figure 3.4.7, the patches of concentrated vorticity downstream of the upper and lower trailing edges are of drastically different sizes, and their interaction, as time evolves, is not discernable. Instead, small patches of strong alternating-signed vorticities are aligned downstream of the gap exit in the near-wall region. Meanwhile, the fluctuating vorticity above the upper surface elevation of the cylinder occurs in large areas that are elongated in the streamwise direction, and switch sign as time evolves. As such, in the R0.3 case, the fluctuating vorticity underlying the dominant coherent structure features drastically different spatio-temporal characteristics for the upper and lower shear layers, and consequently, in-phase interaction and regular vortex shedding motion are absent.

4.0 Gap Ratio Effects on the Coherent Structures Surrounding a Near-Wall Square Cylinder

In this chapter, the results and discussion from Chalmers, H., Fang, X., and Tachie, M.F., 2022, "Gap ratio effects on the coherent structures surrounding a near-wall square cylinder," submitted to the International Journal of Heat and Fluid Flow on November 18th, 2022 are presented.

4.1. Upstream Turbulent Boundary Layer

The characteristics of the upstream TBL are investigated using the vertical profiles of the mean velocity and $\overline{u'u'}$ Reynolds stress in Figure 4.1.1a as well as the frequency spectra in the vertical direction in Figure 4.1.1b. From Figure 4.1.1a, the mean velocity profile shows a TBL thickness of $\delta/h = 7.2$, and the centerline of each cylinder is submerged within the boundary layer for cases with $G/h \leq 4.0$. The magnitude of the turbulence intensity at the cylinder height is approximately twice as strong for the $G/h = 0.0$ case than the $G/h = 4.0$ case. This indicates that the level of incoming turbulence is much stronger for cases with cylinders closer to the bottom wall. From Figure 4.1.1b, below $y/h = 1.0$, there is significant energy at the low frequencies $0.02 < St < 0.05$. In the region of $1.0 < y/h < 3.0$, energy concentrates around $St = 0.05$. Above $y/h = 3$, the energy becomes significantly weaker. For instance, at the centerline of the $G/h = 8.0$ case, the incoming turbulence is weak and of indiscernible dominant frequency, i.e. white noise.

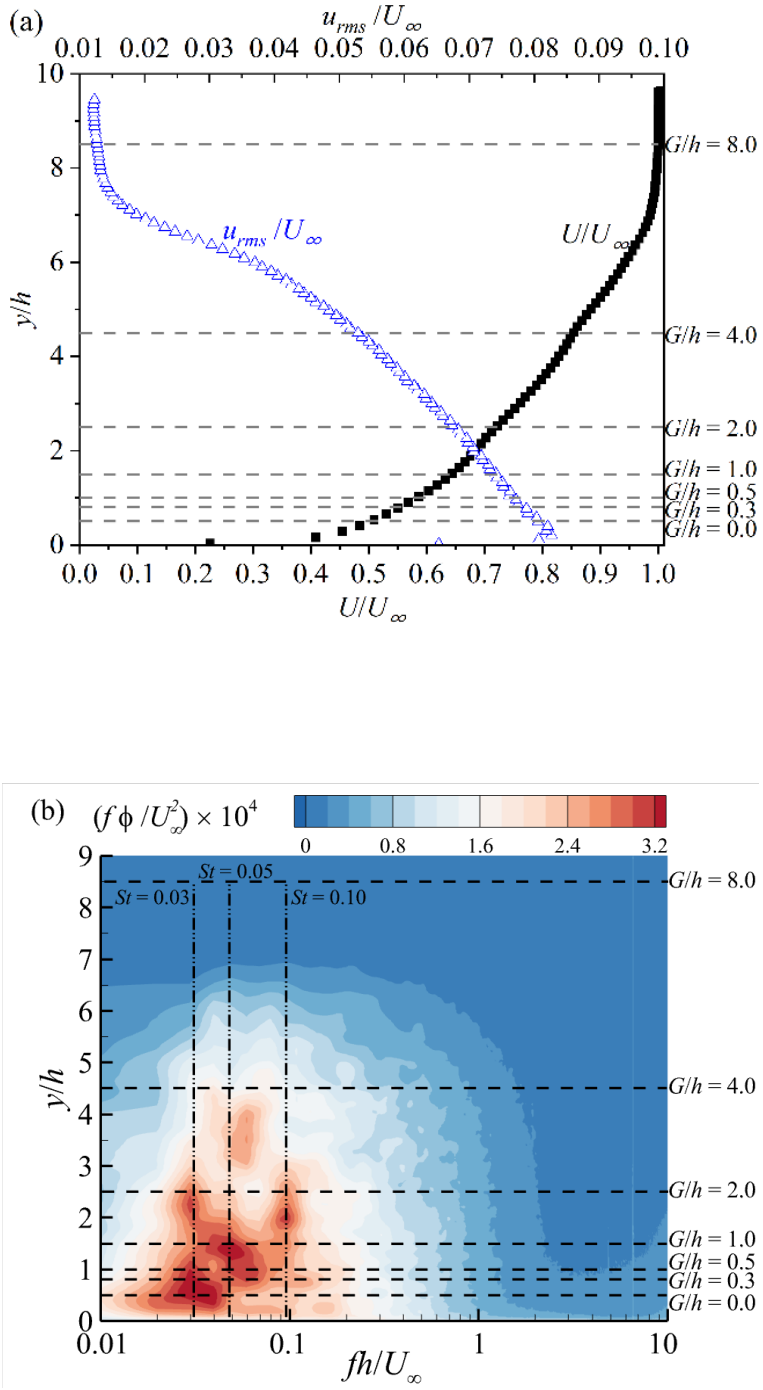

Figure 4.1.1: Vertical profile of the streamwise mean velocity and Reynolds normal stresses (a) and premultiplied frequency spectra of the streamwise velocity in the upstream TBL along the

vertical direction (b). The horizontal dashed lines represent the cylinder centerline for each test case.

4.2. Mean Flow and Turbulent Kinetic Energy

Figure 4.2.1 shows the contours of the streamwise mean velocity (U) for each test case with isopleths of 50% and 99% forward flow fractions, defined as the probability of positive instantaneous streamwise velocity, superimposed. The mean recirculation region is defined using the 50% forward flow fraction isopleth following the approach of Shi et al. (2010). Additionally, the isopleth of 99% forward flow fraction is employed to indicate the furthest extent of instantaneous flow recirculation. The furthest streamwise extents of the isopleths of 50% and 99% flow fractions are used to determine the mean recirculation length, L_r, and the permanent recirculation length, L_R, respectively.

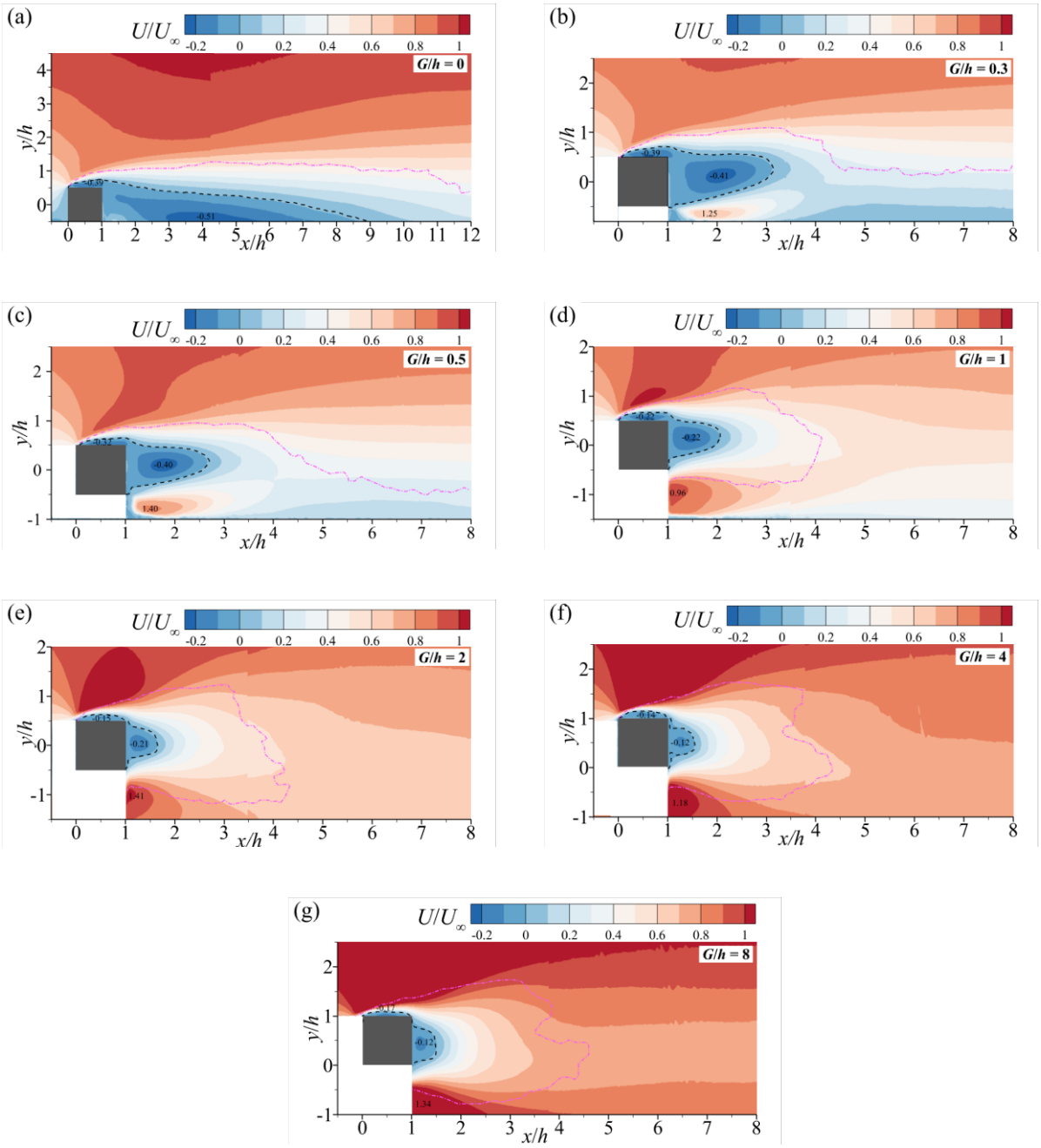

Figure 4.2.1: Contours of the streamwise mean velocity (U) for the various test cases superimposed with isopleths of the 50% *forward flow fraction (black dashed isopleth) and the* 99% *forward flow fraction (violet dash-dotted isopleth).*

The mean recirculation lengths for different test cases are plotted in Figure 4.2.2 along with available values from the literature. For each test case, there are distinct regions of flow reversal

above the cylinder and in the wake region. The mean recirculation length, L_r, increases as the gap ratio decreases. The lengthening of the recirculation region as the gap ratio decreases is widely reported (Durão et al. 1991; Panigrahi 2009; Shi et al. 2010; Chalmers et al. 2022), although the results shown in Figure 4.2.2 for the present study are larger than the values of $L_r = 1.5$ with $G/h = 0.8$, and $L_r = 0.6$ with $G/h = 1.0$ reported by Shi et al. (2010) and Panigrahi (2009) respectively. However, the present results agree with the values of $L_r = 2.9$ and 1.8 reported by Durão et al. (1991) for gap ratios of $G/h = 0.5$ and 3.3 respectively. Interestingly, the ratio of the boundary layer thickness to cylinder height is $\delta/h = 0.8$ in the studies by Shi et al. (2010) and Durão et al. (1991), indicating that the mean recirculation length is sensitive to a variety of flow parameters. For instance, in a uniform flow Lander et al. (2016) report an 11% increase in the recirculation length downstream of a square cylinder when the turbulence intensity increases from 1.0% to 6.5%. Therefore, the larger mean recirculation lengths observed in the present study for $G/h \leq 0.5$ are a result of the high intensity of incoming turbulence shown in Figure 4.1.1a. This is a departure from the linear dependence of the recirculation length behind wall-mounted square cylinders on the turbulent boundary layer thickness reported in Chalmers et al. (2022) for a variety of data sets (Bergeles & Athanassiadis, 1983; Agelinchaab & Tachie, 2009; Nematollahi et al., 2017; Van der Kindere & Ganapathisubramani, 2018).

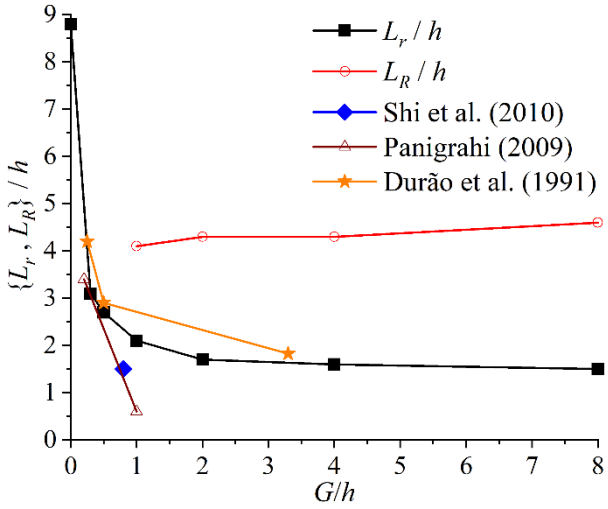

Figure 4.2.2: Variation of the mean recirculation length, L_r, and the permanent recirculation length, L_R, with gap ratio.

The 99% flow fraction isopleth reveals that when $G/h \leq 0.5$, there is intermittent reverse flow near the wall surpassing $x/h = 8.0$. This is reminiscent of the results by Shi et al. (2010) who reported the 80% forward flow fraction to extend past $x/h = 9.0$ in the streamwise direction. However, in similar fashion to the mean recirculation length, L_R remains nearly constant above $G/h = 1.0$ For $G/h \geq 1$, the 99% forward flow isopleth extends further in the streamwise direction in the upper and lower shear layers than it does along the cylinder centerline. According to Shi et al. (2010), this indicates a weakening interaction of the unsteady separation bubble with the intermittent large-scale VK vortex shedding motions in the upper and lower shear layers.

The maximum backflow behind the cylinder increases as the cylinder approaches the wall, to a maximum magnitude of$0.40U_\infty$. There is also a significant reduction in the magnitude of backflow as the gap ratio increases above $G/h = 0.5$ (45% reduction) and again as G/h increases above 2.0 (43% reduction). The maximum backflow above the cylinder decreases in magnitude

as the gap ratio increases between $0.5 < G/h < 2.0$. Meanwhile, the maximum velocity at the gap exit occurs at $G/h = 2.0$, indicating strong mean flow acceleration through the gap. Below this threshold gap size, the small gap restricts the flow, resulting in a velocity deficit near the wall as reported by Durão et al. (1991) for a gap size of $G/h = 0.25$, whereas above $G/h = 2.0$ flow acceleration through the gap diminishes.

To further investigate the flow acceleration through the gap, the probability density function (PDF) at the gap outlet is shown in Figure 4.2.3a. From the figure, the probability of positive fluctuation at the gap outlet is greatest for the $G/h = 0.3$ case. Furthermore, the possibility of high intensity negative velocity fluctuations is only shown for the $G/h = 0.3$ case as well. This indicates that the majority of the time the small gap size acts to accelerate the flow beneath the cylinder, although at certain instances, a mean recirculation region forms near the bottom wall. Above $G/h = 0.3$, the probability of high velocity fluctuations becomes unlikely. A similar analysis was done using the vertical velocity fluctuations at the point of furthest streamwise extent of the mean recirculation region to examine the behaviour of the wake flow. For the $G/h = 0.3$ and 0.5 cases, there is a low probability of high magnitude velocity fluctuations. Interestingly, as the gap ratio increases above $G/h = 1.0$, Figure 4.2.3b shows that both positive or negative high magnitude velocity fluctuations are most common, indicating a coherent vertical oscillation of the wake flow.

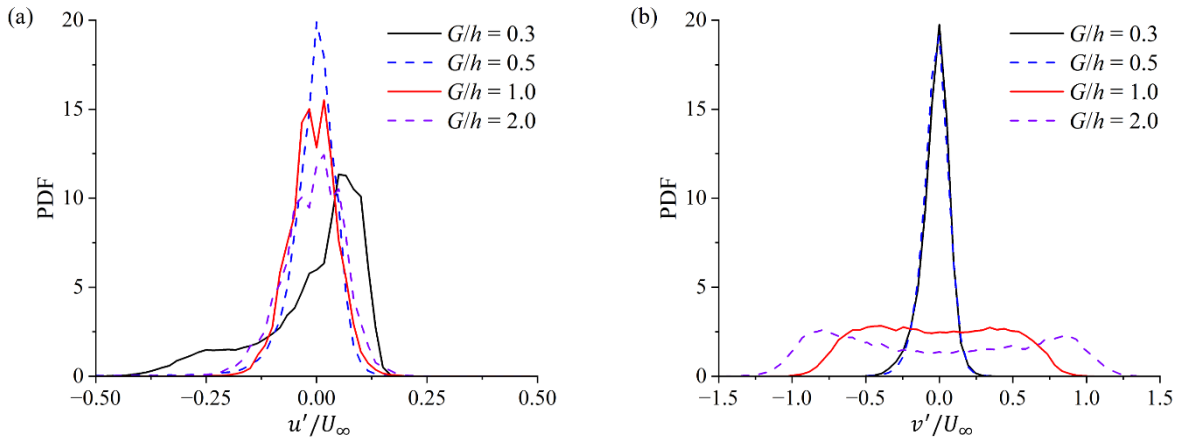

Figure 4.2.3: Probability density function of the streamwise velocity fluctuations at the gap outlet (a) and vertical velocity fluctuations at the point of the furthest streamwise extend of the mean recirculation region (b). PDFs are constructed using 60 *bins for each velocity sample.*

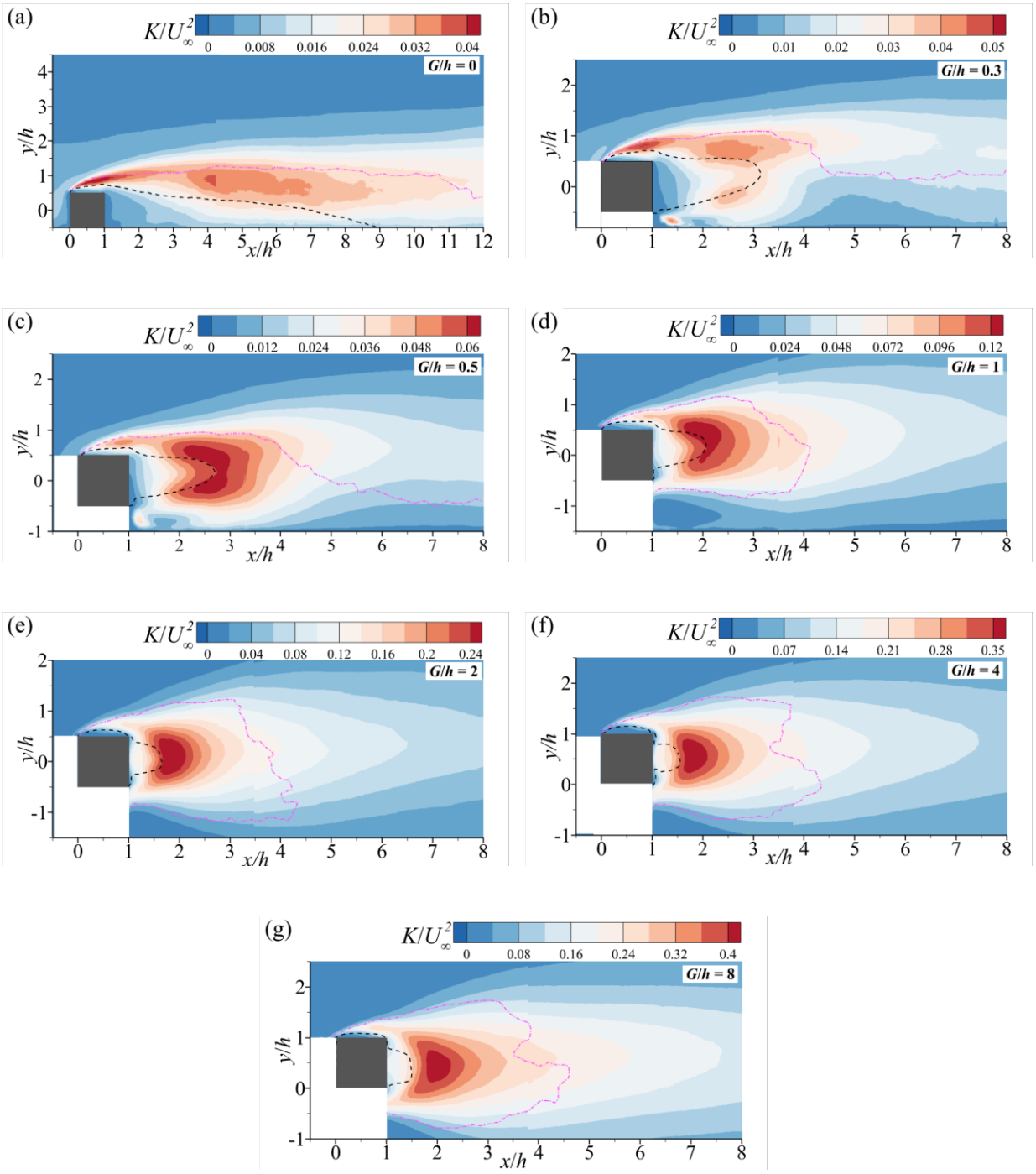

Figure 4.2.4: Contours of the in-plane component of turbulent kinetic energy (K) superimposed with isopleths of the 50% *forward flow fraction (green dashed isopleth) and the* 99% *forward flow fraction (violet dash-dotted isopleth).*

The turbulent kinetic energy (TKE), $K = \frac{1}{2}(\overline{u'u'} + \overline{v'v'})$, is estimated using planar PIV data and is shown in Figure 4.2.4 for the various test cases with the 50% and 99% forward flow fractions superimposed. The turbulent kinetic energy is strongest at the leading edge of the cylinder for the wall-mounted case, and decays in the streamwise direction. Noticeably for the $G/h = 0.3$ case, the concentration of TKE is located on either side of the mean recirculation region. This distribution is attributed to the dominance of $\overline{u'u'}$ in the near wall region, as shown in Chalmers et al. (2022) behind an offset cylinder with $G/h \leq 0.5$. However, as gap ratio increases, TKE becomes concentrated at the cylinder centerline at approximately the mean recirculation length, reflecting the dominance of $\overline{v'v'}$ in the wake region for the cases of $G/h > 0.5$. Indeed, as noted by Chalmers et al. (2022) and Durão et al. (1991), the wall tends to attenuate the vertical velocity fluctuations in comparison to the streamwise velocity fluctuations. Further comparisons with Panigrahi (2009) confirm that TKE is stronger in the upper shear layer when the cylinder is closer to the wall and becomes symmetrical in magnitude for $G/h > 0.57$. In the region above the cylinder, $0 \leq x/h \leq 1$, the maximum TKE occurs along the trajectory of the 99% forward flow fraction isopleth. These local peaks above the cylinder are strongest for cases with $G/h \leq 0.5$, above which the peak in the wake region is significantly stronger than that over the cylinder.

Figures 4.2.5, 4.2.6, and 4.2.7 show the vertical profiles of the TKE and Reynolds normal stress production terms, defined in equations 4.1-4.3, at $x/h = 0.25$, 1.4 and at the point of maximum K, respectively.

$$P_{uu} = -2\left(\overline{u'u'}\frac{\partial U}{\partial x} + \overline{u'v'}\frac{\partial U}{\partial y}\right) \tag{4.1}$$

$$P_{vv} = -2\left(\overline{v'v'}\frac{\partial V}{\partial y} + \overline{u'v'}\frac{\partial V}{\partial x}\right) \tag{4.2}$$

$$P_{tke} = -\frac{1}{2}(P_{uu} + P_{vv}) \tag{4.3}$$

The profiles in Figure 4.2.5 show that the production of TKE is overwhelmingly positive between $0.5 < y/h < 0.75$. In general, the positive production of TKE stems from positive contribution from the streamwise fluctuating velocity (P_{uu}), although the magnitude of local production is limited by the negative contributions from P_{vv}. The magnitude of production of TKE and Reynolds normal stresses increases as the gap size increases. Interestingly, concentration of K shown in Figure 4.2.4b at the gap outlet corresponds to negative production of TKE. This is because the strong mean velocity gradients, $\partial U/\partial x$ and $\partial U/\partial y$ resulting from the mean flow acceleration through the gap as well as the presence of the bottom wall, respectively, contribute to an overwhelmingly negative production of P_{uu} that is compensated for by a strong diffusion term. For cases with $G/h > 2.0$, the production of TKE is primarily positive on either side of the cylinder due to strong contributions from the streamwise component. However, behind the cylinder the contribution by the vertical velocity component is more significant than the negative contribution by the streamwise component resulting in a region of small magnitude positive production of TKE. At the horizontal location of maximum K, P_{uu} and P_{vv} provide significant contribution to the production of TKE for the wall-mounted and offset cases respectively. In fact, the relative dominance of P_{vv} compared with P_{uu} increases with increasing gap ratio.

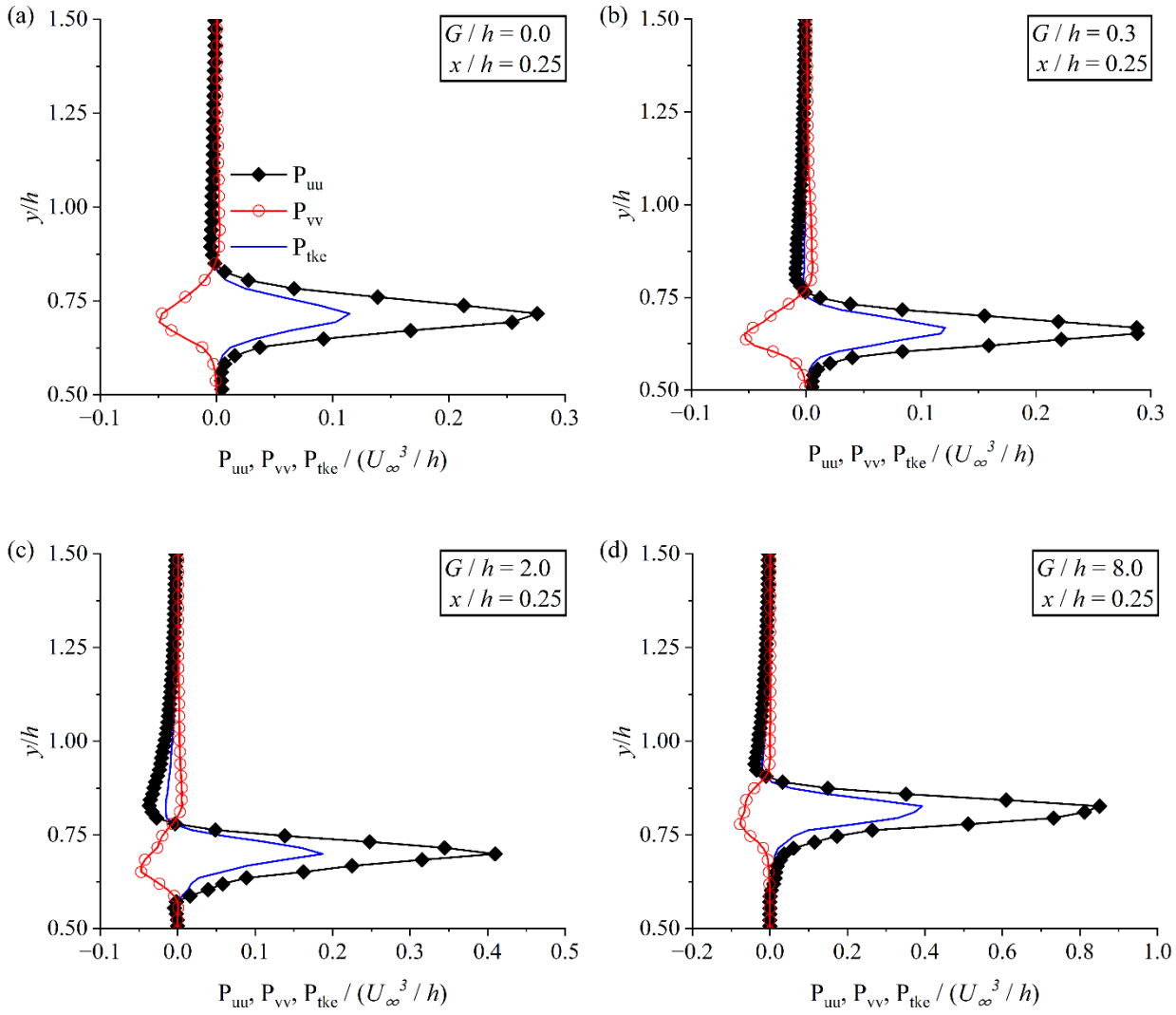

Figure 4.2.5: Vertical profiles of the production of TKE and Reynolds normal stresses immediately downstream of the cylinder's leading edge at $x/h = 0.25$.

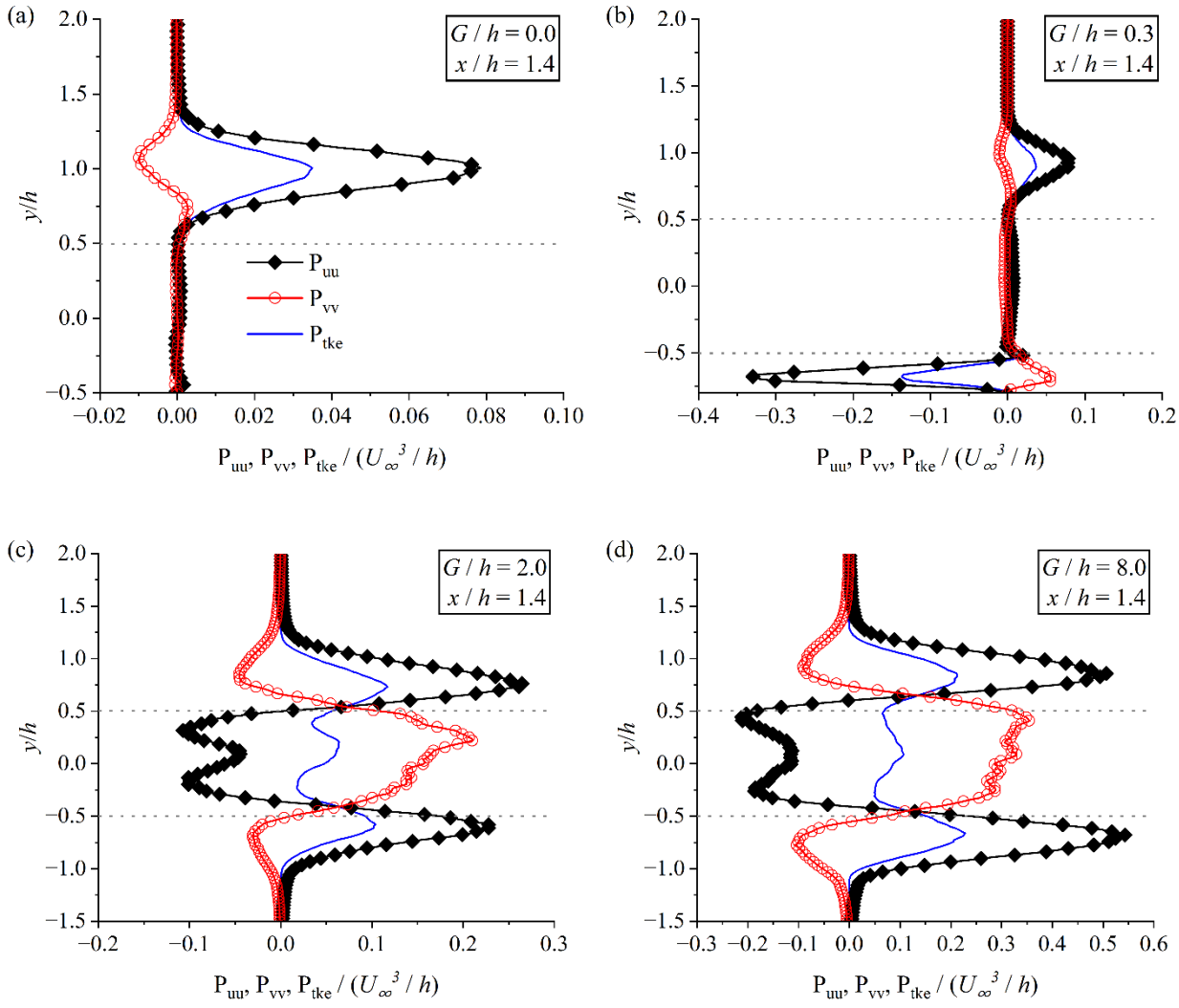

Figure 4.2.6: Vertical profiles of the production of TKE and Reynolds normal stresses downstream of the gap outlet at $x/h = 1.4$. *The grey dotted lines represent the vertical location of the upper and lower surfaces of the cylinder.*

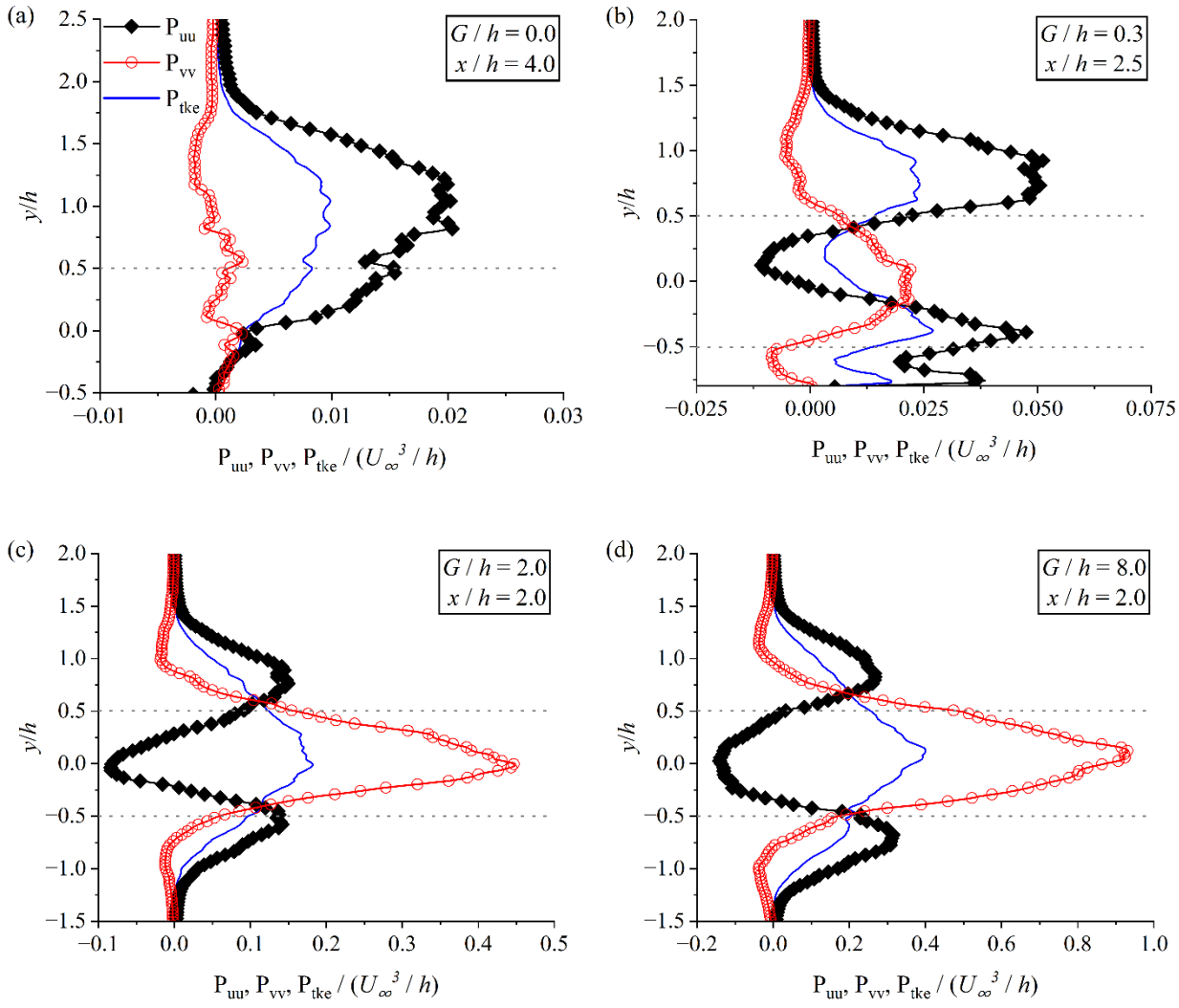

Figure 4.2.7: Vertical profiles of the production of TKE and Reynolds normal stresses at the horizontal location of maximum K in the wake region. The grey dotted lines represent the vertical location of the upper and lower surfaces of the cylinder.

The turbulent transport of the TKE by the u' and v' fluctuations, determined using the triple correlations $\overline{ku'} = \overline{u'u'u'} + \overline{u'v'v'}$ and $\overline{kv'} = \overline{u'u'v'} + \overline{v'v'v'}$, are shown in Figures 4.2.8 and 4.2.9, respectively, for selected gap ratios. For the wall-mounted case, there is a distinct change in sign of the turbulent transport above the cylinder along the 99% flow isopleth. Above the

separating isopleth, $\overline{ku'} < 0$ while $\overline{kv'} > 0$ indicating the presence of an ejection event. Conversely, below the 90% flow fraction, $\overline{ku'} > 0$ while $\overline{kv'} < 0$ indicating a sweep event. This is qualitatively similar to the results of Chalmers et al. (2021) who reported an ejection event above a wall-mounted cylinder and a sweep event within the recirculation region over a wall-mounted cylinder. For the $G/h = 0.3$ case, the transport of TKE is positive behind the cylinder near the recirculation length in both the streamwise and vertical directions. However, on either side of the recirculation region the streamwise transport is negligible while the vertical transport is negative indicating transport of the TKE towards the wall. For the $G/h = 2.0$ and 8.0 cases, the vertical component transports the TKE away from the recirculation region where it is then transported upstream by the streamwise fluctuations. This behaviour agrees with the findings of Addai (2022) who reported that high speed fluid bifurcates behind an offset square cylinder and is transported away from the horizontal centerline of the cylinder.

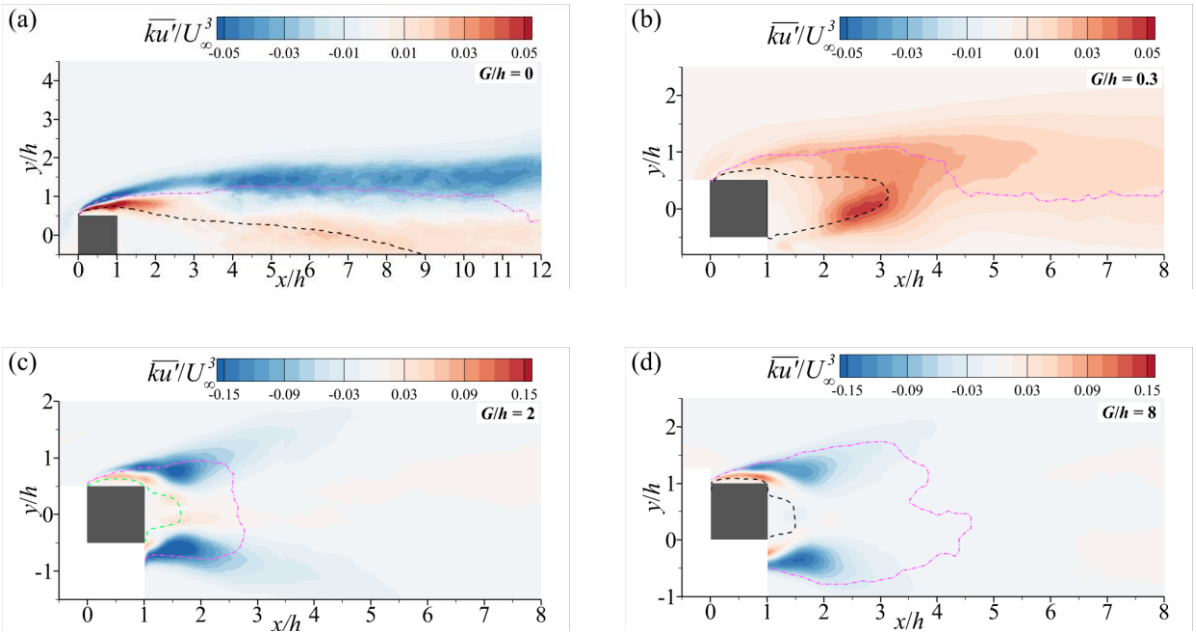

Figure 4.2.8: Characterization of the triple velocity correlations, $\overline{ku'} = \overline{u'u'u'} + \overline{u'v'v'}$*, for the* $G/h = 0.0, 03, 2.0,$ *and* 8.0 *cases*

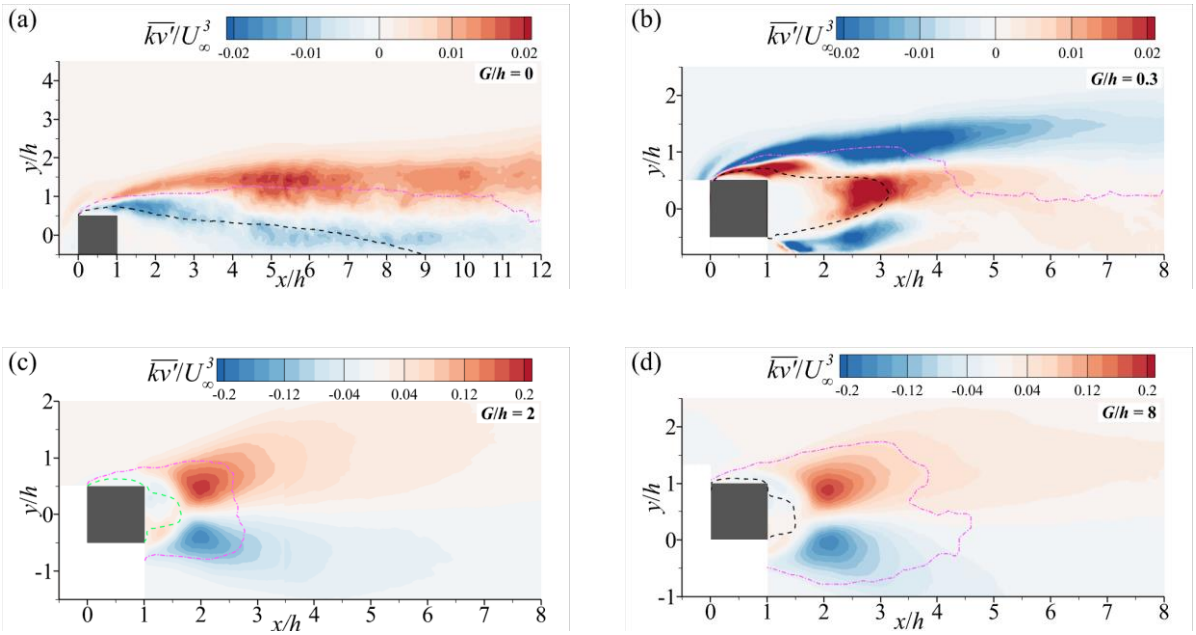

Figure 4.2.9: Characterization of the triple velocity correlations, $\overline{kv'} = \overline{u'u'v'} + \overline{v'v'v'}$*, for the* $G/h = 0.0, 0.3, 2.0,$ *and* 8.0 *cases*

4.3. Frequency Spectra

Figure 4.3.1 shows the frequency spectra of the streamwise velocity at $y/h = 0.75$ for $-2.0 < x/h < 1.0$. For the wall-mounted case, a sole peak frequency exists upstream of the bluff body near the frequency observed in the upstream TBL, at $St = 0.040$. At $x/h = 0.5$, the peak at $St = 0.040$ is still locally dominant, although the spectrum is excited at frequencies greater than $St = 0.100$ as well. At the trailing edge of the bluff body, the peak at $St = 0.040$ is subdominant compared to a broadband peak above $St = 0.100$. This broadband peak above $St = 0.100$ has also been observed in studies by Samani & Bergstrom (2015) and Addai (2022). For the $G/h = 0.5$ case, the peak at $St = 0.020$ is visible when $x/h < 0.5$. At $x/h = 0.5$, the energy concentrates around the vortex shedding frequency, $St = 0.109$. Low frequency oscillations at $St = 0.030$ for the $G/h = 2.0$ case are only visible when $x/h \leq -1.0$ and the vortex shedding

frequency dominates thereafter. This transition of energy towards the vortex shedding frequency occurs even earlier at $x/h < -2.0$ for the $G/h = 8.0$ case.

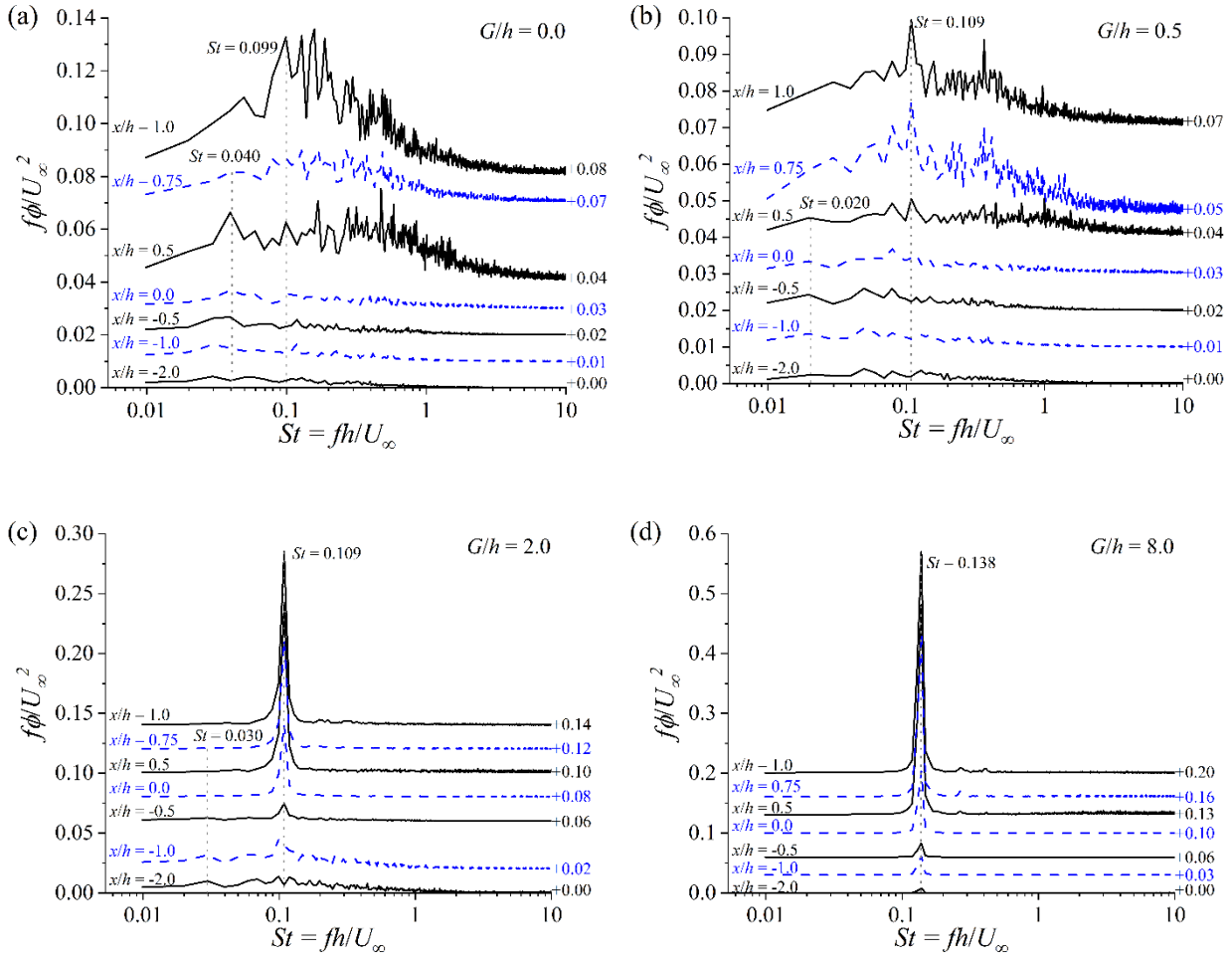

Figure 4.3.1: Premultiplied frequency spectra of the streamwise velocity fluctuations at $y/h = 0.75$ *and* $-2.0 \leq x/h \leq 1.0$ *for* $G/h =$ *(a)* 0.0, *(b)* 0.5, *(c)* 2.0, *and (d)* 8.0. *The frequency spectra at different locations are offset for clarity by the amount denoted to the right of the spectra.*

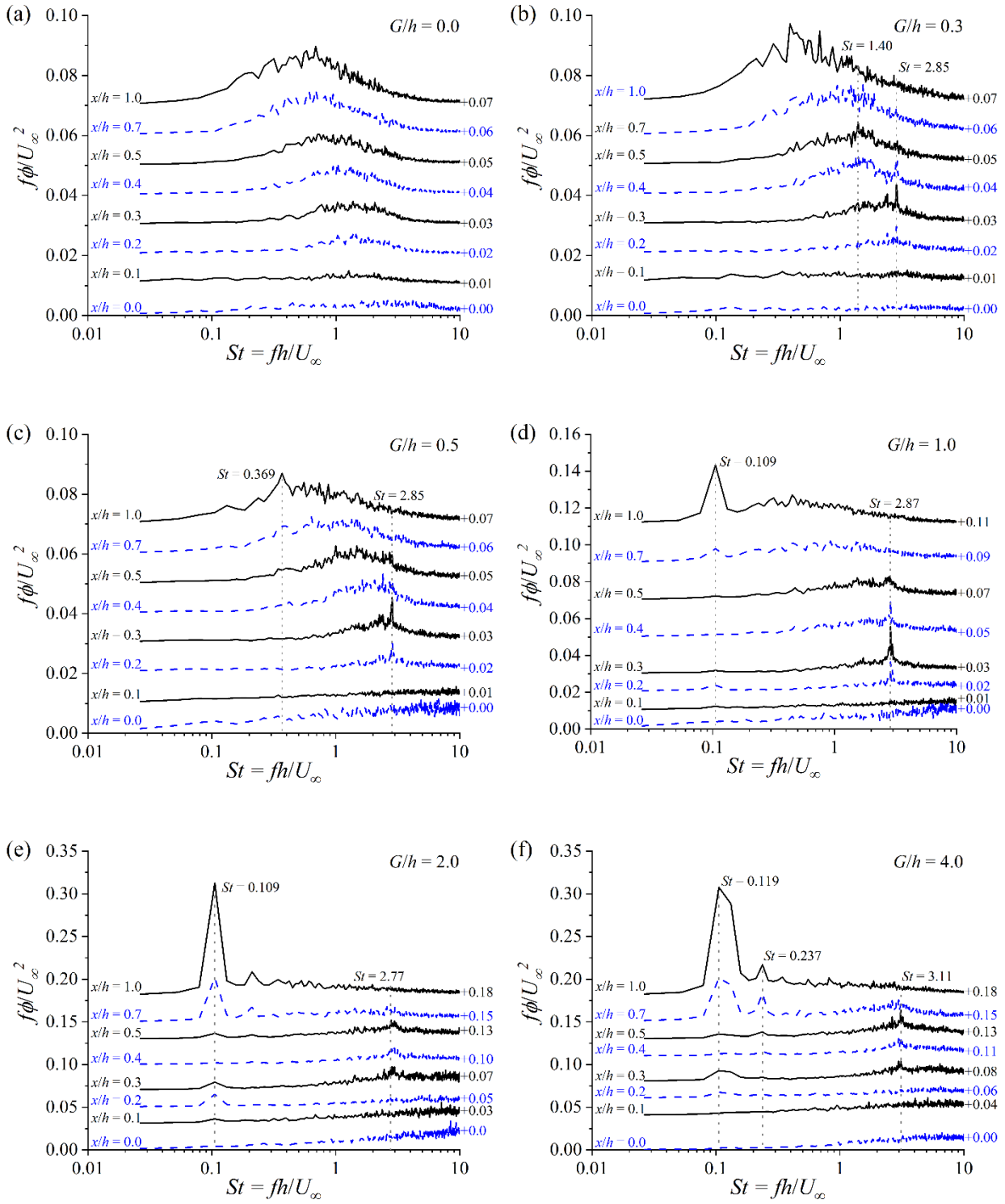
(a)
G/h = 0.0
(b)
G/h = 0.3
St = 1.40
St = 2.85
(c)
G/h = 0.5
St = 0.369
St = 2.85
(d)
G/h = 1.0
St = 0.109
St = 2.87
(e)
G/h = 2.0
St = 0.109
St = 2.77
(f)
G/h = 4.0
St = 0.119
St = 0.237
St = 3.11
x/h = 1.0
x/h = 0.7
x/h = 0.5
x/h = 0.4
x/h = 0.3
x/h = 0.2
x/h = 0.1
x/h = 0.0
fϕ/U∞²
St = fh/U∞

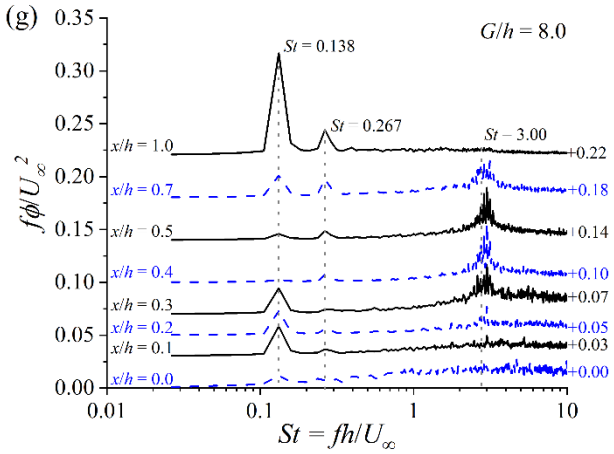

Figure 4.3.2: Premultiplied frequency spectra of the vertical velocity fluctuations along the shear layer above the cylinder between $0.0 \leq x/h \leq 1.0$ *for various test cases. The frequency spectra at different locations are offset for clarity by the amount denoted to the right of the spectra.*

Following the approach of Moore et al. (2019) and Fang et al. (2022), the mean trajectory of the shear layer is defined as the vertical locations of maximum TKE. To further investigate the transition to turbulence and the occurrence of KH vortices, Figure 4.3.2 shows the frequency spectra of the vertical velocity fluctuations along the trajectory of the mean shear layer over the cylinder. For the wall-mounted case in Figure 4.3.2a, a broadband peak occurs between $1.00 \leq St \leq 3.00$ at $x/h = 0.2$, indicating the presence of KH instabilities near the leading edge of cylinder. As the reference point moves downstream, the broadband peak migrates to lower frequencies. For the case of $G/h = 0.3$, a distinct spectral peak occurs at $St = 2.85$ between $x/h = 0.2$ and 0.4. For $0.4 \leq x/h \leq 0.8$, a broad peak is observed near the subharmonic frequency $St = 1.40$. This represents the traditional understanding that KH vortices are shed near the cylinder's leading edge before merging in the spanwise direction and migrating towards a lower frequency (Moore et al. 2019). A similar pattern of spectral peaks migrating towards lower

frequencies in the streamwise direction is also observed for the $G/h = 0.5$ case, however spectral migration is not observed above $G/h \geq 1$. The KH frequency, $St = 3.00$, for the $G/h = 8.0$ case is in good agreement with the value of $St = 3$ reported by Kiya & Sasaki (1983) for flow past a plate as well as with the findings of Addai (2022) who reported $St = 2.92$ for a square cylinder with gap ratio ranging from $0.3 \leq G/h \leq 4.0$. An additional low frequency peak is observed for test cases with $G/h \geq 1.0$ in the range of the von Kármán (VK) vortex shedding frequency, $0.10 < St < 0.14$ (Bosch et al. 1996; Bailey et al. 2002; Moore et al. 2019; Chalmers et al. 2022). As the gap ratio increases, the harmonics of the shedding frequency become increasing energetic indicating the strengthening of VK vortex shedding motions as the cylinder moves away from the wall and towards lower incoming turbulence levels. Unlike the KH instability that is confined to $0.2 < x/h < 0.8$, the imprint of the VK vortex shedding motions is discernible as early as $x/h = 0.0$ for the $G/h = 8.0$ case and as early as $x/h = 0.2$ for the $G/h = 1.0$, 2.0, and 4.0 cases.

4.4. Spectral Proper Orthogonal Decomposition

A spectral proper orthogonal decomposition (SPOD) analysis is performed following the procedure outlined in Towne et al. (2018), to extract spatial structures that vary over a designated time period. This involves performing a Fourier transform on the velocity field using Welch's overlapping window technique (Welch 1967). The size of the Fourier transformations was 6 000 snapshots ($7.43s$) and the window overlap was 100 snapshots ($0.12s$) resulting in resolved frequencies occurring in multiples of $0.12U_\infty/h$ (0.2018 Hz). The Fourier-transformed velocity field can then be further decomposed using a single value decomposition that is commonly used for spatial POD (Fang & Tachie 2019, Chalmers et al. 2022). The resultant, decomposed velocity field takes the form of equation 4.4.

$$u'(x,t) = \sum_{j=1}^{\infty}\sum_{k=1}^{200} a_j^{(k)}\Phi_j^{(k)}(x)e^{i2\pi f_j t} + c.c. \tag{4.4}$$

where $\Phi_j^{(k)}$ denotes the k-th mode at the j-th frequency respectively, $a_j^{(k)}$ is the corresponding mode coefficient, and $c.c$ denotes the complex conjugate. Further details concerning the algorithm used in the present study can be found in Fang et al. (2022).

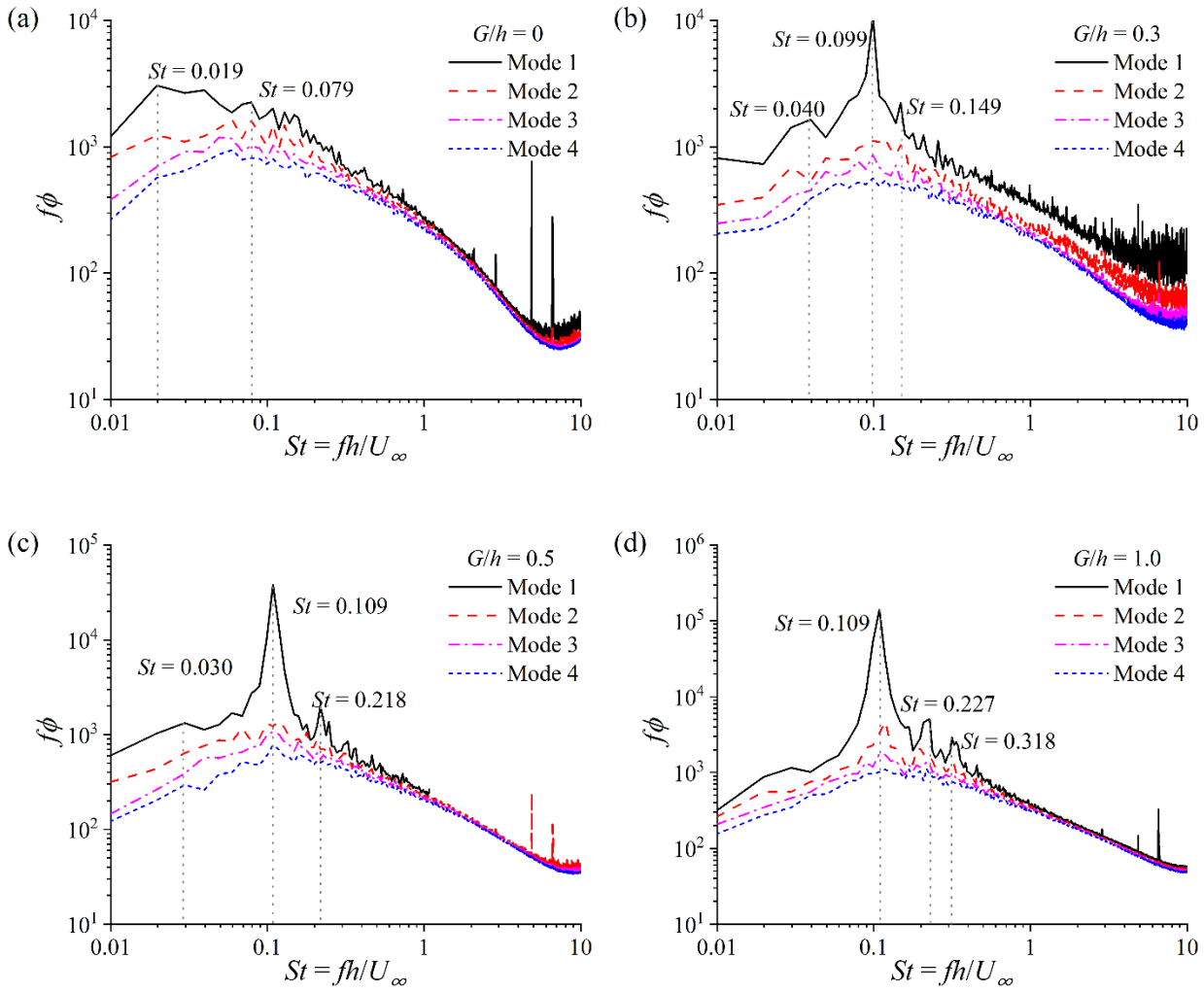

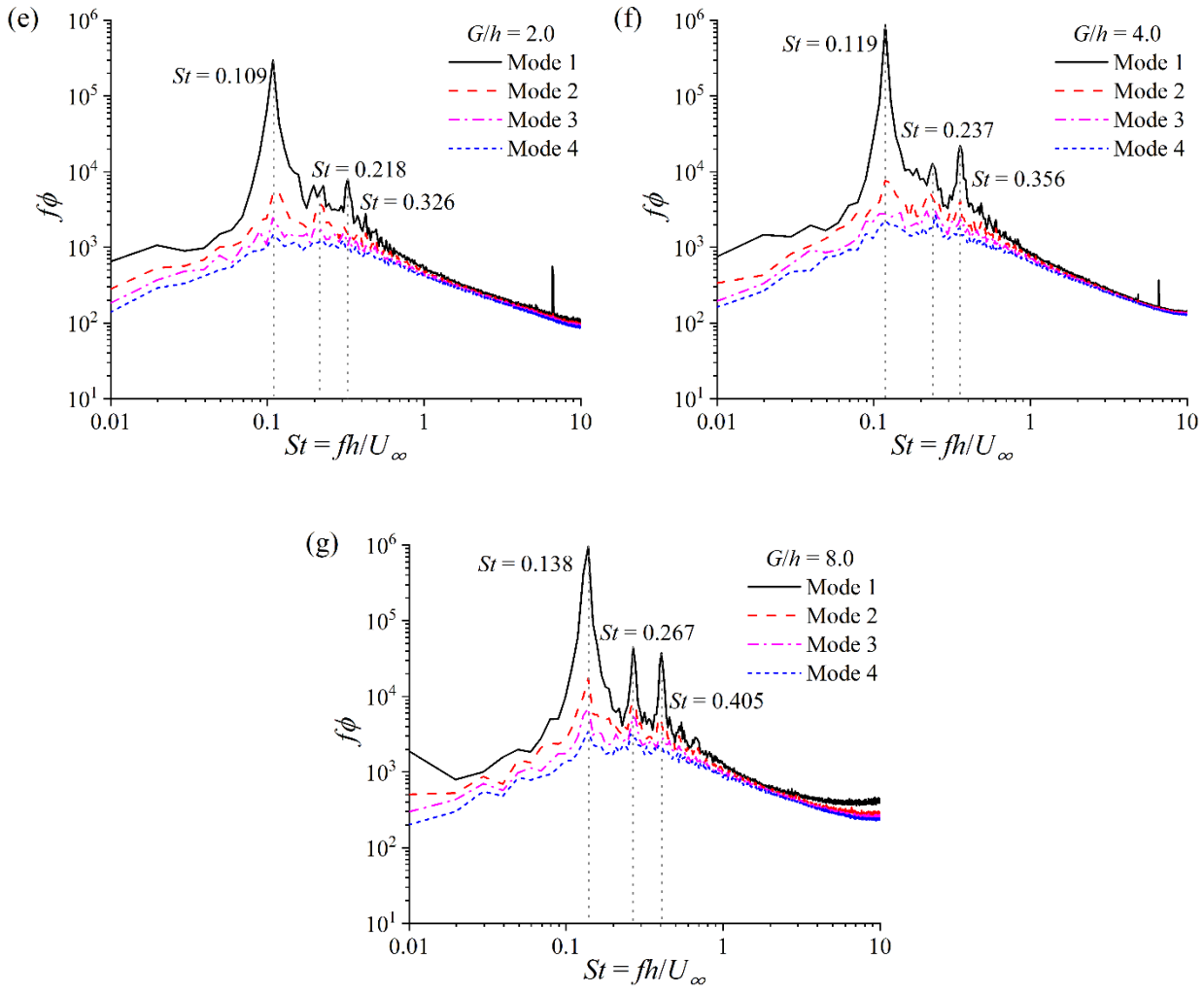

Figure 4.4.1: Premultiplied frequency spectra of the first four SPOD mode for the various test cases.

Spectral POD was performed over the entire field of view of both cameras to further understand the various coherent structures and the dynamic relationship amongst them. Previous work by Riches et al. (2018) notes the pairing of space-only POD modes due to vortex shedding patterns in the bluff body wake, and by Chalmers et al. (2022) who describe the relevance of the first two space-only POD mode pairs for square cylinders near a rough wall. Accordingly, Figure 4.4.1

shows the premultiplied frequency spectra of the first four SPOD mode energies. In general, coherent structures emanating from the upstream turbulent boundary layer manifest at frequencies between $0.03 < St < 0.08$ (Chalmers et al. 2022, Fang et al. 2019). Figures 4.4.1a, 4.4.1b, and 4.4.1c show coherent structures emanating from the upstream TBL, at $St < 0.08$, are influential in the first POD modes at $G/h \leq 0.5$. Vortex shedding dominates the first four POD modes for all offset cases between a frequency $0.099 \leq St \leq 0.139$, depending on the gap ratio. Additional spectral peaks are observed at the harmonics of the vortex shedding frequency for cases with $G/h \geq 0.5$. For example, at $G/h = 0.5$ there are peaks at $St = 0.109$ and 0.218, while at $G/h = 8$ there are peaks at $St = \{0.139, 0.267, 0.405\}$. Although the wall-mounted case does not display a dominant vortex shedding frequency, there are peaks at $St = 0.019$ and 0.079 which, respectively, matches the frequency of the incoming TBL reported in Figure 4.1.1 and the flapping shear layer as reported by Fang et al. (2019). The energy content of the first SPOD modes are significantly higher than those of higher rank modes at $St < 0.4$. This emphasizes the coherency of the turbulent structures at these low frequencies and the subsequent analysis will focus accordingly on the information extracted from the first SPOD mode.

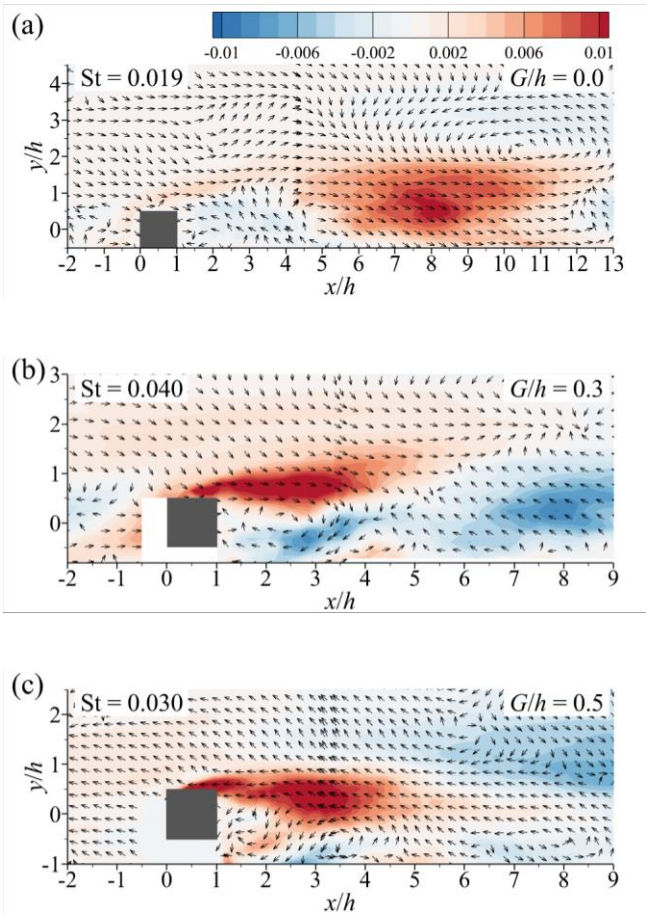

Figure 4.4.2: The first SPOD mode at (a) $St = 0.019$ *for the* $G/h = 0.0$ *case, (b)* $St = 0.040$ *for the* $G/h = 0.3$ *case, and (c)* $St = 0.03$ *for the* $G/h = 0.5$ *case at arbitrary phase angles. The vectors of the SPOD mode velocities are superimposed. An animated portrayal of the mode topologies is also provided.*

Figure 4.4.2 shows the first POD mode at an arbitrary phase angle, $\alpha = 2\pi f_j t$, for significant frequencies below $St = 0.05$ based on the frequency spectra shown in Figure 4.4.1. Animations are also provided to depict a complete period of SPOD modes with the phase angle ranging from $0 - 2\pi$. For the wall-mounted case, alternating signed structures originate at the sharp corner of the cylinder and propagate into the wake region. The structure becomes strongest near the

reattachment point near $x/h = 8.0$, at which point a new structure originates near the leading edge as the original structure dissipates downstream. This is reminiscent of the observations made by Mercier et al. (2020) that smaller high frequency KH vortices amalgamate with large flapping separation bubbles in the wake of a cylinder, around $x/h = 7$. For the $G/h = 0.3$ case, oppositely signed vortices emanate from both the upper and lower surfaces of the square cylinder. The structures emanating from the upper surface propagate along the shear layer and dissipate in the downstream direction. In contrast, the propagation of structures originating from the bottom surface of the cylinder are confined by the wall. Thus, as reported by Chalmers et al. (2022), an in-phase interaction between the upper and lower shear layers is prohibited which decreases the likelihood of regular VK vortex shedding motions. As the gap ratio increases to $G/h = 0.5$, wall confinement effects are noticeably less restrictive. Structures emanating from the lower surface of the cylinder are able to interact with the upper shear layer before dissipating in the downstream direction.

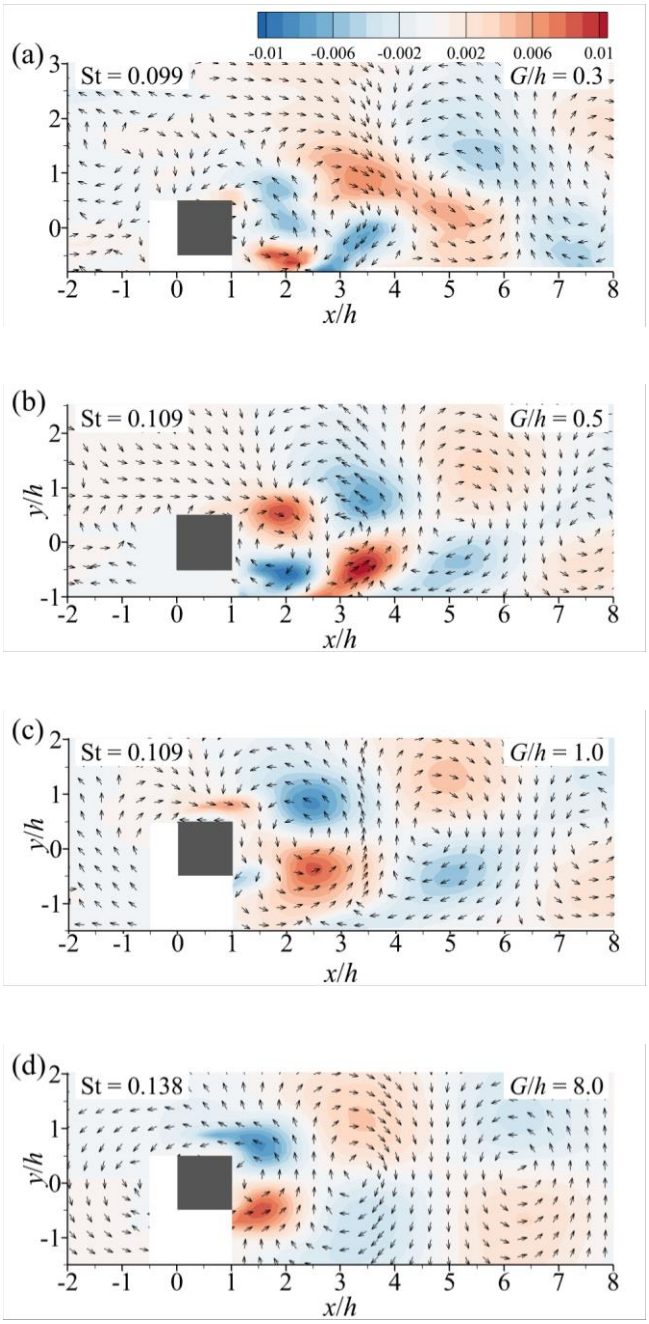

Figure 4.4.3: The first POD mode at (a) $St = 0.099$ *for the* $G/h = 0.3$ *case, (b)* $St = 0.109$ *for the* $G/h = 0.5$ *case, (c)* $St = 0.109$ *for the* $G/h = 1.0$ *case, and (d)* $St = 0.138$ *for the* $G/h = 8.0$ *case at arbitrary phase angles. The vectors of the SPOD mode velocities are superimposed. An animated portrayal of the mode topologies is also provided.*

Figure 4.4.3 shows the first POD mode at an arbitrary phase angle for the vortex shedding frequencies identified in Figure 4.4.1. At the vortex shedding frequency for the $G/h = 0.3$ case, regions of strong velocity fluctuations originate near the wall at approximately $x/h = 2.0$. This region of high velocity fluctuations convects downstream and as this occurs, the structure splits in two different directions. One of these structures continues travelling in the downstream direction and becomes inclined away from the wall, while the other structure is entrained into the upper shear layer and merges with smaller structures originating along the upper surface of the cylinder. For the $G/h = 0.5$ case, the entrainment into the upper shear layer becomes much less distinct in favour of regular vortex shedding motions that occur at a higher frequency. In the case of $G/h = 1.0$, the structures are symmetric in the near wake although a slight skew upwards is visible in the lower shear layer at approximately $x/h = 4.0$, indicating the influence of the wall. This asymmetry diminishes as the gap size increases until it disappears entirely for the $G/h = 8.0$ case, and the vortex shedding frequency increases further to $St = 0.138$ as a result of the coherent VK vortex shedding motions.

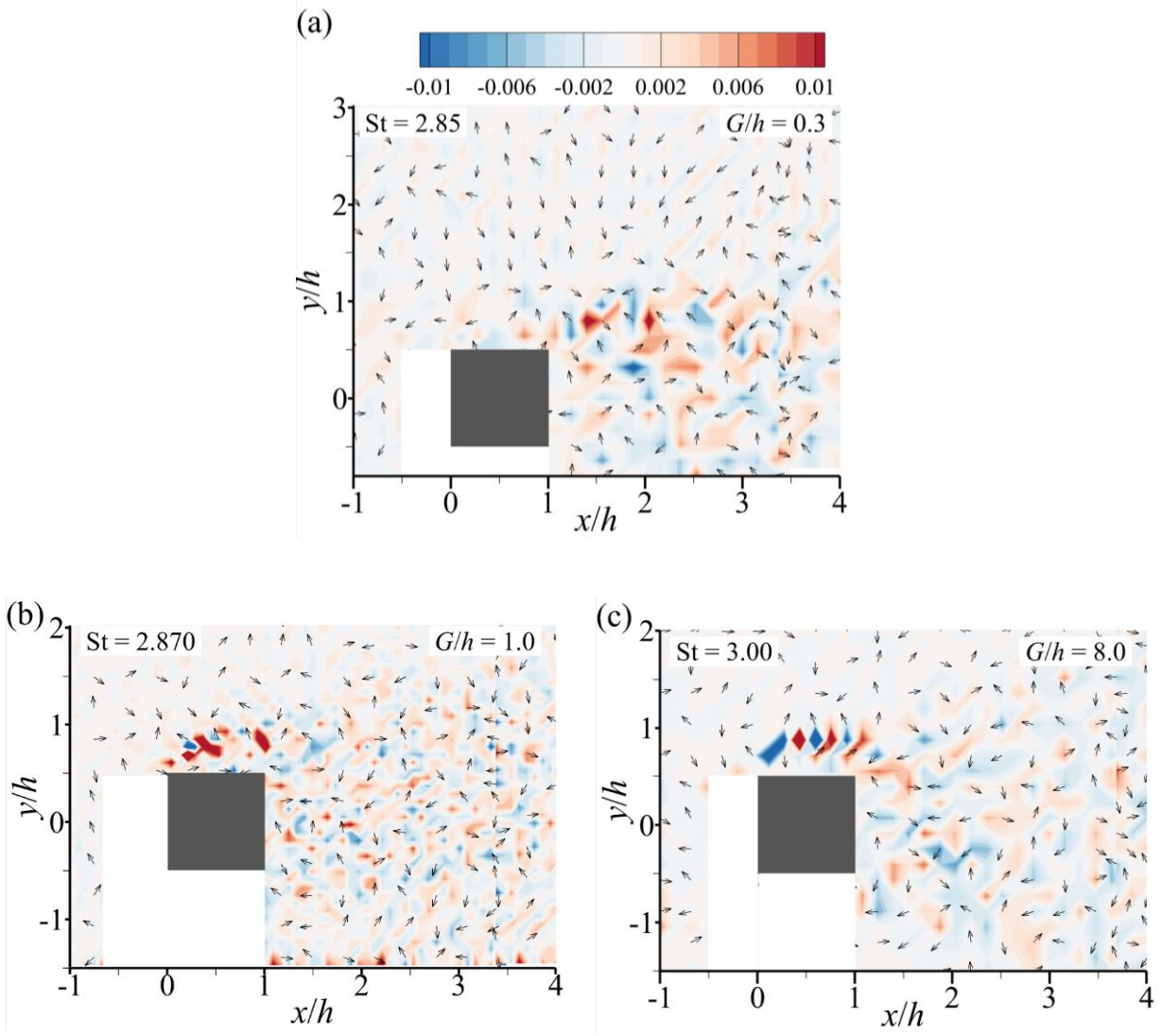

Figure 4.4.4: The first POD mode at (a) $St = 2.850$ for the $G/h = 0.3$ case, (b) $St = 2.870$ for the $G/h = 1.0$ case, and (c) $St = 3.000$ for the $G/h = 8.0$ case at arbitrary phase angles. The vectors of the SPOD mode velocities are superimposed. An animated portrayal of the mode topologies is also provided.

Figure 4.4.4 shows the first POD mode at an arbitrary phase angle for the KH frequencies identified in Figure 4.3.2. A train of alternating positive and negative vortices are shed from the cylinder's

leading edge for each test case shown. For the $G/h = 0.3$ case, the train of vortices periodically disappears in favour of an amalgamation of vortices around $x/h = 0.6$. This is in line with the observations from Figure 4.2.3 and the general understanding that vortices pair in the spanwise direction at the KH frequency subharmonic. As the gap ratio increases to $G/h = 1.0$, the frequency of shed vortices increases to $St = 2.87$ resulting in a more organized train of vortices. Additionally, the trajectory of the shed vortices extends further away from the cylinder's surface for the larger gap ratio. This follows the observation from Lander et al. (2016) that the trajectory of the KH vortices approaches the cylinder surface as the freestream turbulence intensity increases. In this case, the local turbulence intensity is higher at smaller gap ratios due to the presence of the rough wall. The coordination of vortices extending away from the cylinder's surface is further exaggerated for the $G/h = 8.0$ case. Furthermore, the animation of the $G/h = 8.0$ case reveals a cyclic pattern of KH formation and dissipation. First, the shed vortices merge between $x/h = 0.4 - 0.8$, before collapsing closer to the cylinder surface while weakening in intensity. This merging of vortices occurs further downstream than is reported by Moore et al. (2018). Afterwards, the vortices reorganize into a coherent train of alternating positively and negatively signed vortices emanating from the leading edge of the cylinder.

5.0 Summary, Conclusions and Future Work

5.1 Summary and Conclusions

Two separate studies, each using time-resolved particle image velocimetry, were performed to investigate the flow dynamics surrounding a square cylinder in the vicinity of a wall. In the first study, both wall-mounted and offset cylinders are examined, and the wall-normal distances of the offset cylinders are 0.3, 0.5 and 2.0 times cylinder height. The Reynolds number (Re_h) based on the freestream velocity and cylinder height is kept at 12 750.

For the wall-mounted cases, the mean flow features a separated shear layer emanating from the leading edge of cylinder encompassing a large mean recirculation behind the cylinder. The present and available data in the literature demonstrate that the mean reattachment length increases exponentially with Reynolds number but becomes independent of Reynolds number at $Re_h = 20\ 000$. The mean reattachment length for the smooth case decreases linearly with increasing relative boundary layer thickness. It was observed that upstream rough wall reduced the reattachment length by 29% compared to the smooth case. Regions of elevated Reynolds stresses are observed in the upper and lower shear layers in the wake region. Wall roughness tends to reduce the level of Reynolds stresses in the lower shear layer at smaller gap ratios (by 37% and 26% for the cases of $G/h = 0.3$ and 0.5, respectively), but its effects on the mean flow and Reynolds stresses become negligible when the gap is two times of the cylinder height.

The dominant shedding frequencies in the wake region of offset cylinders are within $St_\infty \in [0.119, 0.130]$ in the smooth case, and $St_\infty \in [0.099, 0.109]$ in the rough case. In spite of the thick boundary layer, the freestream velocity is the appropriate velocity scale for the vortex shedding frequencies for the offset cylinders. The proper orthogonal decomposition analysis

reveals that the dominant structure behind wall-mounted cylinders is related to the incoming coherent structures embedded in the turbulent boundary layer, as such its characteristic frequency is similar to the incoming fluctuating velocity regardless of upstream wall roughness condition. With an upstream smooth wall, the characteristic frequencies of POD modes are not influenced by the incoming TBL. On the other hand, the characteristic frequencies of the incoming rough-wall TBL manifest at higher (third and/or fourth) ranks of POD modes at relatively small gap ratios (G/h = 0.3 and 0.5).

The pairing mechanism of POD modes is closely related to the occurrence of vortex shedding motion behind cylinders, and the regular vortex shedding motion relies on the mutual interaction of fluctuating vorticity originated in the upper and lower shear layers. Both smaller gap ratio and wall roughness promote intermittent vortex shedding motion. In the case of the smallest gap ratio (G/h = 0.3), vortex shedding motion is highly intermittent with an upstream smooth wall, and becomes indiscernible with an upstream rough wall. In the latter rough-wall case, the dominant vortical structures in the upper and lower shear layers possess drastically different length scales, and evolve differently with time. Consequently, an in-phase interaction between the upper and lower shear layers as well as regular vortex shedding motion are absent.

The second study presents a focused investigation on gap ratio effects on the flow surrounding square cylinder in a rough wall boundary layer. The cylinder is offset from the wall at different distances resulting in gap sizes of 0.0, 0.3, 0.5, 1.0, 2.0, 4.0 and 8.0 times the cylinder height. The Reynolds number based on the freestream velocity and cylinder height remained constant at 12 750 for each test case and the relative boundary layer thickness was equal to 7.2 cylinder heights. Data is analyzed in terms of mean flow, production and turbulent transport of turbulent kinetic energy, and frequency spectra at different locations upstream of the cylinder's trailing edge.

Spectral proper orthogonal decomposition analysis is also performed to investigate the coherent structures oscillating at various frequencies.

The mean flow reveals a region of flow reversal above as well as in the wake of the cylinder. The mean and the permanent recirculation lengths, defined by the isopleths of the 50% and 99% forward flow fractions respectively, remain constant for cases with gap ratios greater than 1.0 times the cylinder height. Comparison with the literature reveals that these recirculation lengths are dependent on the upstream flow conditions such as the incoming turbulent boundary layer thickness and Reynolds number. When the gap size is 2.0 times the cylinder height, the magnitude of the reverse flow drops significantly and the flow acceleration through the gap is the strongest. Furthermore, the distribution of turbulent kinetic energy becomes symmetrical when the gap size is equal to 2.0 times the cylinder height. This indicates that below this critical gap size, the vertical velocity fluctuations are suppressed by the presence of the wall. Vertical profiles of the turbulent kinetic energy production show that when the gap size is 0.3 times the cylinder height there is significant negative production of turbulent kinetic energy at the outlet of the cylinder undergap. Behind the cylinder, the vertical velocity fluctuations are the major contributor to the production of TKE.

Spectral analysis based on the velocity fluctuations along the shear layer revealed the presence of the Kelvin-Helmholtz instability oscillating at a Strouhal number based on the freestream velocity and cylinder height of $2.77-3.11$. The onset of the Kelvin-Helmholtz instability is between $0.2-0.4$ cylinder heights from the leading edge of the cylinder for all test cases. Furthermore, the presence of spectral migration, indicating the spanwise pairing of vortices, occurs for cases with gap size less than or equal to 0.5 times the cylinder height. The von Kármán frequency is also observed globally for cases with gap size greater than or equal to 1.0 cylinder height. Spectral

analysis upstream and over the cylinder revealed the transition of energy from the frequency detected in the upstream turbulent boundary layer towards the shedding frequency as the reference point moves in the streamwise direction. The frequency observed in the turbulent boundary layer is observed along the shear layer at 0.5 cylinder heights downstream of the leading edge.

Spectral proper orthogonal decomposition analysis revealed that the most energetic frequencies are located between a Strouhal number of $0.099 - 0.138$ depending on the gap ratio, indicating the dominance of the vortex shedding motions in the wake region. Other energetic frequencies were observed below a Strouhal number of 0.05 for cases with a gap size less than 1.0 cylinder height. For the wall-mounted case, the low frequency structures show strong velocity fluctuations along the shear layer. These large structure merges with the small-scale vortices near the point of reattachment onto the bottom wall around 8.0 cylinder heights from the leading edge of the cylinder. At the vortex shedding frequencies, there is significant break-up of vortices near the wall surface that prevents regular vortex shedding for cases with gap size less than 0.5 cylinder heights. Spectral proper orthogonal decomposition contours at high frequencies reveal the pairing of vortices around 0.6 cylinder heights past the leading edge for each test case. Furthermore, the trajectory of the Kelvin Helmholtz vortices extends further away from the cylinder for cases with larger gap sizes.

5.2 Future Work

Based on the findings of the present studies, the following recommendations are provided for further investigation into this topic.

1. Due to experimental limitations in the present study, the flow underneath the cylinder was not captured and therefore not discussed. The gap flow underneath a cylinder can differ

from the flow above the cylinder due to the confinement of the wall boundary. It is recommended that future studies investigate gap ratio effects on the gap flow underneath a square cylinder.

2. For an offset cylinder, the smallest gap ratio tested was equal to 0.3 cylinder height. Although the clear, organized vortex shedding motions are not present for this case in the present study, there are still intermittent signs of irregular vortex shedding in the wake of the cylinder. It is recommended in further studies that a range of smaller gap ratios are tested between 0.0 and 0.3 cylinder height.
3. Analysis of the turbulent kinetic energy budget was limited in the present study due to the two-component nature of the time-resolved particle image velocimetry system that was used. In future studies, it is recommended to explore the use of direct numerical simulation or tomographic particle image velocimetry to capture, and analyze, the three-dimensional flow field surrounding a square cylinder near a rough wall.
4. Varying the Reynolds number is shown to drastically affect the flow behaviour around a wall-mounted square cylinder. Future work should focus on the combined effects of Reynolds number and wall-roughness on the flow past offset square cylinders.

References

Addai, S. (2022). Experimental study of wall proximity effects on turbulent flow around a square cylinder. *Master's Thesis, University of Manitoba*.

Adrian, R.J., Meinhart, C.D., & Tomkins, C.D. (2000). Vortex organization in the outer region of the turbulent boundary layer. *Journal of Fluid Mechanics,* 422, 1-54.

Agelinchaab, M., & Tachie, M. F. (2008). PIV study of separated and reattached open channel flow over surface mounted blocks. *Journal of Fluids Engineering*, 130, 061206.

Akinlade, O. G., Bergstrom, D. J., Tachie, M. F., & Castillo, L. (2004). Outer flow scaling of smooth and rough wall turbulent boundary layers. *Experiments in Fluids*, 37, 604-612.

Baars, W. J., Squire, D. T., Talluru, K. M., Abbassi, M. R., Hutchins, N., & Marusic, I. (2016). Wall-drag measurements of smooth- and rough-wall turbulent boundary layers using a floating element. *Experiments in Fluids*, 37, 604-612.

Bai, H., & Alam, M.M. (2018). Dependence of square cylinder wake on Reynolds number. *Physics of Fluids*, 30, 015102.

Bailey, S.C.C., Kopp, G.A., & Martinuzzi, R.J. (2002) Vortex shedding from a square cylinder near a wall. *Journal of Turbulence,* 3 (3), 1-18.

Bergeles, G., & Athanassiadis, N. (1983). The flow past a surface-mounted obstacle. *Journal of Fluids Engineering*, 105, 461-463.

Bosch, G., Kappler, M., & Rodi, W. (1996). Experiments on the flow past a square cylinder placed near a wall. *Experimental Thermal and Fluid Science*, 13, 292-305.

Brun, C., Aubrun, S., Goossens, T., Ravier, P. (2008). Coherent structures and their frequency signature in the separated shear layer on the sides of a square cylinder. *Flow Turbulence Combust*, 81, 97-114.

Castro, I.P. (1979). Relaxing Wakes Behind Surface-Mounted Obstacles in Rough Wall Boundary Layers. *Journal of Fluid Mechanics*, 93, 631-659.

Chalmers, H., Fang, X., & Tachie, M. F. (2021). Streamwise aspect ratio effects on turbulent flow separations induced by forward-backward-facing steps. *Journal of Fluids Engineering*, 143, 021305.

Chalmers, H., Fang, X., Addai, S., Tachie, M.F. (2022). The effects of wall roughness on the flow dynamics behind a near-wall square cylinder. *Experiments in Fluids*, 63, 123.

Chauhan, K.A., Monkewitz, P.A., & Nagib, H.M. (2009). Criteria for assessing experiments in zero pressure gradient boundary layers. *Fluid Dynamics Research*, 41, 021404.

Durão, D. F. G., Heitor, M. V., & Pereira, J. C. F. (1988). Measurements of turbulent and periodic flows around a square cross-section cylinder. *Experiments in Fluids*, 6, 298-304.

Durão, D.F.G., Gouveia, P.S.T., & Pereira, J.C.F. (1991). Velocity characteristics of the flow around a square cross section cylinder placed near a channel wall. *Experiments in Fluids*, 11, 341-350.

Essel, E. E., & Tachie, M. F. (2017). Upstream roughness and Reynolds number effects on turbulent flow structure over forward facing step. *International Journal of Heat and Fluid Flow*, 66, 226-242.

Essel, E. E., Nematollahi, A., Thacher, E.W., & Tachie, M. F. (2015). Effects of upstream roughness and Reynolds number on separated and reattached turbulent flow. *Journal of Turbulence*, 16, 872-899.

Fang, X., Tachie, M.F., & Dow, K. (2022). Turbulent separations beneath semi-submerged bluff bodies with smooth and rough undersurfaces. *Journal of Fluid Mechanics*, 947, A19 1-34.

Fang, X., & Tachie, M. F. (2019a). Flows over surface-mounted bluff bodies with different spanwise widths submerged in a deep turbulent boundary layer. *Journal of Fluid Mechanics*, 877, 717-758.

Fang, X., & Tachie, M.F. (2019b). On the unsteady characteristics of turbulent separations over a forward-backward-facing step. *Journal of Fluid Mechanics*, 863, 994-1030.

Fang, X., & Tachie, M. F. (2020). Spatio-temporal dynamics of flow separation induced by a forward-facing step submerged in a thick turbulent boundary layer. *Journal of Fluid Mechanics*, 892, A40.

Farell, C., Carrasquel, S., Güven, O., & Patel, V. C. (1977). Effect of wind-tunnel walls on the flow past circular cylinder and cooling tower models. *Journal of Fluids Engineering*, 99 (3), 470-479.

Flack, K. A., & Schultz, M. (2014). Roughness effects on wall-bounded turbulent flows. *Physics of Fluids*, 26, 101305.

Hearst, R.J., Gomit, G., & Ganapathisubramani, B. (2016). Effect of turbulence on the wake of a wall-mounted cube. *Journal of Fluid Mechanics*, 804, 513-530.

Ikhennicheu, M., Germain, G., Druault, P., Gaurier, B. (2019). Experimental study of coherent flow structures past a wall-mounted square cylinder, *Ocean Engineering*, 182, 137-146.

Kim, K.C., Lee, M.B., Yoon, S.Y., Boo, J.S., Chun, H.H. (2002). Phase averaged velocity field in the near wake of a square cylinder obtained by a PIV method, *Journal of Visualization*, 5, 29-36.

Kiya, M., Sasaki, K. (1983). Structure of a turbulent separation bubble. *Journal of Fluid Mechanics*, 137, 83-113.

Kumahor, S., Fang, X., & Tachie, M. F. (2021). Upstream roughness and Reynolds number effects on turbulent flow structure over forward facing step. *Journal of Fluids Engineering*, 143, 071301.

Kumahor, S., Tachie, M. F. (2021). Turbulent flow around rectangular cylinders with different streamwise aspect ratios. *Journal of Fluids Engineering*, 144, 051304.

Kumaran, M., Vengadesan, S. (2007). Flow characteristics behind rectangular cylinder placed near a wall. *Numerical Heat Transfer, Part A*, 52, 643-660.

Lander, D.C., Letchford, C.W., Amitay, M., Kopp, G.A. (2016). Influence of the bluff body shear layers on the wake of a square prism in a turbulent flow. *Physical Review Fluids*, 1, 044406.

Lander, D.C., Moore, D.M., Letchford, C.W., Amitay, M., Kopp, G.A. (2018). Scaling of square prism shear layers. *Journal of Fluid Mechanics*, 849, 1096-1119.

Lim, H.C., Castro, I.P. & Hoxey, R.P. (2007). Bluff bodies in deep turbulent boundary layers: Reynolds-number issues. *Journal of Fluid Mechanics*, 571, 97-118.

Martinuzzi, R. J., Bailey, S.C.C, & Kopp, G.A. (2003). Influence of wall proximity on vortex shedding from a square cylinder. *Experiments in Fluids*, 34, 585-596.

McAuliffe, B.R., Yaras, M.I. (2010). Transition mechanisms in separation bubbles under low- and elevated-freestream turbulence. *Journal of Turbomachinery,* 132, 011004.

Mercier, P., Ikhennicheu, M., Guillou, S., Germain, G., Poizot, E., Grondeau, M., Thiebot, J., Druault, P. (2020). The merging of Kelvin-Helmholtz vortices into large coherent flow structures in a high reynolds number flow past a wall-mounted square cylinder. *Ocean Engineering*, 204, 107274.

Minguez, M., Brun, C., Pasquetti, R., & Serre, E. (2011). Experimental and high-order LES analysis of the flow in near-wall region of a square cylinder. *International Journal of Heat and Fluid Flow*, 32, 558-566.

Moore, D.M., Letchford, C.W., Amitay, M. (2019). Energetic scales in a bluff body shear layer. *Journal of Fluid Mechanics,* 875, 543-575.

Nematollahi, A., & Tachie, M. F., (2018). Time-resolved PIV measurement of influence of upstream roughness on separated and reattached turbulent flows over a forward-facing step. *AIP Advances*, 8, 105110.

Nematollahi, A., Nyantekyi-Kwakye, B., Fang, X., Tachie, M. F., Clark, S. P., & Dow, K. (2017). Experimental study of turbulent boundary layer over different shaped cylinders. *The 11th Pacific Symposium on Flow Visualization and Image Processing*, 1-3, Kumamoto, Japan.

Nikuradse, J. (1933). Stromungsgesetz in rauhren rohren, *VDI Forschungshefte,* 361 (English translation: Laws of flow in rough pipes. *Technical Report NACA Technical Memorandum 1292*), National Advisory Commission for Aeronautics, Washington, DC, USA.

Noack, B.R., Afanasiev, K., Morzyński, M., Tadmor, G., & Thiele, F. (2003). A hierarchy of low-dimensional models for the transient and post-transient cylinder wake. *Journal of Fluid Mechanics,* 497, 335-363.

Norberg, C. (1993). Flow around rectangular cylinders: Pressure forces and wake frequencies. *Journal of Wind Engineering and Industrial Aerodynamics*, 49, 187-196.

Okajima, A. (1982). Strouhal numbers of rectangular cylinders. *Journal of Fluid Mechanics,* 123, 379-398.

Panigrahi, P.K. (2009). PIV Investigation of flow behind surface mounted detached square cylinder. *Journal of Fluids Engineering*, 131, 011202.

Panigrahi, P. K., & Acharya, S. (1996). Spectral characteristics of separated flow behind a surface-mounted square rib. *AIAA Fluid Dynamics Conference*, 96, New Orleans, LA, USA.

Portela, F. A., Papadakis, G., & Vassilicos, J. C. (2017). The turbulence cascade in the near wake of a square prism. *Journal of Fluid Mechanics,* 825, 315-352.

Raffel, M., Willert, C. E., Wereley, S. T., & Kompenhans, J. (2007). *Particle Image Velocimetry*. Springer.

Ranjan, P., & Dewan, A. (2017). A PANS study of fluid flow and heat transfer from a square cylinder approaching a plane wall. *International Journal of Thermal Sciences,* 120, 321-336.

Riches, G., Martinuzzi, R., & Morton, C. (2018). Proper orthogonal decomposition analysis of a circular cylinder undergoing vortex-induced vibrations. *Physics of Fluids*, 30, 105103.

Rifat, S. M., Marchildon, A. L., & Tachie, M. F. (2016). Effects of upstream wall roughness on separated turbulent flow over a forward-facing step in an open channel. *International Journal of Mechanical and Mechatronics Engineering*, 10 (2), 250-255.

Roshko, A. (1954). On the drag and shedding frequency of two-dimensional bluff bodies. *Technical Note 3169*, National Advisory Commission for Aeronautics, Washington, DC, USA.

Saathoff, P., & Melbourne, W.H. (1999). Effects of freestream turbulence on streamwise pressure measured on a square-section cylinder. *Journal of Wind Engineering and Industrial Aerodynamics*, 79, 61-78.

Samani, M., & Bergstrom, D. J. (2015). Effect of a wall on the wake dynamics of an infinite square cylinder. *Journal of Wind Engineering and Industrial Aerodynamics*, 55, 158-166.

Samimy, M., & Lele, S. K. (1991) Motion of particles with inertia in a compressible free shear layer. *Physical Review Fluids*, A3(8), 1915-1923.

Sherry, M., Lo Jacono, D., & Sheridan, J. (2010). An experimental investigation of the recirculation zone formed downstream of a forward-facing step. *Journal of Wind Engineering and Industrial Aerodynamics*, 98, 888-894.

Shi, L. L., Liu, Y. Z., & Wang, J. J. (2010). Influence of wall proximity on characteristics of wake behind a square cylinder: PIV measurements and POD analysis. *Experimental Thermal and Fluid Science*, 34, 28-36.

Sirovich, L. (1987). Turbulence and the dynamics of coherent structures. Parts I, II, and III. *Quarterly of Applied Mathematics*, 45 (561-571), 573-590.

Smits, A.J., Matheson, N., & Joubert, P.N. (1983). Low-Reynolds-number turbulent boundary layers in zero and favorable pressure gradients. *Journal of Ship Research*, 27, 147-157.

Straatman, A. G., & Martinuzzi, R. J. (2003). An examination of the effect of boundary layer thickness on vortex shedding from a square cylinder near a wall. *Journal of Wind Engineering and Industrial Aerodynamics*, 91, 1023-1037.

Tachie, M. F., Bergstrom, D. J., & Balachandar, R. (2000). Rough wall turbulent boundary layers in shallow open channel flow. *Journal of Fluids Engineering*, 122, 533-541.

Towne, A., Schmidt, O.T., Colonius, T. (2018). Spectral proper orthogonal decomposition and its relationship to dynamic mode decomposition and resolvent analysis. *Journal of Fluid Mechanics*, 847, 821-867.

Van der Kindere, J., & Ganapathisubramani, B. (2018). Effect of length of two-dimensional obstacles on characteristics of separation and reattachment. *Journal of Wind Engineering and Industrial Aerodynamics*, 178, 38-48.

Van Oudheusden, B. W., Scarano, F., Van Hinsberg, N. P., & Watt, D. W. (2005). Phase-resolved characterization of vortex shedding in the near wake of a square-section cylinder at incidence. *Experiments in Fluids*, 39, 86-98.

Wang, X.K., & Tan, S. K. (2008). Comparison of flow patterns in the near wake of a circular cylinder and a square cylinder placed near a plane wall. *Ocean Engineering*, 35, 458-472.

Welch, P. (1967). The use of fast fourier transform for the estimation of power spectra: a method based on time-averaging over short, modified periodograms. *IEEE Transactions Audio Electroacoustics*, 15(2), 70-73.

Appendix: Supplemental Analysis

Figure A.1 compares the temporal trajectories of the coefficients $a^{(1)}$ and $a^{(2)}$ as well as $a^{(3)}$ and $a^{(4)}$ in the offset cases. The trajectory of POD modes is not shown for the wall-mounted case as it displayed no signs of a coherent pattern. In the ideal case where the cylinder is placed in freestream flow and the cycle-to-cycle variation of vortex shedding motions is negligible (Noack et al. 2003), these two mode coefficients would form a perfect orbital trajectory., and the phase of vortex shedding motion is described by an angle $\varphi = \tan^{-1}\left(\frac{a^{(2)}\sqrt{\lambda_1}}{a^{(1)}\sqrt{\lambda_2}}\right)$, where $a^{(i)}$ and λ_i with i = 1 and 2 are the coefficients and energy of the first and second POD mode, respectively. From Figure A.1, the orbital trajectory of the first two POD mode pairs are coefficients is discernable to varying degrees in different cases, suggesting the occurrence of vortex shedding motion in all offset cases. Additionally, The orbital trajectory of the first mode pair is evidently more organized for larger gap ratios and smooth wall cases. This is indicative of weaker perturbation of incoming turbulence on the vortex shedding motion when the cylinder is farther away from the wall especially for the upstream smooth wall case. In particular, in the R0.3 case, the trajectory of the first two POD mode coefficients is the most random compared with other cases. This randomness is attributed to the intermittency of vortex shedding motion imposed by the significant incoming turbulence through the gap, and is the underlying mechanism for the broader peak observed for this case shown figure 3.4.1b. Bai & Alam (2018) observed that for a square cylinder in a uniform flow, the regular vortex shedding motion is interrupted as the shear layer intermittently reattaches on the side surfaces. Bailey et al (2002) concluded that the suppression of vortex shedding is accompanied by the reattachment of the shear layer on the undersurface of the cylinder. The intermittency of vortex shedding motion in the present R0.3 case is likely due to a stronger tendency of mean flow reattaching on the undersurface of cylinder due to significant incoming turbulence. The exchange

of energy between the first two POD modes and the higher order POD modes observed in Figure 3.4.3e and 3.4.3f is quantified by the coherence of the orbital trajectory of $a^{(3)}$ and $a^{(4)}$. Evidently, the third and fourth POD modes exhibits the smoothest circular pattern for the S2 and R2 cases. The second mode pair for the G/h = 0.3 and 0.5 cases do not exhibit coherent orbital trajectories and likely do not represent true POD mode pairs according to the criteria suggested by Riches et al (2018).

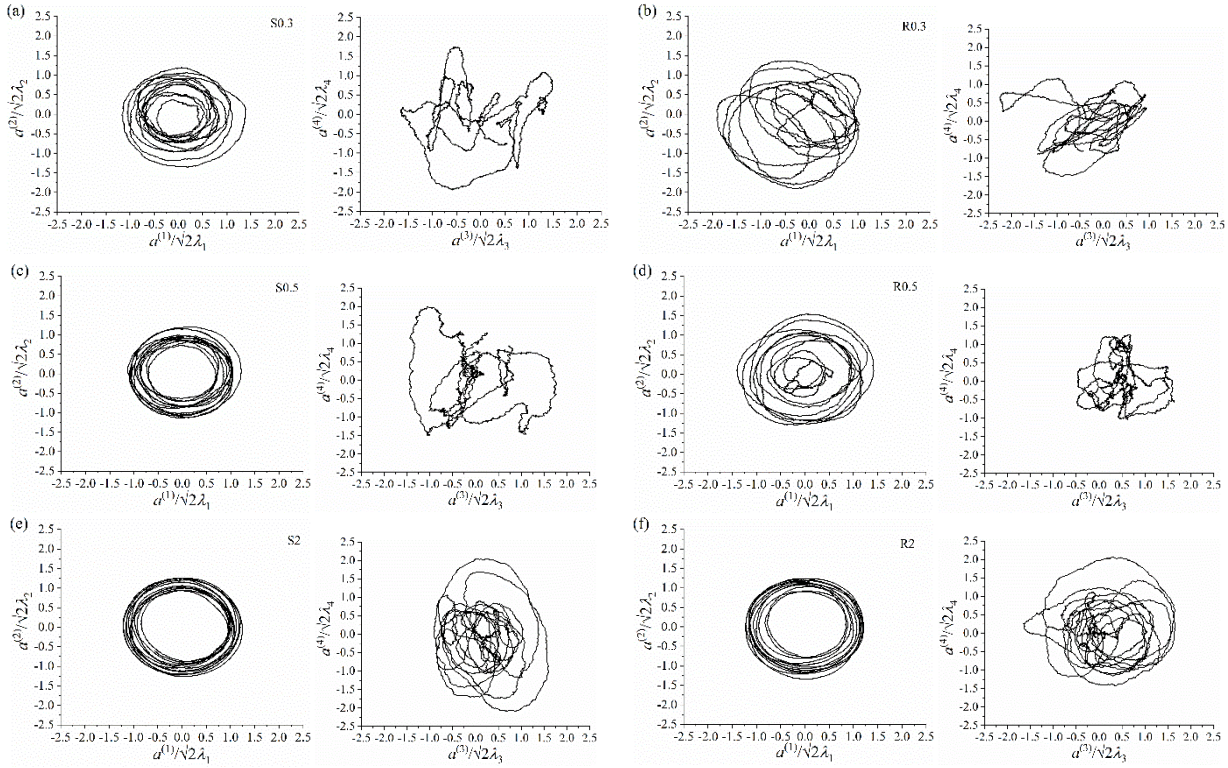

Figure A.1 Temporal trajectories of ($a^{(1)}$, $a^{(2)}$) and ($a^{(3)}$, $a^{(4)}$) for the (a, c, e) smooth and (b, d, f) rough wall cases.

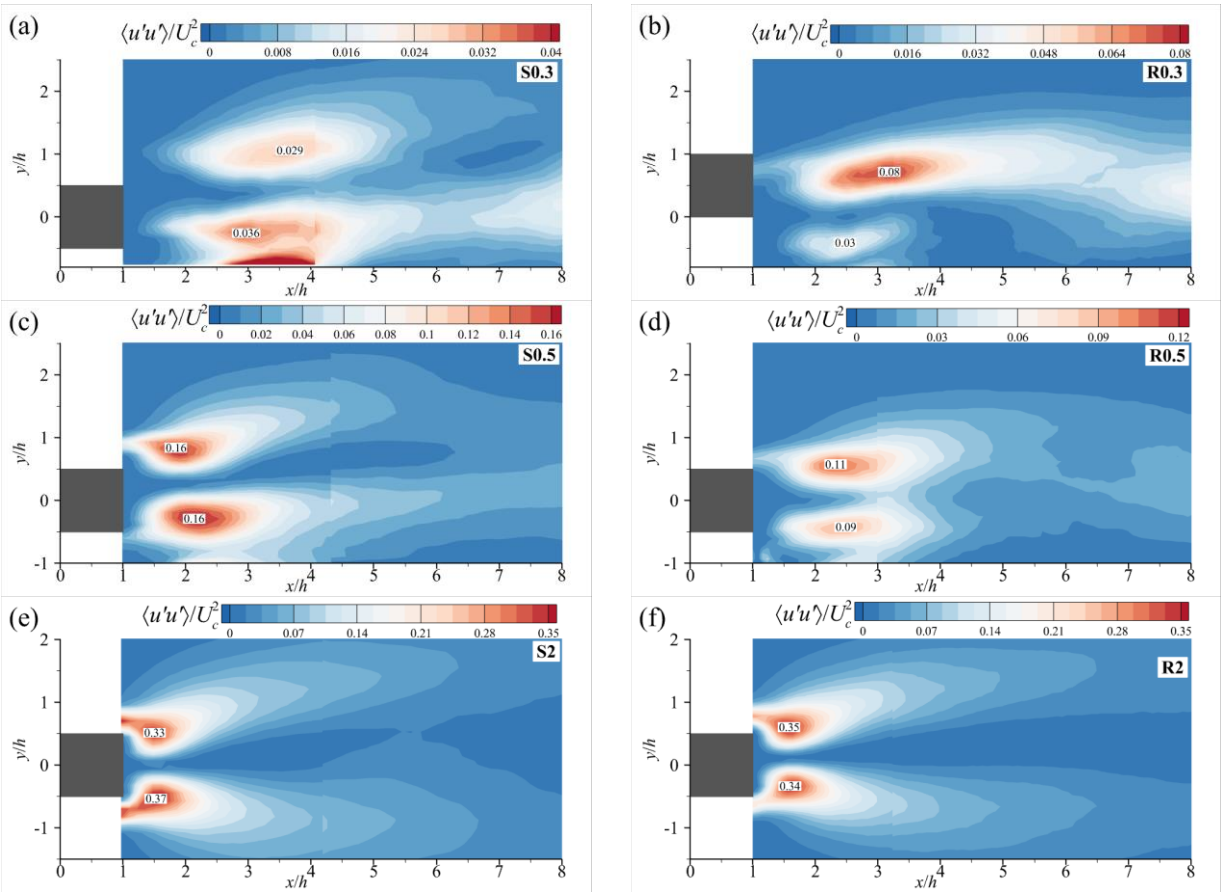

Figure A.2 Contours of the reconstructed streamwise Reynolds normal stress, $u'u'$, using the first four POD modes.

Figure A.2 shows the reconstructed streamwise Reynolds normal stress using the first four POD modes for the various offset cases. For the R0.3 case, the magnitude of the $u'u'$ is larger in the upper shear layer than in the lower shear layer. Furthermore, the relative contribution of the third and fourth modes to the overall reconstruction is approximately 4 times stronger for the R0.3 case compared to the S0.3 case. Since the higher order POD modes are associated with the large-scale motions in the TBL, this suggests that the turbulent fluctuations in the oncoming flow imprint themselves on the wake and manifest in the upper shear layer. As the gap ratio is increased beyond $G/h = 0.3$, the relative contribution of the higher order modes decreases significantly, and the peak values are significantly closer to the $\overline{u'u'}$ values reported in Figure 3.3.1. For instance, the peak

values in the upper and lower shear layers for the S2 and R2 cases are all within approximately 80% of the time-averaged values. Riches et al. (2018) performed reconstruction of wake flow behind a vibrating square cylinder and found that the majority of the time, two modes were sufficient to reconstruct the wake vorticity field. However, at instances when there was low-amplitude modulation of the first two POD mode coefficients, further POD modes were necessary to adequately resolve the flow field. As shown in Figure 3.4.3, the modulation of the first two POD mode coefficients increases for smaller gap ratio cases. Thus, for larger gap ratio cases, the four-mode reconstruction shown above tends closer to the time-averaged Reynolds stress field than smaller gap ratio cases.

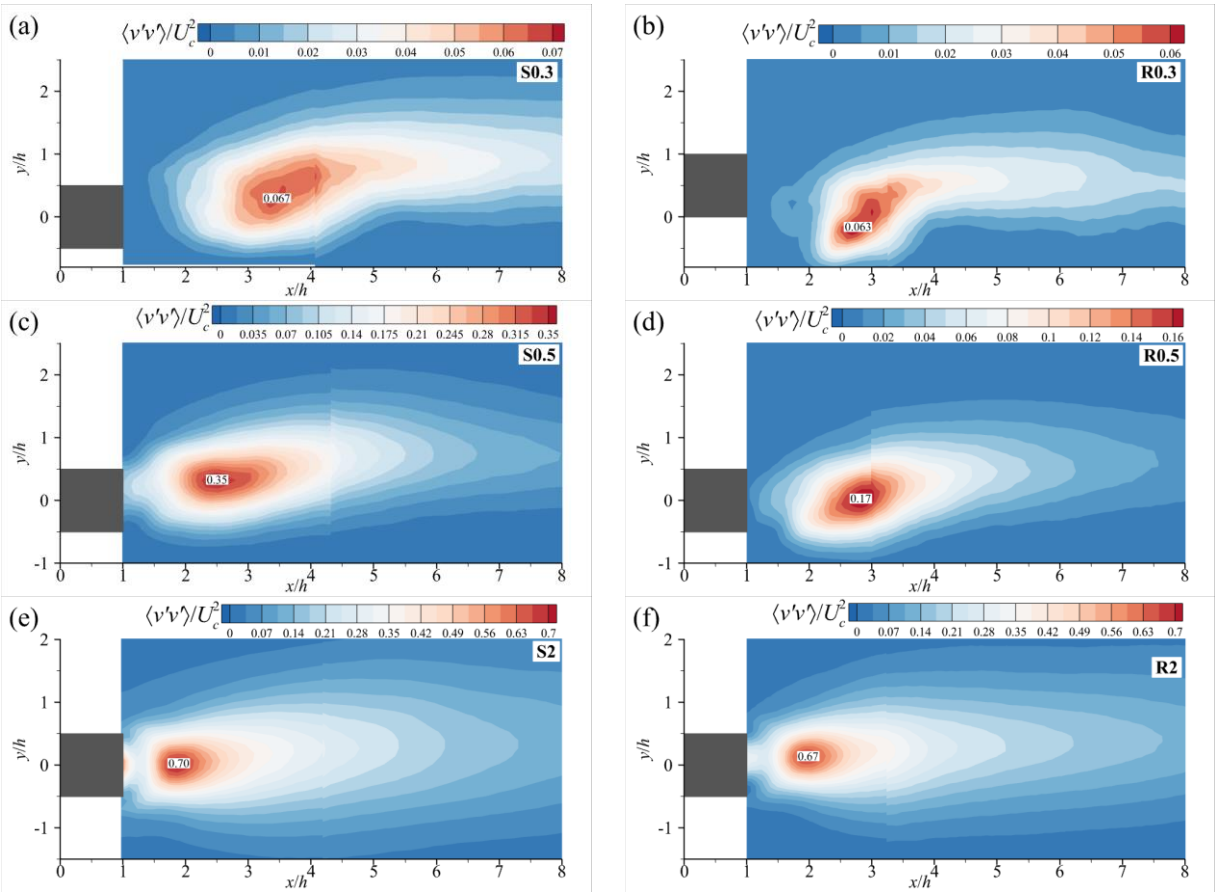

Figure A.3 Contours of the reconstructed vertical Reynolds normal stress, $v'v'$, using the first four POD modes.

Figure A.3 shows the reconstruction of the vertical Reynolds normal stress, $v'v'$, using the first four POD modes. Noticeably in the cases of S0.3 and R0.3, the $v'v'$, is skewed upwards and meanders into the upper shear layer. This is due to the large-scale motions from the TBL manifesting above the cylinder. This phenomenon is not observed for the larger gap ratio cases because of the relative dominance of the vortex shedding motions. Shi et al. (2010) performed reconstruction of a wall pressure signal of a square cylinder near a wall using the first five POD modes and observed that the reconstruction acts as a low-pass frequency filter for turbulent fluctuations. This is observed for larger gap ratio cases but due to the distribution of energy among multiple turbulent length scales when the cylinder approaches the wall, small scale fluctuations in the upper shear layer significantly impact the reconstruction for the G/h = 0.3 cases. For the S0.5 case, the reconstructed $v'v'$ achieves approximately 80% of the time-averaged value despite the $u'u'$ reaching only approximately 65% of the time-averaged value. A similar behaviour is also observed for the R0.5 case where the $v'v'$ attains 68% of the mean value despite the reconstructed streamwise Reynolds normal stress achieving only 48% and 54% in the upper and lower shear layers, respectively. This further emphasizes the transfer of energy from the streamwise velocity component to the vertical velocity component due to the presence of vortex shedding. For the S2 and R2 cases, the first four POD modes adequately capture the coherent motions in the wake and both achieve just over 80% of the peak time-averaged $v'v'$ values.